MULTI-ELECTRON BUBBLE PHASES

A Dissertation

Submitted to the Faculty

of

Purdue University

by

Dohyung Ro

In Partial Fulfillment of the

Requirements for the Degree

of

Doctor of Philosophy

August 2020

Purdue University

West Lafayette, Indiana

THE PURDUE UNIVERSITY GRADUATE SCHOOL
STATEMENT OF DISSERTATION APPROVAL

Dr. Gábor A. Csáthy, Chair

Department of Physics and Astronomy

Dr. Leonid Rokhinson

Department of Physics and Astronomy, Department of Electrical and Computer Engineering

Dr. Paul F. Muzikar

Department of Physics and Astronomy

Dr. Tongcang Li

Department of Physics and Astronomy, Department of Electrical and Computer Engineering

Approved by:

Dr. John P. Finley

Head of the Graduate Program

To my Parents, Sister, and Bumindong & Haeundae Family.

ACKNOWLEDGMENTS

I acknowledge this work was supported by NSF grants DMR 1505866 and 1904497. I would like to thank my advisor Prof. Gábor Csáthy for training me as a strong man and researcher for the past five years and especially appreciate waiting me recovering from the hand injury I had in 2019. I also thank my committee members Prof. Leonid Rokhinson, Prof. Paul Muzikar, and Prof. Tongcang Li for supporting me further towards the next steps. I thank my collaborators Dr. Kenneth West, Dr. Loren Pfeiffer, and Prof. Michael Manfra for providing the excellent quality samples.

I thank physics department staffs Sandy Formica and Janice Thomaz for their kindness and lots of help on complicated administrative tasks, Keith Schmitter for supporting my experiments supplying liquid helium anytime even in the middle of covid-19, Carla Redding and Kasey Howe for purchasing and supplying the equipment necessary for my experiments, James Corwin for always kindly helping me in the machine shop, and Dr. David Sederberg for introducing me to the world of outreach.

I thank my labmates Dr. Kate Schreiber for discussing and answering millions of my questions and helping me even after graduation and Dr. Nianpei Deng for being a guideline to my research. I wish a good luck to my new labmates Sean Myers and Hongxi Li. I thank my physics classmates Jeremy Munsell, Trang Nguyen, Adeel Mughal, and Andres Llacsahuanga for making my Purdue life joyful as well as helping each other throughout different stages of graduate school. I thank my soccer group West Lafayette Football Group (WLFG) and teammates for healing me mentally and physically from the formidable graduate life and being a huge happiness in my life.

I thank Prof. Jonghwan Lee, Prof. Sungkyun Park, and Dr. Jamin Goo for the special lectures in my undergraduate time. And finally, I thank my mom and dad for all the philosophy and physics conversations we are having throughout my life.

Endless love to my parents, sister, and Bumindong & Haeundae family.

TABLE OF CONTENTS

Page

LIST OF TABLES

LIST OF FIGURES

Figure Page

Figure Page

ABSTRACT

Ro, Dohyung Ph.D., Purdue University, August 2020. Multi-Electron Bubble Phases. Major Professor: Gábor A. Csáthy.

Strong electronic correlations in many-body systems are cradles of new physics. They give birth to novel collective states hosting emergent quasiparticles as well as intriguing geometrical charge patterns. Two-dimensional electron gas in GaAs/AlGaAs under perpendicular magnetic field is one of the most well-known hosts in condensed matter physics where a plethora of the collective states appear. In the strong magnetic field regime, strong Coulomb interactions among the electrons create emergent quasiparticles, i.e. composite fermions and Cooper-paired composite fermions. In the weak magnetic field regime, modified Coulomb interactions drive electron solid phases having geometrical charge patterns in the shape of stripes and bubbles and lower the spatial symmetry of the states.

The fascinating charge order in bubble geometry is the electron bubble phase predicted first by the Hartree-Fock theory. In a bubble phase, certain number of electrons cluster as an entity called bubble and the bubbles order into a crystal of triangular lattice. In addition to the Hartree-Fock theory, the density matrix renormalization group and the exact diagonalization methods further support the formation of electronic bubbles.

Reentrant integer quantum Hall states are commonly accepted as the manifestations of the bubble phases in transport experiment. Soon after the first prediction of the Hartree-Fock theory, the reentrant integer quantum Hall states were observed in the third and higher Landau levels. Since then, the association to the bubble phases has been tested with different experimental techniques for decades.

Although the experimental results from different methods support the bubble phase picture of the reentrant integer quantum Hall states, the electron confinement under the quantum well structure hindered direct scanning of bubble morphology. Thus none of the experiments could showcase the bubble morphology of the reentrant integer quantum Hall states. Meanwhile, a significant discrepancy still remained in between the bubble theories and the experiments. Even though the bubble theories predict the proliferation of bubble phases with increasing orbital index, none of the experiments could observe multiple reentrant integer quantum Hall states in a high Landau level, which signify the multiple bubble formation. Therefore, the proliferation of bubble phases with increasing Landau level index was pessimistic.

In this Dissertation, I present my research on solving this discrepancy. In chapter 4, we performed a magnetotransport measurement of reentrant integer quantum Hall states in the third and higher Landau levels at various different temperatures. Then, we scrutinized how each of the reentrant integer quantum Hall states develops with the gradual increase of the temperature. As a result, we observed multiple reentrant integer quantum Hall states in the fourth Landau level which are associated with the two- and three-electron bubble phases. This result strongly supports the bubble phase picture of the reentrant integer quantum Hall states by confirming the possibility of the proliferation of bubble phases in high Landau levels.

In chapter 5, I analyzed the energetics of newly resolved two- and three-electron bubble phases in the fourth Landau level as well as those of two-electron bubble phases in the third Landau level. Here, I first found, in the fourth Landau level, the three-electron bubbles are more stable than the two-electron bubbles indicating that the multi-electron bubbles with higher electron number are more stable within a Landau level. Secondly, I found distinct energetic features of two- and three-electron bubble phases which are independent of Landau level index throughout the third and the fourth Landau levels. These results highlight the effect of the number of electrons per bubble on the energetics of multi-electron bubble phases and are expected to contribute on improving the existing Hartree-Fock theories.

1. CLASSICAL AND QUANTUM HALL EFFECTS

When the magnetic field is applied perpendicularly to the direction of current to a material which current passes through, apart from the expected voltage drop along the direction of the current, voltage drop transverse to the direction of the current also occurs [1]. This voltage is called the *Hall voltage* and with the voltage drop along the direction of the current, *longitudinal voltage*, it provides fruitful information to characterize the electronic states of the material.

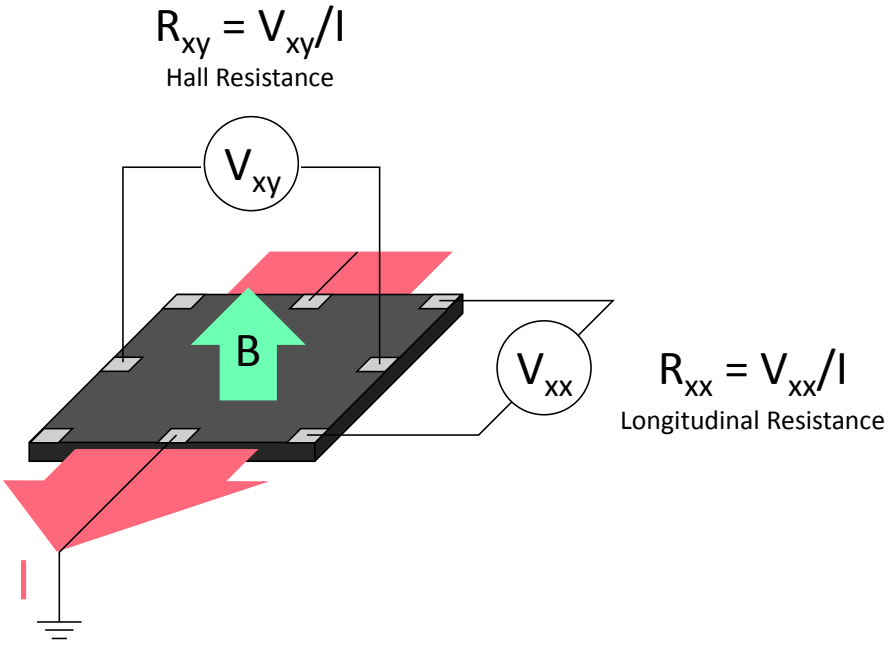

Figure 1.1. A Hall bar configuration to measure the longitudinal voltage V_{xx} and the Hall voltage V_{xy}. From the longitudinal and Hall voltage, the longitudinal resistance R_{xx} and the Hall resistance R_{xy} are deduced respectively.

1.1 Classical Hall Effect

This phenomenon of induced Hall voltage due to a perpendicularly applied magnetic field is called *Hall effect* and was first discovered in a gold strip by Edwin Hall in 1879 [1]. The emergence of Hall voltage is well described by the Lorentz force in classical electromagnetism. As electrons experience the Lorentz force passing through the perpendicular magnetic field, electrons deflect toward one side of the sample and are piled up to the side. As a result, the voltage difference between the two sides of the sample is created.

The signature of classical Hall effect is the linearly increasing Hall voltage with respect to increasing magnetic field. The linear dependence is quantified $R_{xy} = B/en$, where R_{xy} is the Hall resistance, B is the perpendicular magnetic field, e is the electron charge, and n is the carrier density. Thus, by measuring the Hall resistance, one can find the carrier density of the material, which is an important characteristic of material.

1.2 Introduction to the Quantum Hall Effects

As the dimensions of electronic system reduce into two dimensions and the temperature lowers down to liquid helium temperature, more interesting phenomena emerge. For the *two-dimensional electron gas (2DEG)* confined in GaAs/AlGaAs quantum well, plateaus appear on the Hall resistance R_{xy} vs perpendicular magnetic field plot at low temperature. Surprisingly, these plateaus only appear at the quantized values of the Hall resistance $R_{xy} = \dfrac{h}{ie^2}$, where h is the Planck constant, e is the elementary charge, and i are the quantized filling factors. These phenomena of the emergence of novel electronic states corresponding to each of the quantized plateaus are called *quantum Hall effect (QHE)* and divided into two categories: one with integer filling factors, *integer quantum Hall effect (IQHE)*, and the other with fractional filling factors, *fractional quantum Hall effect (FQHE)*. Unlike the classical Hall effect which

can be described classically, the quantum Hall effects require quantum mechanical descriptions.

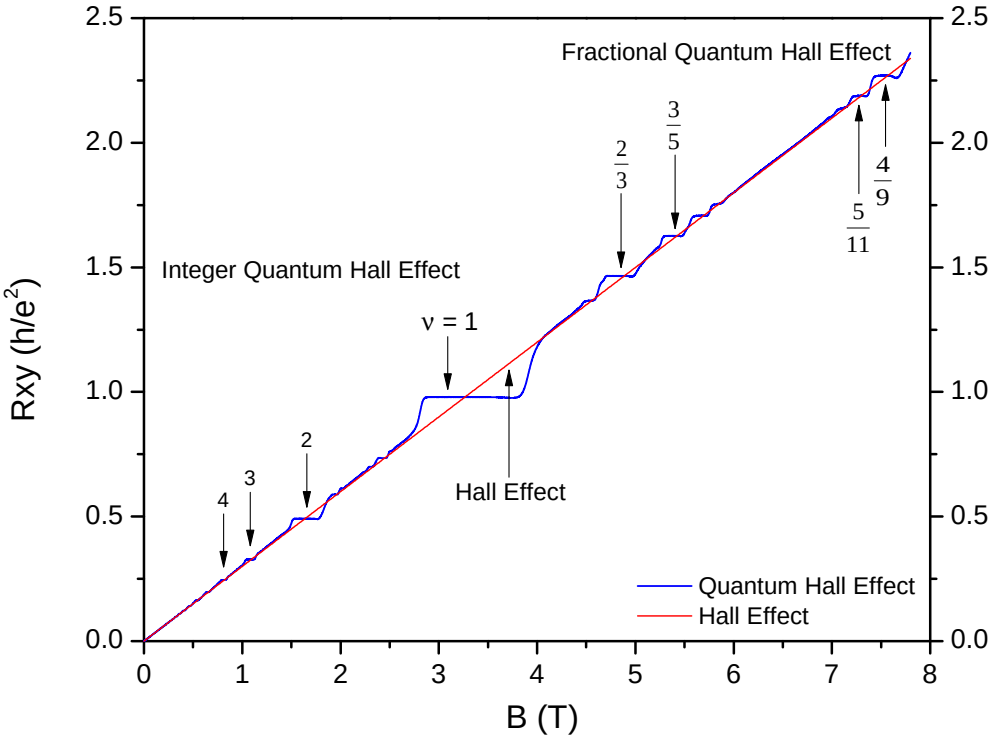

Figure 1.2. Comparison between the (classical) Hall effect and quantum Hall effects. The Hall resistance is plotted in the units of *von Klitzing constant* $\frac{h}{e^2}$ which is approximately 25.8 kΩ. The integers and fractions marking each plateau are the filling factors. The fitted red line shows the linearity of classical Hall effect behavior in the measured trace of quantum Hall effects.

1.3 Integer Quantum Hall Effect

The IQHE was first discovered in an inversion layer of MOSFET (metal-oxide-semiconductor field-effect transistor) by Klaus von Klitzing in 1980 [2]. The signature of IQHE is the plateau at the integer-quantized value of the Hall resistance R_{xy},

$$R_{xy} = \frac{h}{\nu e^2} = \frac{h}{ie^2} \tag{1.1}$$

where h is the Planck constant, ν is the filling factor, and i is an integer ($i = 1, 2, 3...$), and the vanishing to zero longitudinal resistance R_{xx}.

$$R_{xx} = 0 \tag{1.2}$$

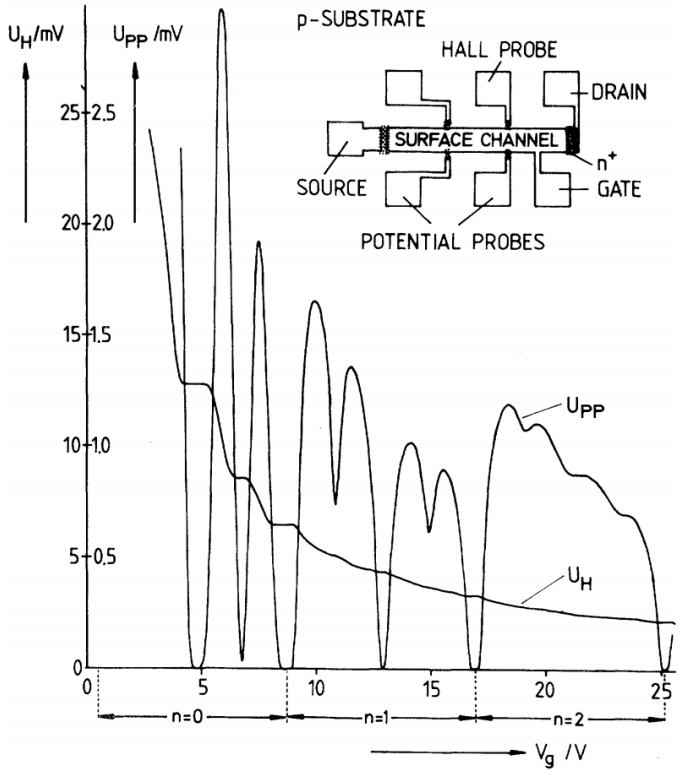

Figure 1.3. The first observation of IQHE by K. von Klitzing et al. [2]. The plateaus in the Hall resistance as well as the vanishing longitudinal resistance identify the integer quantum Hall states. Reprinted figure with permission from Ref. [2]. Copyright © 1980 by American Physical Society.

The IQHE is understood through the quantization of the energy band in the magnetic field. Before the perpendicular magnetic field is applied, the 2DEG has the continuous energy band. As the perpendicular magnetic field is applied, the continuous energy band quantizes into discrete energy levels called *Landau levels*. This quantization of energy band into Landau levels is the analytical result of solving the

Schrödinger equation with the Hamiltonian describing one spin-less electron confined in 2D, on the X-Y plane, with the perpendicular magnetic field in the Z-direction [3,4].

Hamiltonian:

$$\hat{H} = \frac{1}{2m^*}(\hat{p} + eA)^2 \tag{1.3}$$

where m^* is the effective mass of electron, $\hat{p}$ is the momentum operator, e is the elementary charge, and $A = Bx\hat{y}$ is the Landau gauge.

Wave Functions:

$$\Psi(x, y)_n = e^{ik_y y} u_n(x + \hbar k_y / eB) \tag{1.4}$$

where $k_y = 2\pi m/L_y$, ($m = 0, 1, 2...$, L_y is the system width), $u_n(x)$ is the solution of 1D simple harmonic oscillator.

Landau Levels:

$$E_n = (1/2 + n)\hbar\omega_c \tag{1.5}$$

where $n = 0, 1, 2...$, $\hbar = h/2\pi$, $\omega_c = eB/m^*$ is the cyclotron frequency of electrons (e is the elementary charge, B is the perpendicular magnetic field, and m^* is the effective mass of electron.).

Number of Degenerate States (not per unit area)

$$N = eBA/h \tag{1.6}$$

where e is the elementary charge, B is the perpendicular magnetic field, A is the area of system, and h is the Planck constant.

Counting the spin of electron, a Landau level splits into two *Zeeman energy levels*.

Zeeman Energy Gap:

$$\Delta_{Zeeman} = g\mu B \tag{1.7}$$

where, g is the g-factor of the host material, μ is magnetic moment of electron, and B is the perpendicular magnetic field. Zeeman energy gap indicates the energy difference between the upper (spin-down) and lower (spin-up) spin branches within a Landau level.

Each spin branch of Landau level or Zeeman energy level corresponds to one integer filling factor. The lowest energy spin branch is $\nu = 1$, which is the spin-up

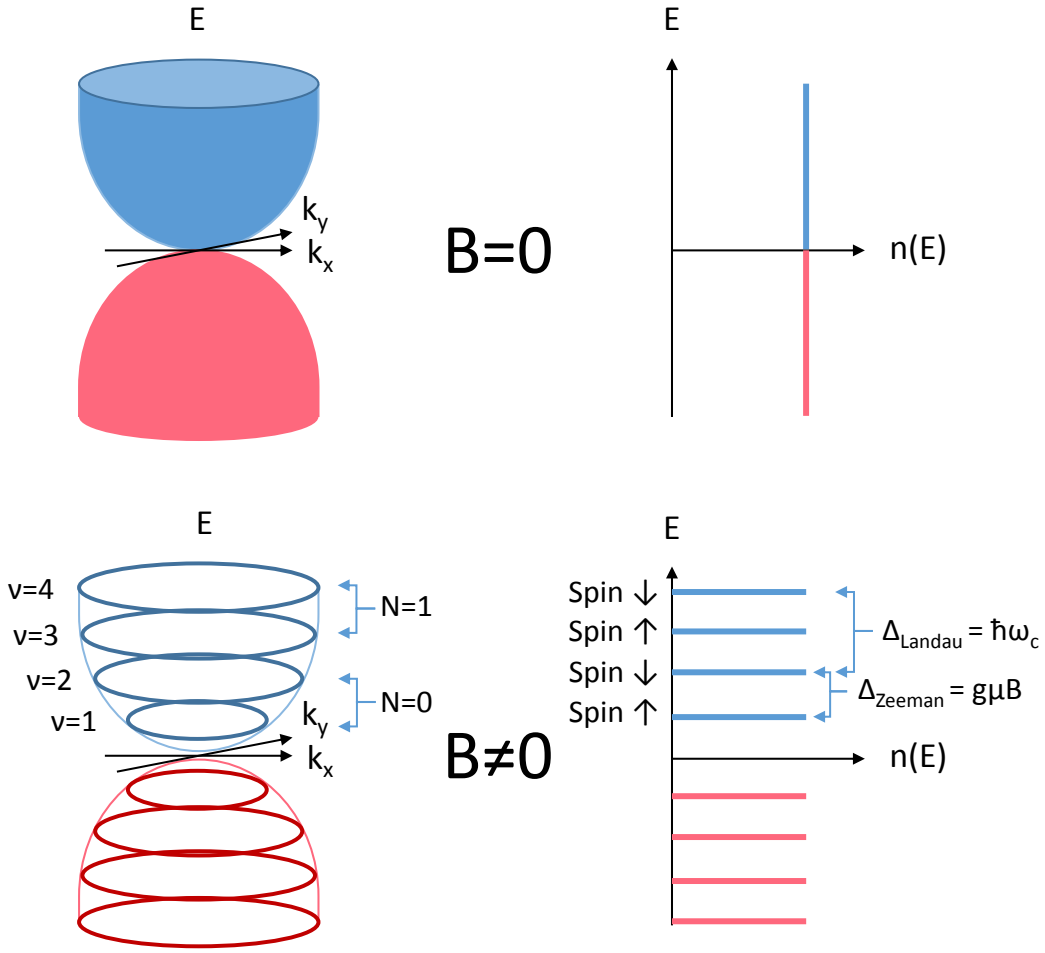

Figure 1.4. Quantization of the energy band into the Landau levels due to the perpendicular magnetic field. The 2DEG in GaAs has parabolic energy band with single valley, unlike that in graphene which has cone-shaped energy band with multiple valleys. The density of states n(E) is constant with respect to energy in two-dimensions.

branch of the lowest Landau level. The second lowest energy spin branch is $\nu = 2$, which is the spin-down branch of the lowest Landau level. In GaAs, in ambient pressure, the spin-up branch has lower energy than the spin-down branch within a landau level due to the negative value of g-factor [5]. Thus, also for the other Landau levels, spin-up branch has lower energy than the spin-down branch.

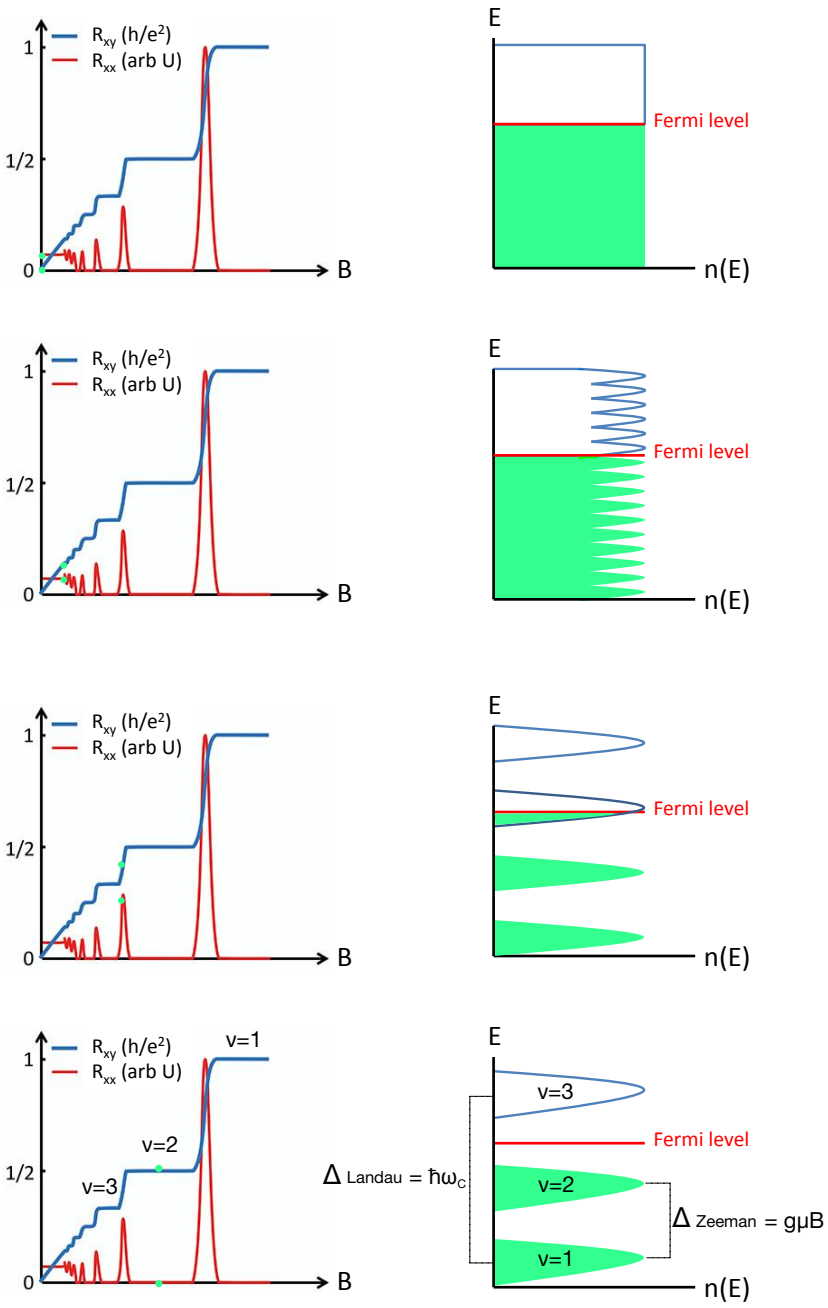

Figure 1.5. Evolution of R_{xx}, R_{xy}, and Landau levels with increasing perpendicular magnetic field. As the magnetic field increases, the Landau levels expand and spread out towards the higher energy regime. Figure adapted with permission from Ref. [7]. Copyrighted by American Physical Society.

The lowest Landau level (N=0 Landau level) has the energy of $E_0 = \frac{1}{2}\hbar\omega_c$ and the second lowest Landau level or the first excited Landau level or the N=1 Landau level has the energy of $E_1 = \frac{3}{2}\hbar\omega_c$. Here, one needs to pay attention to the terminology describing the second lowest Landau level. People use several different terminologies to describe the second lowest and higher Landau levels. The energy difference between two consecutive Landau levels is $\Delta_{Landau} = \hbar\omega_c$.

The physical meaning of the filling factor is the total number of electrons/the number of states in one spin branch of Landau level. The $\nu = 1$ IQHS fills all the available states of the lowest spin branch. The $\nu = 2$ IQHS fills all the available states of the two lowest spin branches.

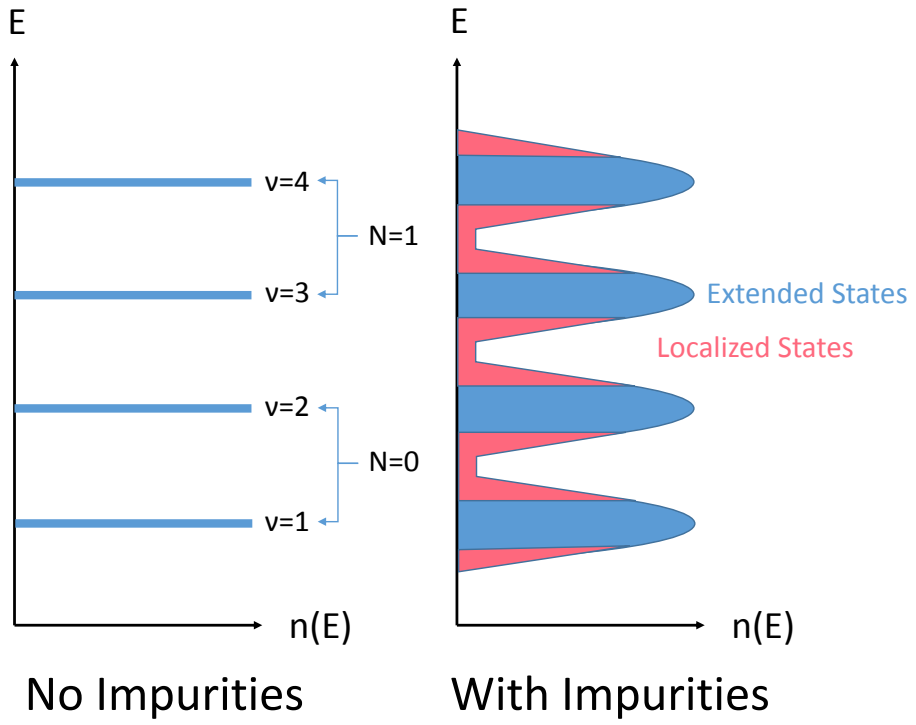

Figure 1.6. The Landau level broadening due to the impurity effect. Thanks to the presence of impurities even in the purest sample, the narrow Landau levels broaden and host more states as the extended and the localized states.

The IQHSs are heavily degenerate states since there are a number of combinations of k_x and k_y within a Landau level. Semi-classically the number of degenerate states (not per unit area) is equal to the number of the minimum area for an electron's cyclotron motion throughout the total area of the system. This number coincides with the total number of the magnetic flux in the area of the system [3].

Owing to the effect of the impurities in the sample, extra states in between the Landau levels which are called *localized states* are created and these states allow the Fermi level to locate in between the Landau levels. If there is no state in between the *extended states*, which are the conducting states inside the Landau levels, Fermi level

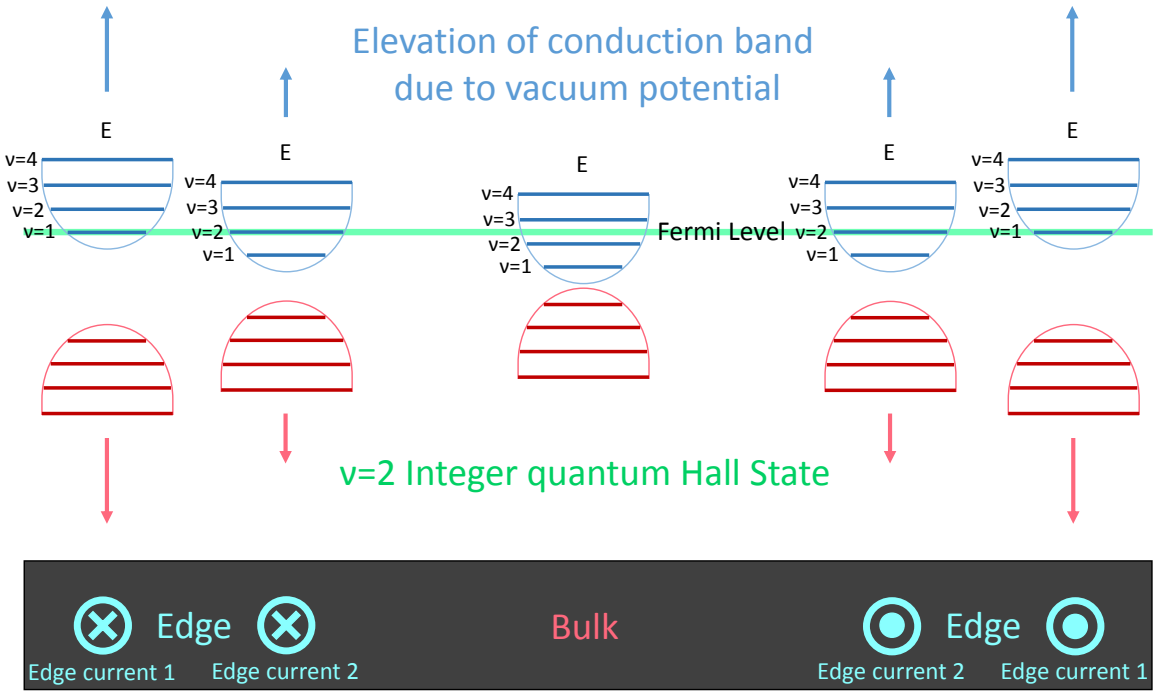

Figure 1.7. The origin of the edge current. The conduction band elevates as it reaches to the edge of sample due to the vacuum potential. As a result, the Fermi level crosses the elevated underlying Landau levels at the edge. The number of Fermi level crossed Landau levels is the number of edge current. The $\nu = 2$ IQHS is shown as an example.

will directly jump up to the next Landau level to conserve the number of electrons and as a result, R_{xy} plot will lose the plateaus.

Looking into the quantized Landau levels in the conduction band, when the Fermi level is in the extended states, the host material is metallic, since there are vacant energy levels right above and below the Fermi level similar to a normal metal. As a result, R_{xy} increases with increasing magnetic field. When the Fermi level is in the localized states, the bulk of the host material is insulating, because the impurities localize the carriers in the energy level right above or below the Fermi level. As a result, R_{xy} creates the plateaus. Although the bulk is insulating, the edge of the

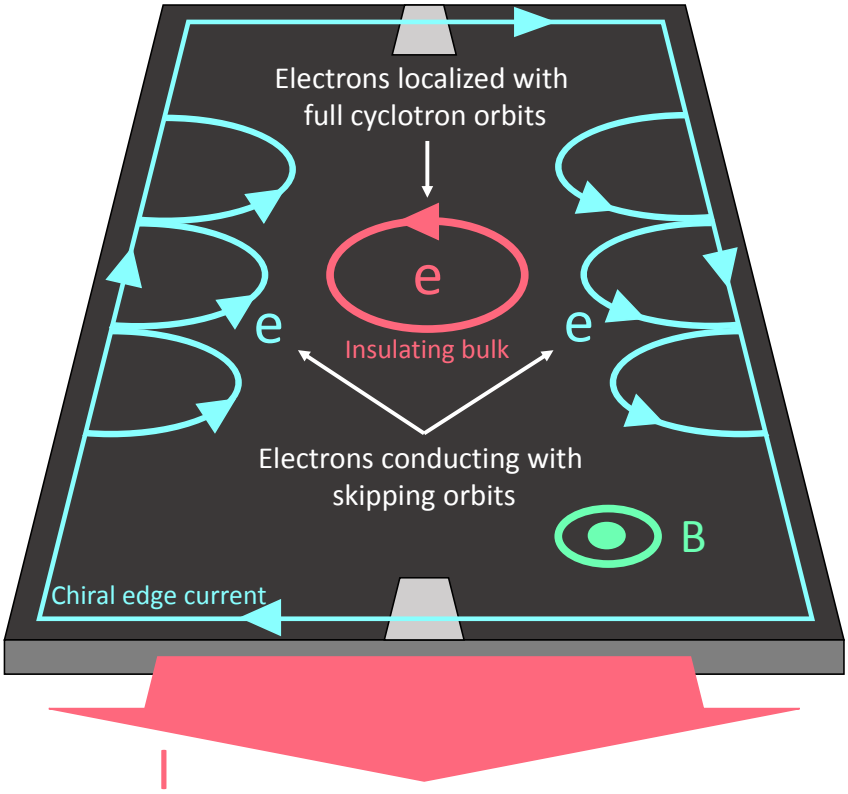

Figure 1.8. The semi-classical picture of dissipation-less chiral edge current of quantum Hall states. The skipping orbit trajectory suppresses backscattering only for one chiral direction at the edge. Meanwhile, in the bulk, the electrons in full cyclotron motion are localized.

sample conducts. This is because the Landau levels skyrocket at the edge of the sample due to the effect of the vacuum potential. This current at the edge is called *edge current* and shows the dissipation-less nature, which is an important feature of the quantum Hall states.

Dissipation-less nature of the edge current can be intuitively described through semi-classically [8–10]. The 2DEG in perpendicular magnetic field is in cyclotron motion in the semi-classical picture. Electrons in the bulk are localized through the complete orbital motion. However, electrons at the edge are not able to finish a complete circular motion due to the reflection to the edge of the sample. This reflection suppresses the back-scattering of the electrons and yields the net translation of the electrons along the edge of the sample towards the grounding contact. As a result, there is no potential drop along the edge and R_{xx} becomes zero.

Although the four terminal measurement of the longitudinal resistance gives the $R_{xx} = 0$ thanks to the dissipation-less chiral edge current, the two terminal measurement in between the input contact (source) and the ground contact (drain) gives the Hall resistance, R_{xy} not the longitudinal resistance, R_{xx}. This is because the input contact shares its potential with one edge and the drain contact shares its potential with the other edge [4].

1.4 Fractional Quantum Hall Effect

The FQHE was first discovered in a GaAs/AlGaAs heterostructure by Daniel C. Tsui , Horst L. Stormer, and Arthur C. Gossard in 1982 [12]. The signature of the FQHE is the plateau at the fraction-quantized value of the Hall resistance R_{xy},

$$R_{xy} = \frac{h}{\nu e^2} = \frac{h}{ie^2} \tag{1.8}$$

where h is the Planck constant, ν is the filling factor, and i is a fraction ($i = 1/3, 2/3, 1/5, 2/5, ...$), and the vanishing to zero longitudinal resistance R_{xx}.

$$R_{xx} = 0 \tag{1.9}$$

Unlike the IQHEs, which are the phenomena of non-interacting electrons, FQHEs are phenomena of interacting electrons. These interacting electrons of different fractional quantum Hall states (FQHSs) can be mapped into non-interacting or interacting *composite fermions*, which are the quasiparticles made up of one electron and even number of vortices [13]. A "*n vortex*" is an topological object which gives $2n\pi$ phase on the wave function or order parameter when the particle completes one rotation [3].

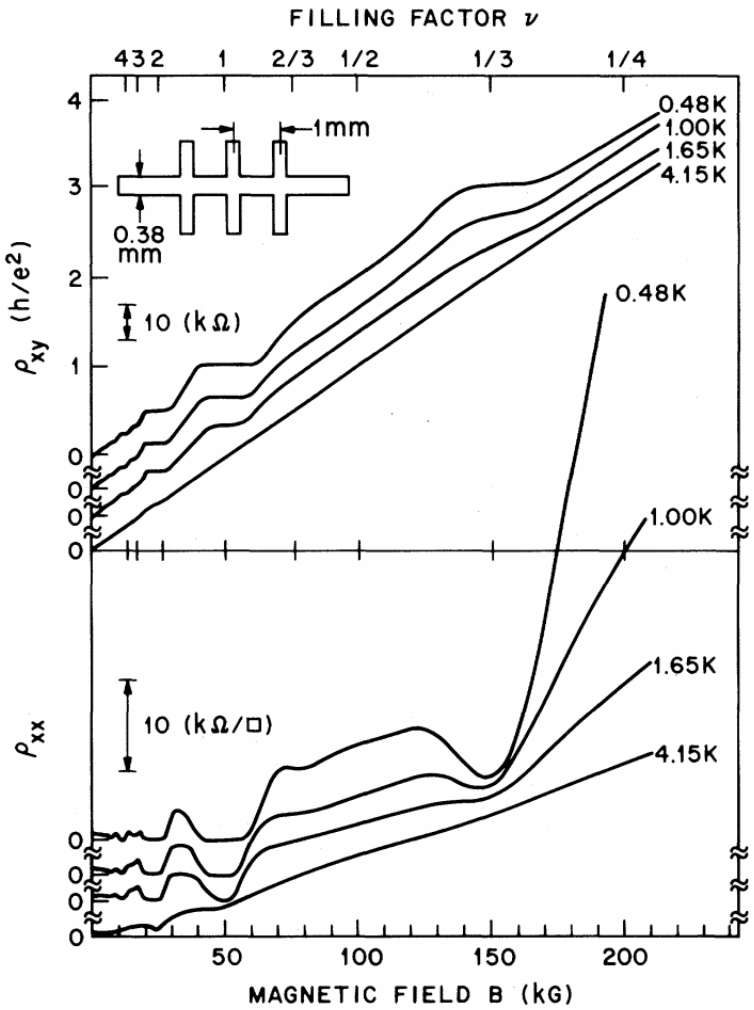

Figure 1.9. The first observation of FQHE by D.C. Tsui et al. [12]. The plateau in the Hall resistance and the vanishing longitudinal resistance at the filling factor $\nu = 1/3$ capture the fractional quantum Hall state. Reprinted figure with permission from Ref. [12]. Copyright © 1982 by American Physical Society.

Roughly speaking, the FQHSs are divided into two categories: *odd-denominator states* and *even-denominator states*. Odd-denominator states are the FQHSs of which the denominators of the filling factors are odd. Odd-denominator states include

$$\nu = 1/3, 2/3, 1/5, 2/5, 3/5, 4/5, ... \tag{1.10}$$

which are identified with the equations

$$\nu = \frac{n}{2pn \pm 1} \tag{1.11}$$

$$\nu = 1 - \frac{n}{2pn \pm 1} \tag{1.12}$$

where n is positive integer (n=1, 2, 3...), and p is also positive integer (p=1, 2, 3,...) which indicates the number of pairs of vortices attached on one electron [3]. p=1 indicates there are two vortices attached on one electron. p=2 indicates there are four vortices attached on one electron. In the odd-denominator states, composite fermions do not interact one another and Jainendra K. Jain's composite fermion theory can explain most of the odd-denominator states as the IQHE of composite fermion [13].

Even-denominator states are the FQHSs of which the denominators of the filling factors are even. Even-denominator states include

$$\nu = 5/2, 7/2 \tag{1.13}$$

In the even-denominator states, composite fermions interact one another and the composite fermion theory requires additional interacting terms in Hamiltonian. As a result, novel quasiparticles such as p-wave paired composite fermions have been theorized to explain these exotic states [22]. In addition, these quasiparticles are predicted to follow the non-Abelian braiding statistics [22], and with this property one may realize the qubits of fault-tolerant topological quantum computer [23–25]. Thanks to this applicational importance as well as rich physics, FQHEs have been one of the most actively investigated topics in the field of condensed matter physics from the past decades.

1.4.1 Odd-Denominator Fractional Quantum Hall States

Most of the odd-denominator FQHSs can be understood through both the interacting electrons picture and non-interacting composite fermions picture. Laughlin's ansatz and the hierarchical expansion are based on the interacting electrons picture while Jain's composite fermion theory is based on the non-interacting composite fermions picture. Although the two approaches give the same mathematical results, the composite fermion theory became the cornerstone for describing the fractional quantum Hall states, since the composite fermion theory can cover more states including the $\nu = 1/2, 3/2$ composite fermion seas and the $\nu = 5/2, 7/2$ paired composite fermion states (even-denominator FQHSs) thanks to its simpler nature [3]. In addition, the Laughlin's states turn out to be the special cases in composite fermion picture [3].

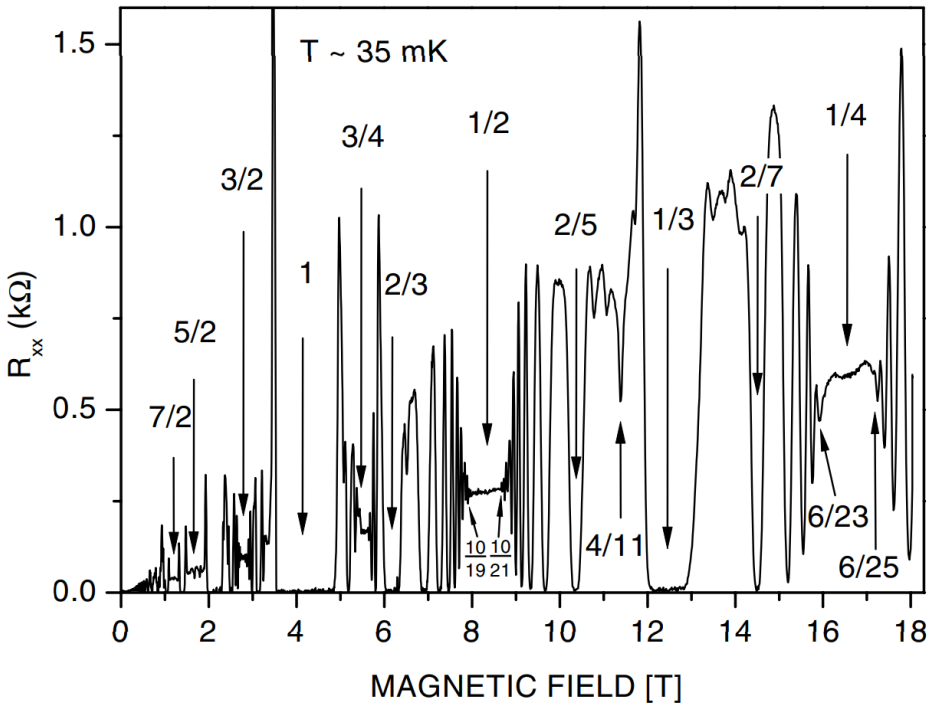

Figure 1.10. A variety of odd-denominator FQHSs measured by W. Pan et al. [14]. Reprinted figure with permission from Ref. [14]. Copyright © 2002 by American Physical Society.

Laughlin States

The interacting electrons model was theorized earlier than the composite fermion theory as one may expect. Robert B. Laughlin proposed the ground state ansatzs of the $\nu = 1/m$ states, where m are the odd integers (m=3, 5, 7...) in 1983 [15].

Laughlin wave function:

$$\Psi_{1/m}^{\text{Laughlin}}(z_1, ..., z_N) = \prod_{j<k}^{N}(z_j - z_k)^m \exp\left[-\frac{1}{4l_B^2}\sum_{j}^{N}|z_j|^2\right] \tag{1.14}$$

where m are the odd integers (m = 3, 5, 7...), z_j is the position of the jth particle ($z_j = x_j + iy_j$) , N is number of particles, and l_B is the magnetic length [3, 15–17]. These wave functions are the variational solution of the Hamiltonian describing the situation that N number of electrons are in the magnetic field corresponding to the vector potential A with the coulomb interaction among the electrons while there is background positive ion charge uniformly spread over the space.

Laughlin Hamiltonian:

$$\hat{H}^{\text{Laughlin}} = \sum_{j}^{N}\frac{1}{2m}(\hat{p} + eA)^2 + \sum_{j<k}^{N}\frac{e^2}{4\pi\epsilon|r_j - r_k|} + \sum_{j}^{N}V_{ion}(\vec{r}_j) \tag{1.15}$$

where m is the mass of electron, $\hat{p}$ is the momentum operator, $-e$ is the electron charge, $A = B(x\hat{y} - y\hat{x})/2$, r_j is the position of the jth particle, and $V_{ion}(\vec{r}_j)$ is the background positive potential [3, 15–17]. The first term represents the kinetic energy of electrons in magnetic field; the second term indicates the coulomb interaction among the electrons; and the last term shows the back ground positive potential of the jellium. In this way, Laughlin explained the emergence of the odd-denominator FQHSs in the $\nu = 1/m$ filling factors, where m are the odd integers (n=3, 5, 7...).

Hierarchy States

After the first observation of $\nu = 1/m$ FQHSs, a variety of different odd denominator FQHSs were also observed. Since the Laughlin ansatzs can explain only the

$\nu = 1/m$ FQHSs, additional formalism is required to explain the existence of the FQHSs of which the numerators of filling factors are bigger than 1. Duncan Haldane and Bertrand Halperin solved this problem by theorizing the hierarchy among the Laughlin and non-Laughlin odd-denominator FQHSs [18, 19]. In this hierarchy model, the $\nu = 1/m$ Laughlin states are the parents states which give birth to their daughter states $\nu = (1 + p)/(m + 2p)$, where p are the integers (p=0, 1, 2...). The emergence of daughter states is explained by the condensation of new quasiparticles in the parents states.

Composite Fermion Theory

With the combination of the Laughlin states and the Hierarchical expansion, most of the odd denominator states are explained. However, there is a simpler and more universal approach using a novel quasiparticle called composite fermion [13]. Composite fermion theory explains the odd denominator FQHE (of electrons) as the IQHE of composite fermions. In other words, the composite fermion theory maps the interacting electrons of Laughlin picture into non-interacting composite fermions picture.

Composite fermion Hamiltonian

$$\hat{H}^{\mathrm{CF}} = \sum_{j}^{N} \frac{1}{2m}(\hat{p} + eA^* + ea(r_j))^2 \tag{1.16}$$

where m is the mass of composite fermion, $\hat{p}$ is the momentum operator, $-e$ is the composite fermion charge, A^* is the corresponding effective vector potential for the effective magnetic field B^*, r_j is the position of the jth particle, and $a(r_j)$ is the vector potential which attaches the magnetic flux quanta to each electron and make an electron as a composite fermion [3]. The first and second term describe the particles are place in the effective magnetic field and the third term indicates the particles are the composite fermions not electrons.

Few steps of composite fermionization including changing the magnetic flux quanta into vortices and the lowest Landau level projection, after the variational approach

using the ground state wave function of the electrons, one can reach to the wave function of composite fermion [3].

Composite fermion wave function

$$\Psi^{\mathrm{CF}}_{n/2pn\pm1} = P_{LLL}\Phi_{\pm n}\prod_{j<k}^{N}(z_j - z_k)^{2p} \tag{1.17}$$

where n are the positive integers (n = 1, 2, 3...), P_{LLL} is the lowest Landau level projection operator, $\Phi_{\pm n}$ is the ground state wave function of electrons in the effective

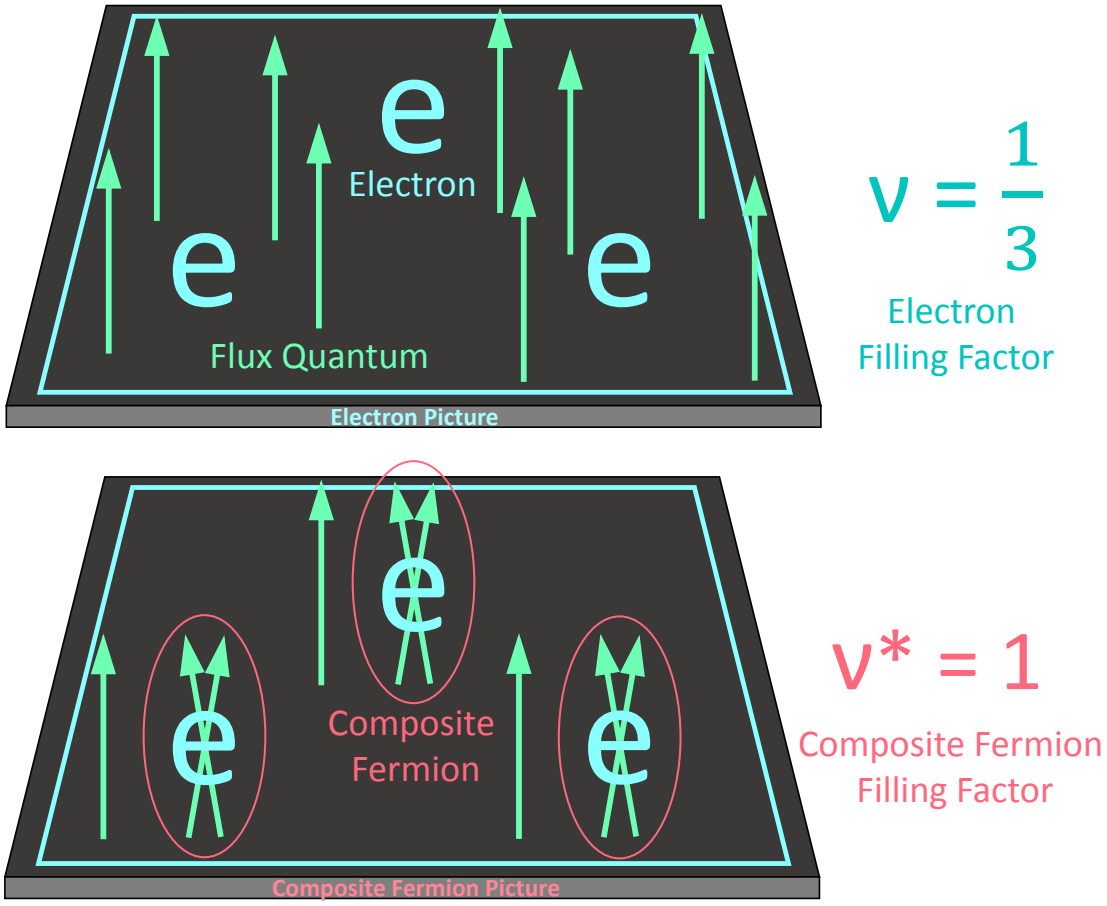

Figure 1.11. The mapping of electron picture into composite fermion picture. The $\nu = 1/3$ FQHS of electron can be mapped into $\nu^* = 1$ IQHS of composite fermion, where the ν^* is composite fermion filling factor.

magnetic field B^*, ($\pm$ sign indicates the direction of effective magnetic field), z_j is the position of the jth particle ($z_j = x_j + iy_j$), and N is number of particles [3].

Each of these wave functions corresponds to the filling factors,

$$\nu = \frac{n}{2pn \pm 1} \tag{1.18}$$

$$\nu = 1 - \frac{n}{2pn \pm 1} \tag{1.19}$$

where n is positive integer (n=1, 2, 3...), and p is also positive integer (p=1, 2, 3,...) [3]. With the combination of n, p, and $\pm$, one can get the wave functions of most of the odd-denominator states. For example, (n=1, p=1, +) gives the wave function of $\nu = 1/3$ and $\nu = 2/3$; and (n=2, p=1, +) earns $\nu = 2/5$ and $\nu = 3/5$.

Here, in the $\nu = 1/3$ state, we can roughly think there is one composite fermion (one electron plus two magnetic fluxes) per one left-over magnetic flux. The numerator indicates the number of electrons and the denominator indicates the number of magnetic flux. In the $\nu = 2/5$ state, we can think there are two two-flux composite fermions per one left-over magnetic flux. Likewise, in the $\nu = 3/7$, there are three two-flux composite fermions per one left-over magnetic flux. Thus, by adding a composite fermion, a daughter state is created from its parents state. In this way, composite fermion theory describes most of the odd-denominator FQHSs covering both the Laughlin and hierarchy states.

1.4.2 Even-Denominator Fractional Quantum Hall States

The $\nu = 5/2$ FQHS and its upper spin branch counter part $\nu = 7/2$ FQHS are the most important and actively researched states in the field of quantum Hall physics. This is because the quasiparticle excitations in the states are predicted to have non-Abelian anyonic braiding statistics [22] which is the prerequisite to realize the decoherence-free topological quantum computer [23–25].

Although the even denominator FQHSs should not exist according to non interacting composite fermion picture, R.L. Willett et al. [20] discovered the emergence

of FQHS at $\nu = 5/2$ in 1987 and W. Pan et al. [21] cofirmed its full development later in 1999. In contrast to the odd-denominator FQHSs which are described with non-interacting composite fermions, even-denominator FQHSs are formalized with interacting- or paired-composite fermions.

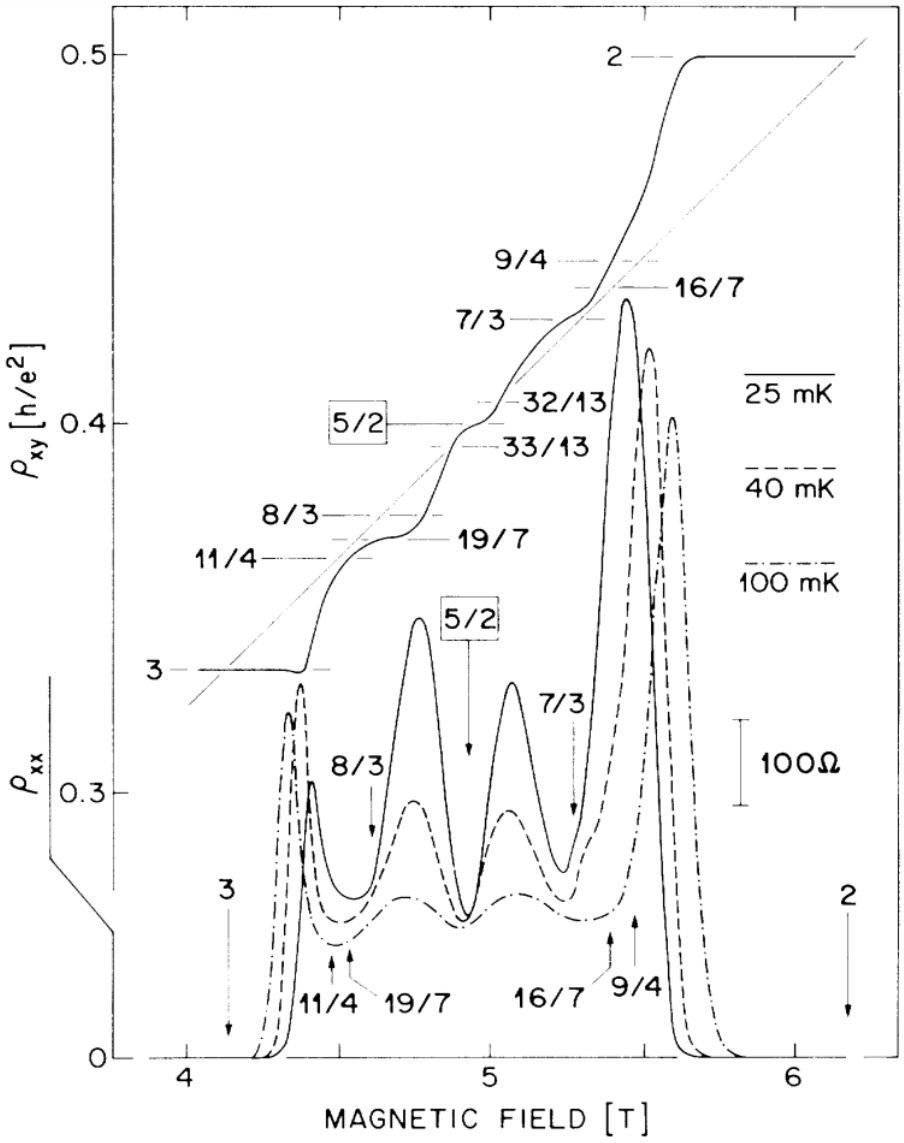

Figure 1.12. The first observation of even-denominator FQHS at $\nu = 5/2$ by R. Willett et al. [20]. Reprinted figure with permission from Ref. [20]. Copyright © 1987 by American Physical Society.

However, the contrasting experimental results could not make coherent agreement on the ground state of $\nu = 5/2$ FQHSs among the candidate wave functions. The most convincing candidates include 1) *Pfaffian or Moore-Read Pfaffian state*, 2) *anti-Pfaffian state*, and 3) *331 state*. The identity of these states is characterized with the ground state spin-polarization, quasiparticle-excitation braiding statistics, quasiparticle charge, and the wave function itself. Although a number of experiments have been conducted to clarify those characteristics, the experimental results supported different candidates.

In this subsection, I will first introduce the most popular candidates, Pfaffian wave function and its particle-hole conjugate anti-Pfaffian wave function followed by the Abelian candidate 331 state. Then, I will discuss how the paradigm of $\nu = 5/2$ ground state changed towards the expanded parametric regime.

Pfaffian Wave Function

Pfaffian or Moore-Read Pfaffian wave function is the most popular candidate among the others. It was proposed by Moore and Read in 1991 [22].

Pfaffian wave function

$$\Psi^{\text{Pfaffian}}(z_1, ..., z_N) = Pf\Big(\frac{1}{z_j - z_k}\Big)\Psi^{\text{Laughlin}}_{1/(m=2)}(z_1, ..., z_N) \tag{1.20}$$

$$Pf\Big(\frac{1}{z_j - z_k}\Big) = \frac{1}{z_1 - z_2}\frac{1}{z_3 - z_4}\frac{1}{z_5 - z_6}... - \frac{1}{z_1 - z_3}\frac{1}{z_2 - z_4}\frac{1}{z_5 - z_6}... + ... - ... \tag{1.21}$$

where Ψ^{Laughlin} is the Laughlin wave function with $m = 2$, and $Pf\Big(\frac{1}{z_j - z_k}\Big)$ is the Pfaffian operator [16, 22].

Pfaffian wave function is basically a Laughlin wave function at $\nu = 1/2$ with the Pfaffian term attached on it [16]. Pfaffian term here describes the weak coulomb interaction among the composite fermions. By attaching the Pfaffian term, the particles in Hamiltonian become the p-wave paired composite fermions from the unpaired ones.

Pfaffian wave function attracted its popularity mainly due to the numerical calculation done by R. H. Morf in 1998 [26]. Morf numerically calculated for the spin-polarized and unpolarized system with 18 or less electrons and found that the ground state is 1) spin-polarized, 2) incompressible, and 3) overlapped largely with the the Pfaffian wave function. Due to the Morf's work, the Pfaffian became the most plausible states dominating against the other spin-unpolarized states including the Haldane-Rezayi state and 331 state. Pfaffian has a spin-polarized and incompressible ground state with non-Abelian quasiparticle excitation braiding statistics.

Anti-Pfaffian Wave Function

Although the $\nu = 5/2$ FQHS is considered to be a particle-hole symmetric state, Pfaffian wave function is the exact ground state of the Hamiltonian which is not particle-hole symmetric [16]. The Hamiltonian has the three body interaction term which breaks the particle-hole symmetry in addition to the two body interaction term conserving the particle-hole symmetry. Thus the exact ground state of the particle-hole conjugated Hamiltonian is different from its non-conjugated counterpart. This particle hole conjugated wave function of Pfaffian is called anti-Pfaffian wave function [27, 28]. Anti-Pfaffian has a spin-polarized and incompressible ground state with non-Abelian quasiparticle excitation braiding statistics.

331 State

331 state is another candidate of the ground state of $\nu = 5/2$ FQHS. It is first proposed by B. I. Halperin in 1983 [29]. Unlike the Pfaffian or anti-Pfaffian, it is spin-unpolarized state with Abelian quasiparticle excitation braiding statistics.

Summary on the Ground States of $\nu = 5/2$ FQHS

The initial paradigm of the competition among different candidate wave functions was made upon assuming a single state emerging at the $\nu = 5/2$. However, this perspective could not explain the contrasting experimental results as well as the broken particle-hole symmetry of Pfaffian and anti-Pfaffian wave functions. As a result, the paradigm shifted to the expandend parametric regime picture with multiple ground states.

After considering different correlation potentials in the Hamiltonian describing even minor factors such as Landau level mixing and finite thickness effect, different candidates are thought to describe the ground state of different parametric regime. The broken particle-hole symmetry of Pfaffian and anti-Pfaffian wave functions could also be justified from the broken particle-hole symmetry of three-body interaction term describing the Landau level mixing. This expanded parametric regime picture is further supported by the theoretical [27, 28, 31, 32] and experimental [30] works predicting and observing the phase transition between Pfaffian and anti-Pfaffian by tuning the Landau level mixing parameter. Moreover, the observation of the nematic phase in high Landau level mixing and low adimensional width regime tuned by hydrostatic pressure further concretes this picture [33–36].

2. ELECTRON SOLIDS IN TWO DIMENSIONAL ELECTRON GAS

In addition to the integer and fractional quantum Hall states we discussed in the previous chapter, the 2DEG in GaAs/AlGaAs quantum well also hosts different group of states which require different order parameters. They are the *nematic phases or stripe phases* at the half-fillings of N=2 and higher Landau levels at $\nu = 9/2, 11/2, 13/2, 15/2, ...$; *reentrant integer quantum Hall states or bubble phases* appearing at the flanks of IQHSs in the N=1 and higher Landau levels; and *Wigner*

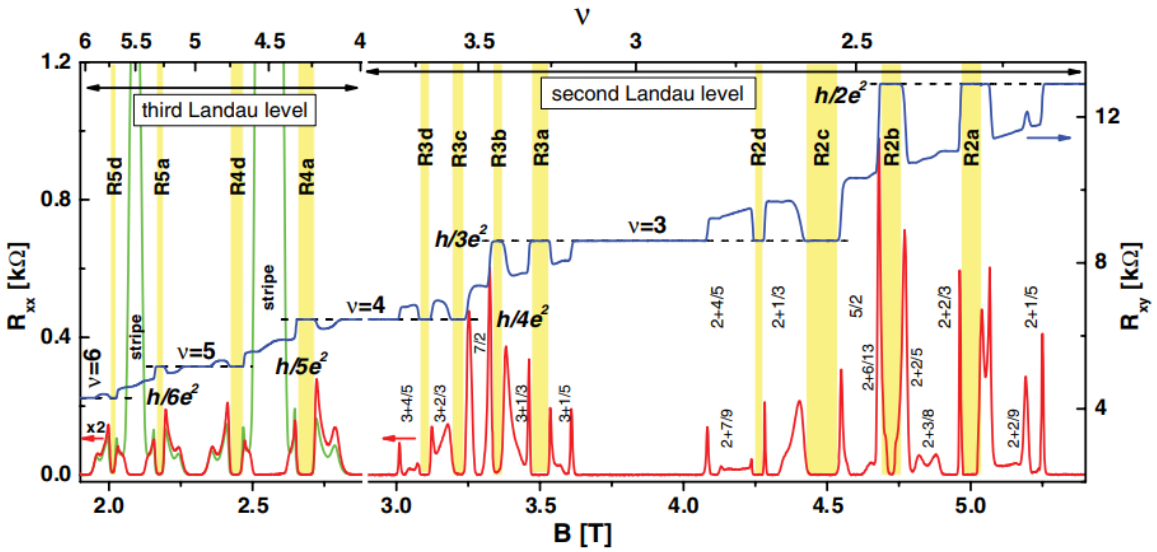

Figure 2.1. A variety of states of 2DEG in GaAs/AlGaAs quantum well. This figure portraying the N=1 and N=2 Landau levels containing the integer and fractional quantum Hall states as well as the nematic phases and the reentrant integer quantum Hall states shows the rich physics of the quantum Hall system. Reprinted figure with permission from Ref. [73]. Copyright © 2012 by American Physical Society.

crystals at the low partial filling factors of the N=0 and higher Landau levels. In these states, electrons are arranged periodically as atoms in solids in the shape of stripes, bubbles, and crystal lattice and altogether they are called *electron solids*. The emergence of electron solids of different morphology is the result of electron-electron interactions.

The electron solid phases require the Landau symmetry breaking picture in addition to or rather than the topological picture which IQHSs and FQHSs are described. IQHSs and FQHSs are the topological states of which the phase transition between two different IQHSs or FQHSs is described by the topological order rather than the traditional Landau symmetry breaking picture with the order parameters. Since the topology of the Berry curvature in the k-space plays role of defining a state, IQHSs and FQHSs are called topological states. On the other hand, the different geometrical charge configurations of electron solids require the description of traditional Landau symmetry breaking picture.

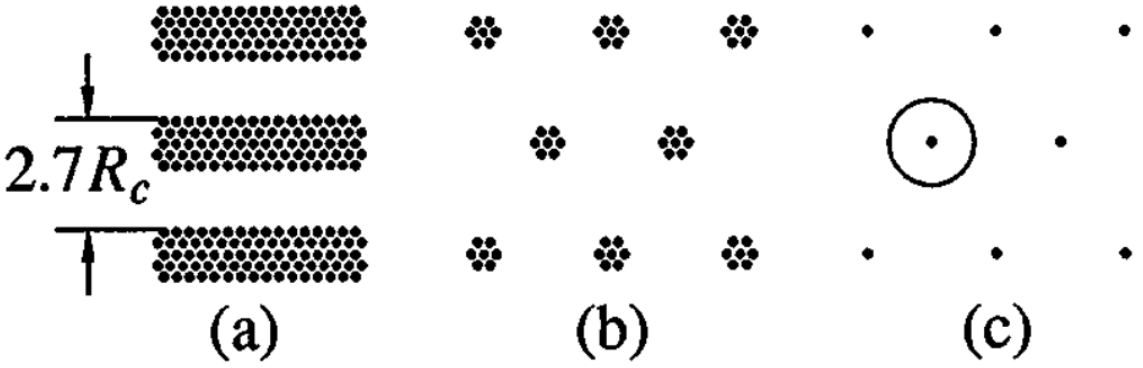

Figure 2.2. Electron solid phases predicted by A.A. Koulakov et al. [61]. The (a) nematic phase, (b) bubble phase, (c) Wigner crystal are schematically shown. R_c in (a) is the cyclotron radius and the circle in (c) indicates the cyclotron orbit. Reprinted figure with permission from Ref. [61]. Copyright © 1996 by American Physical Society.

2.1 Wigner Crystals

Wigner crystal is a solid phase of electrons which the localized electrons build a triangular lattice to minimize the energy of the system [42–45]. The low filling factor regime ($\nu < 1/5$) in the N=0 Landau level where the longitudinal resistance diverges with the temperature drop are commonly accepted as the Wigner crystal state. In the state, the low density of electrons exposed to high magnetic field are localized in small cyclotron motion avoiding the overlap of wave functions. As a result, the constructed triangular Wigner crystal plane is pinned to disorders.

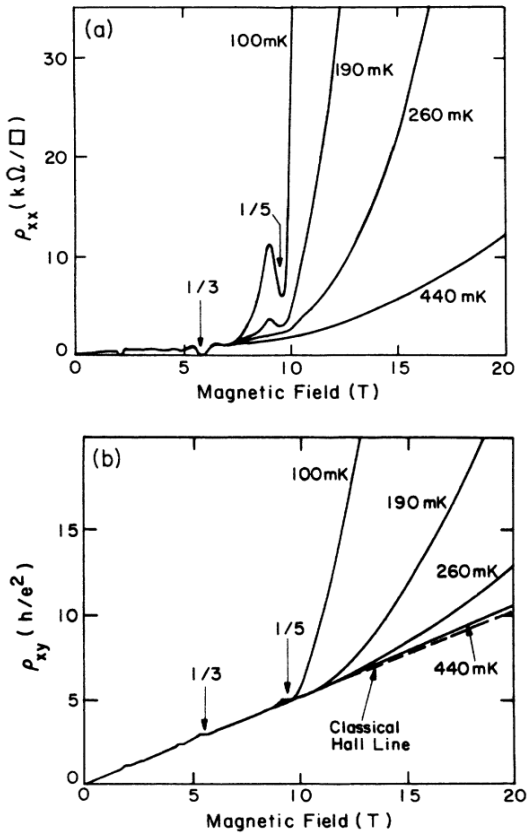

Figure 2.3. The resistive features of Wigner crystal in the N=0 Landau level. The rapidly increasing longitudinal and Hall resistances with decreasing temperature suggest the formation of Wigner crystal at the high magnetic field regime above $\nu = 1/5$. Reprinted figure with permission from Ref. [46]. Copyright © 1988 by American Physical Society.

Because the standard AC magnetotransport techniques are limited from examining different properties of Wigner crystals, multiple techniques including microwave [47–52], DC-current [48, 53–55], and tunneling resonance [94] are used to investigate the Wigner solid.

In addition to the Wigner crystal forming in the lowest Landau level, the filling factor ranges slightly away from integers in high Landau levels are also predicted to form the Wigner crystals as known as one-electron (M=1) bubble phases [89–94].

2.2 Reentrant Integer Quantum Hall States: Electron Bubble Phases

Reentrant integer quantum Hall states (RIQHSs) are the states of which the R_{xy} and R_{xx} values reenter the nearest IQHS value. They locate at the flank of the IQHSs commonly in the N=1 and higher Landau levels. As the Landau level index increases, RIQHSs are faded and eventually washed out as the Shubnikov-de Hass oscillation with other states due to the weak magnetic field. RIQHSs are widely accepted as the bubble phases of the Hartree-Fock theory [61, 63].

Electron bubble phases were first predicted in the Hartree-Fock theory by A.A. Koulakov, M. M. Fogler, and B. I. Shklovskii in one paper [61] and R. Moessner and J. T. Chalker in the other paper published in 1996 [63]. Later in 1999, the RIQHSs were first observed in GaAs heterojunctions by M. P. Lilly et al. [66] and R. R. Du et al. [67]. According to the Hartree-Fock theory, the electrons in the partially filled high Landau levels form the electron solids in the shape of stripe, bubble, and crystal lattice. The bubble shaped electron solids are the bubble phases, while the other two are nematic phases and Wigner crystals. The emergence of the geometric patterns attribute to the competition between the long-range repulsive term and the short-range attractive exchange term in the Coulomb interaction in the weak magnetic field regime. This competition becomes dramatic in high Landau levels due to the presence and proliferation of nodes in the electron wave functions of high Landau levels. The cohesive energy of the stripe, bubble, and Wigner crystal phases compete

throughout the partial filling factor range and the one with the minimum cohesive energy appears as the pattern of the phase.

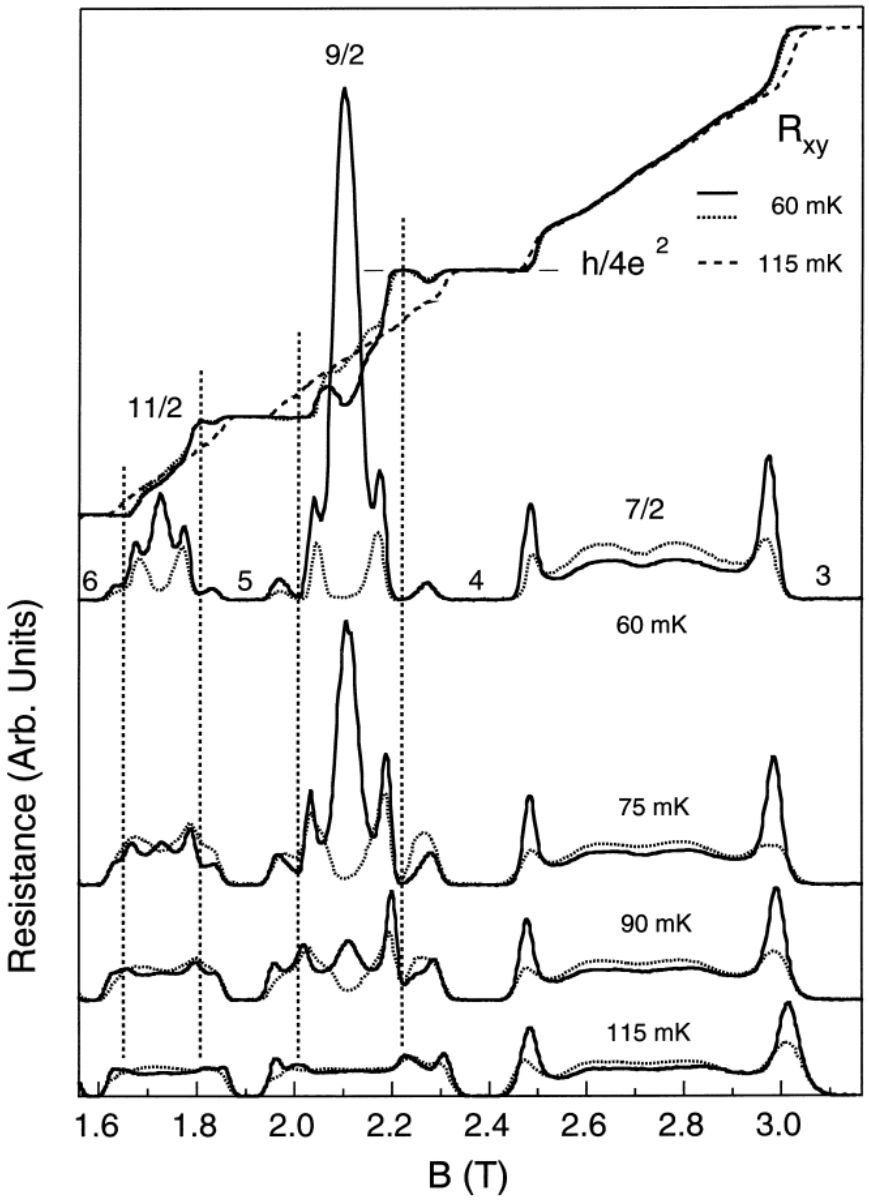

Figure 2.4. One of the two earliest observations of RIQHSs by R.R. Du et al. [67]. The association of RIQHSs to previously predicted bubble phases was first made by this work. Reprinted figure with permission from Ref. [67]. Copyright © 1999 by Elsevier.

In the bubble phases, the combination of a guiding center of electron cyclotron orbit and the orbiting electrons is called a *bubble* [76]. These bubbles form triangular lattice and the overall are pinned to disorders. More than one electron can orbit one guiding center. One electron bubble phase which one electron is rotating a guiding center in a bubble is also called Wigner crystal state. Two-, three-, and multiple-electron bubble phases are called *multi-electron bubble phases* [120] which the number of electrons per bubble are described with the index M. The M=2 and M=3 bubble phases indicate two- and three- electron bubble phases respectively. The dis-

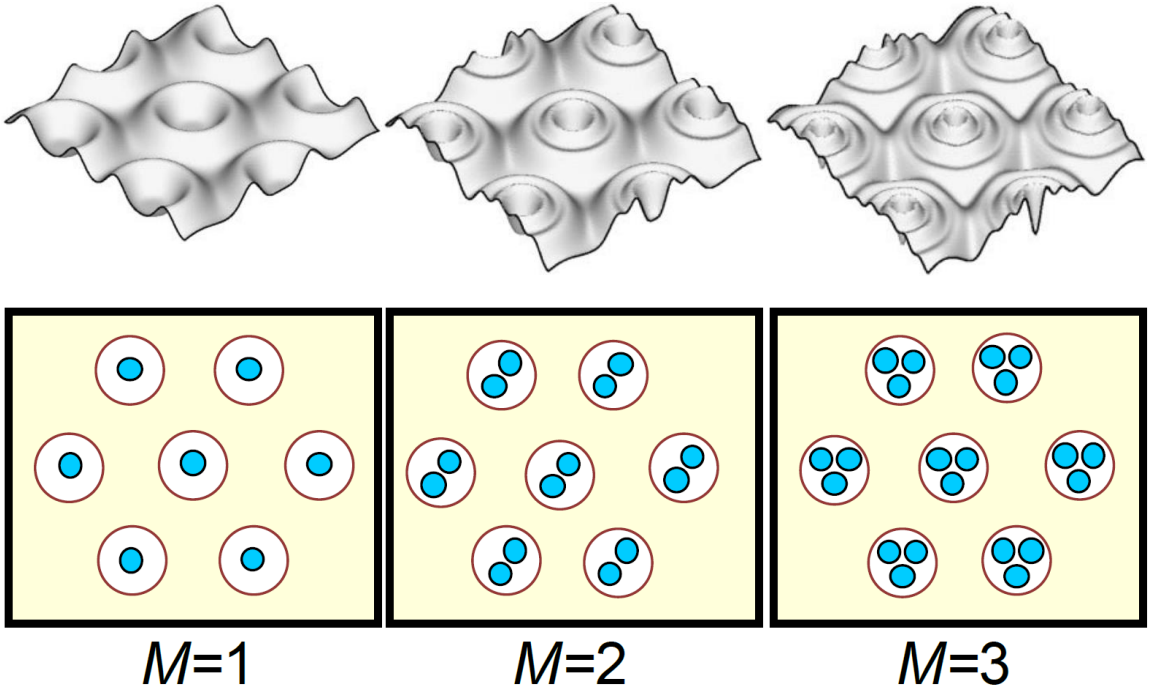

Figure 2.5. The calculated density patterns (top) and the simplified schematic descriptions (bottom) of one-, two-, and three-electron bubble phases are shown. The number of concentric-circular density patterns distinguishes the multi-electron (M=2 and M=3) and the single-electron (M=1) bubble phases. Reprinted figures with permission from Ref. [79] and Ref. [117]. Copyright © 2013, 2019 by American Physical Society.

tance between two bubbles is approximately three cyclotron radii of the corresponding magnetic field.

In addition to the Hartree-Fock theory, numerical calculations such as the density-matrix renormalization group (DMRG) [78] and exact diagonalization [64] method also predict the formation of bubble phases in the N=2 and higher Landau levels.

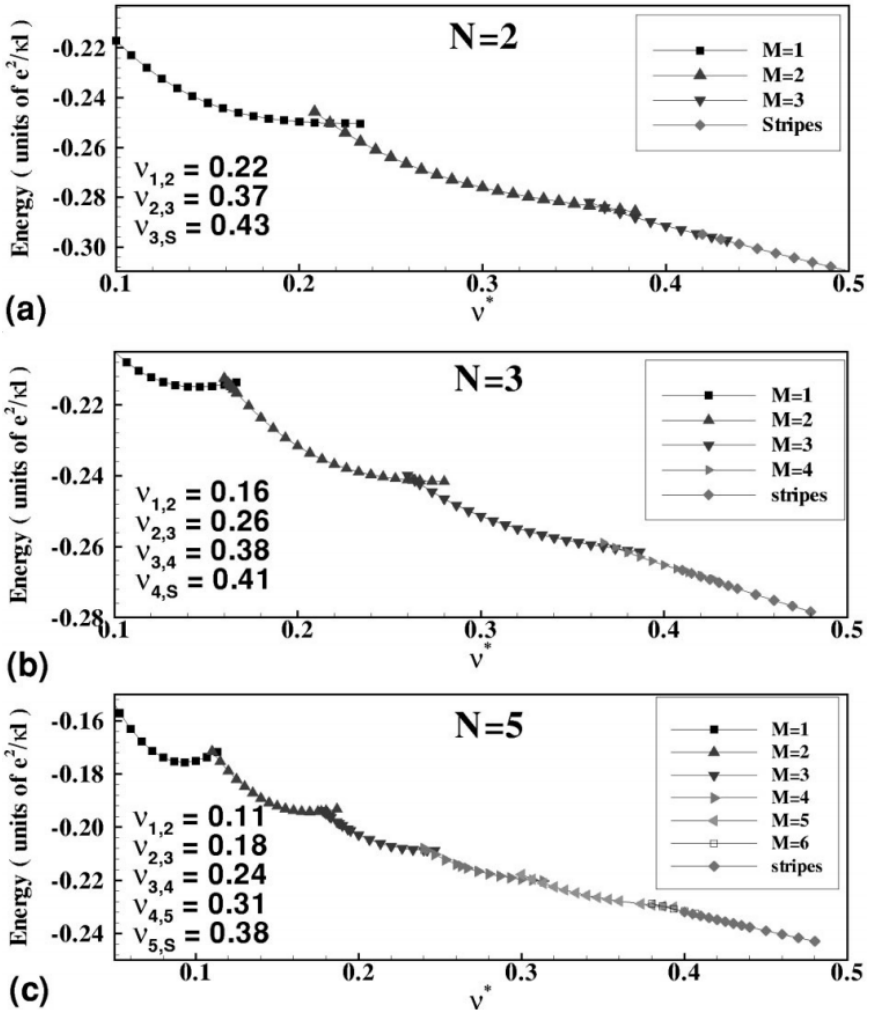

Figure 2.6. Competing cohesive energy of bubble and stripe phases calculated by Hartree-Fock theory throughout the partial filling factor range in the N=2, N=3, and N=5 Landau levels. The proliferation of multi-electron bubble phases with the increasing Landau level index can be identified. Reprinted figure with permission from Ref. [79]. Copyright © 2003 by American Physical Society.

After the discovery of the RIQHSs, the bubble phase description of the RIQHSs has been investigated with different measurement techniques. The standard magnetotransport measurements [66, 67, 102, 107] confirmed the integer-quantized Hall resistance and the vanishing longitudinal resistance due to the localization in bulk and the dissipation-less transport through the edge. The temperature-dependent magnetotransport measurements [37, 73, 110] revealed the unique temperature-dependent signatures of the RIQHSs in the longitudinal resistance which distinguish the states from the IQHSs and FQHSs and from which the onset temperatures are defined. The studies on the DC-current breakdown of RIQHSs [38, 39, 68, 105, 106] and the microwave resonance of the bubbles [71] investigated the depinning and pinning mechanism of the RIQHSs. Alternative to the standard electronic transport, the transport in Corbino geometry [40, 70, 82], thermal transport [112], and the transport of surface acoustic waves (SAW) [74, 75, 83] have been studied to reduce the conducting edge effect and focus on the bulk localization of electron bubbles.

Although the results of different experimental techniques support the electron bubble picture of the RIQHSs, the sandwich structure of quantum well restricts direct observation of bubble morphology and none of the experiments could confirm the formation of bubbles in the RIQHSs. Furthermore, not a negligible discrepancy still lied in between the bubble theory and the experimental results. None of the predicted multiple bubble phases within a high Landau level have been observed, and as a result the proliferation of bubbles in higher Landau levels was unlikely.

My research in this thesis are the works on solving this problem. In the first work, I observed the multiple RIQHSs in the N=3 Landau levels which are associated with M=2 and M=3 bubble phases. This work confirms the possibility of proliferation of bubbles in high Landau levels, as a result, strongly supports the bubble description of the reentrant interger quantum Hall states. In the second work, I compare the energetics of newly resolved M=2 and M=3 bubbles in the N=3 Landau level as well as those of M=2 bubbles in the N=2 Landau level. Here, I first found the M=3 bubbles are more stable than M=2 bubbles in the N=3 Landau level indicating that

the multi-electron bubbles with higher electron number M are more stable within a Landau level. Secondly, I found distinct and Landau level independent energetic features of M=2 and M=3 bubble phases throughout the N=2 and N=3 Landau levels. These results underline the effect of the number of electrons per bubble M on multi-electron bubble energetics and are expected to contribute on the development of existing Hartree-Fock theories.

2.3 Nematic Phases

Nematic phases are the electron solids arranged in the shape of stripes in the Hartree-Fock theory. The half-filled states from $\nu = 9/2$ to $\nu = 11/2, 13/2, 15/2, ...$ in the N=2 and higher Landau levels are the most representatively known nematic phases.

The experimental discovery of nematic phases in the quantum Hall system was first made at the filling factors of $\nu = 9/2, 11/2, 13/2, 15/2, ...$ by M. P. Lilly et al. [66] and R. R. Du et al. [67] respectively in 1999. Here, they found the anisotropy of the two longitudinal resistances along the two perpendicular crystal directions in the half-fillings. The longitudinal resistance R_{yy} along the [110] crystal direction has the minima which indicate the parallel to the direction of the electron stripes, and the longitudinal resistance R_{xx} along the $[1\bar{1}0]$ crystal direction has formidable values making peaks implying the perpendicularity to the direction of the electron stripes.

The nematic phase is roughly divided into two categories based on the Landau symmetry breaking picture, one *smectic phase* and the other *nematic phase* [87, 103]. The terminology setting for the nematic phase is tricky in the sense. The smectic phase looks more stripe like compare to the nematic phase. It has both broken rotational symmetry and broken translational symmetry. On the other hand, the nematic phase looks more randomly distributed but still in the shape of stripe. It has broken rotational symmetry, but the translational symmetry is preserved. The

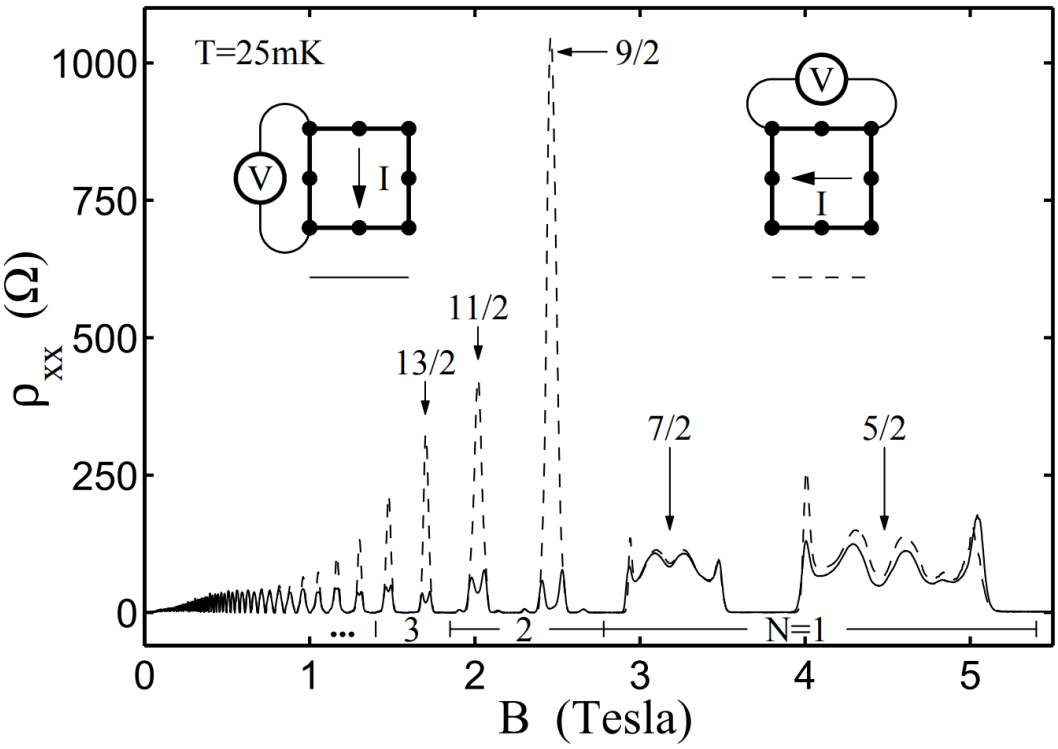

Figure 2.7. One of the two earliest observations of nematic phases by M.P. Lilly et al. [66]. Anisotropy of the two perpendicular longitudinal resistances at the half-fillings from $\nu = 9/2$ indicates the nematic distributions of electrons. Reprinted figure with permission from Ref. [66]. Copyright © 1999 by American Physical Society.

smectic phase is predicted to appear at ultra-low temperature in ultra-pure samples whereas the nematic phase to emerge at higher temperature and disorder condition.

Conventionally, the direction which electrons sit along and as a result has the minima in the longitudinal resistance is called *easy axis* and the direction perpendicular to the electron stripes and as a result possesses the peaks in the longitudinal resistance is called *hard axis*. Although there is no symmetry breaking term in the nematic theory, hard and easy axes are determined spontaneously and this is called *spontaneous symmetry breaking*. Most time in the GaAs/AlGaAs quantum wells, [110] direction is easy axis and $[1\bar{1}0]$ direction is hard axis.

However, with the tuning of different parameters such as in-plane B-field, electron density, and temperature, phase transitions between the nematic and isotropic phases can be realized. Furthermore, tuning these parameters can even flip the easy and hard axes. Investigating novel nematic phase transitions in the quantum Hall system is getting more attention due to the close relation to the pairing potentials. The emegence of nematicity in the vicinity of cooper paring phases in high temperature superconductors as well as the recently observed topological to nematic phase transitions in the $\nu = 5/2$ FQHS support the idea. Further understanding on the nematicity seems crucial to realize and manipulate the exotic paired states hosting high temperature superconductivity and the non-Abelian quasiparticle excitations.

3. EXPERIMENTAL METHODS

The area of study in condensed matter physics conducted in our lab is often referred as *low temperature physics*. To realize and detect novel quantum phases and their smallest behaviors, our lab is armed with different low temperature experimental techniques. Quick and convenient 1K dipper system for preparatory experiments as well as one of the coldest dilution refrigerators in the world equipped with home-made ^{3}He immersion cell are the examples. Further with the samples grown by the cutting edge technology of our collaborators, we expect to see novel quantum states and their intriguing behaviors.

3.1 Two-Dimensional Electron Gas (2DEG)

3.1.1 GaAs/AlGaAs Quantum Well

Among the 2DEG confined in many different systems, we investigate the 2DEG in GaAs/AlGaAs. GaAs/AlGaAs is the most traditional two-dimensional electron system (2DES) which is in the frontier of 2DEG study. The legendary observations of integer and fractional quantum Hall states as well as exotic electron solid phases were observed in the GaAs/AlGaAs system for the first time.

The 2DEG in GaAs/AlGaAs is the purest non-relativistic two-dimensional electrons with single valley. Among different materials, GaAs/AlGaAs achieves the highest mobility of 2DEG [56]. To explore novel strongly correlated phases, achieving high mobility from reducing disorders in a system is critical, since disorder effects can dominate the electron-electron interaction and prevent the emergence of resulting phases. Since GaAs/AlGaAs achieves the highest mobility of 2DEG, so far the richest family of strongly correlated phases are found in GaAs/AlGaAs compared to other materials hosting 2DEG such as graphene, ZnO, transition metal dichalcogenides (TMDs), and

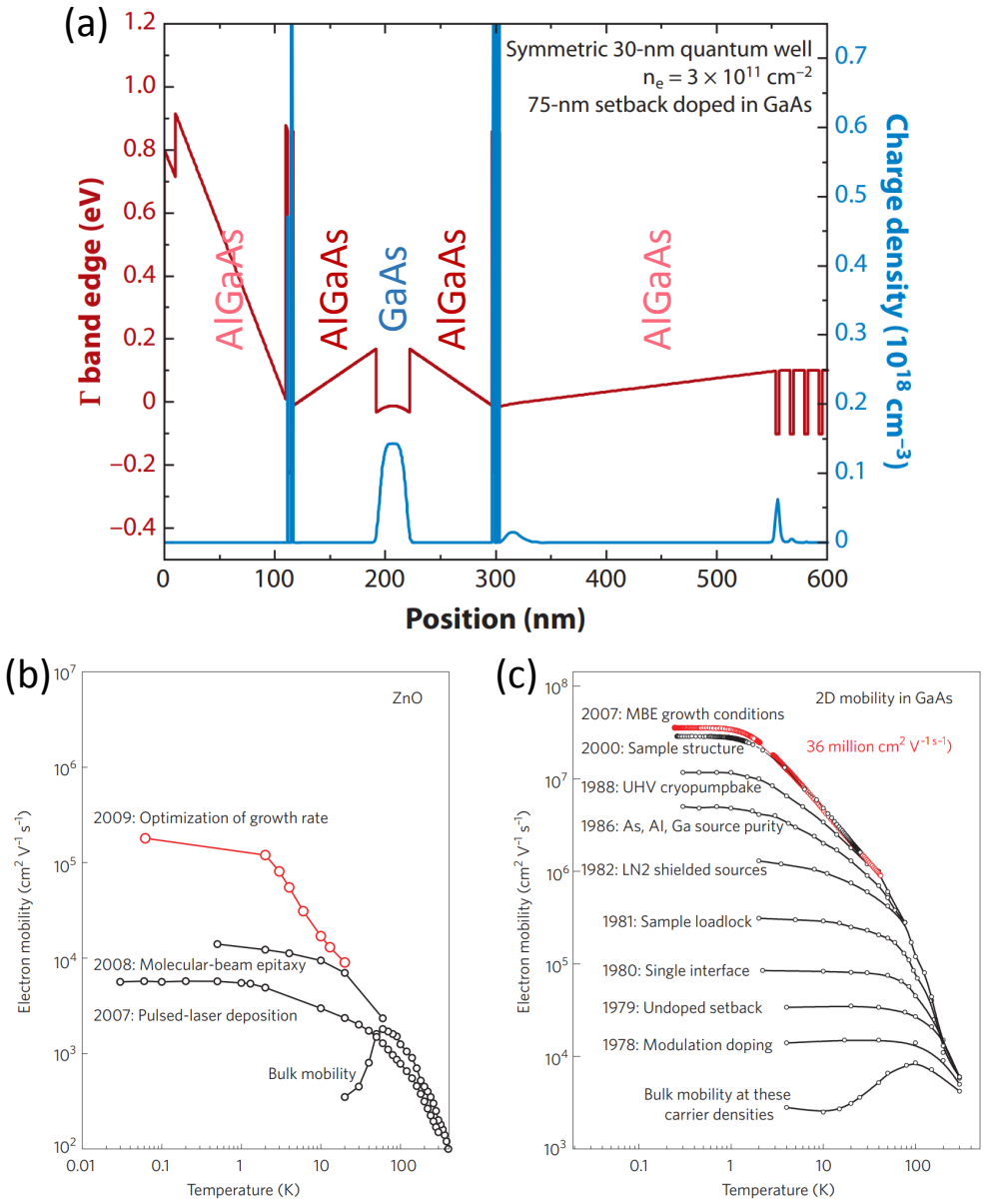

Figure 3.1. (a) The 2DEG realized in GaAs/AlGaAs quantum well. The conduction band profile in GaAs/AlGaAs makes a quantum well structure. The higher energy level of AlGaAs confines the electrons in the GaAs region and quantizes the kinetic energy of electrons along the z-direction. The abundant charge density at GaAs region indicates the presence of 2DEG. (b) ZnO and (c) GaAs mobility improvement history. Reprinted figures with permission from Ref. [56] and Ref. [57]. Copyright © 2014 by Annual Reviews. Copyright © 2010 by Springer Nature.

the surface of 3D topological insulators (TIs). Furthermore, the dispersion relation of 2DEG in GaAs is parabolic. This resembles that of free electron in space rather than relativistic particles such as the photon or those in Dirac materials (graphene and surface of 3D TI) which have linear dispersion relation. In addition, the single valley structure of GaAs provides the simple condition for investigating novel electron-electron interactions excluding multiple valley effects.

We typically use 30nm-wide modulation-doped GaAs/AlGaAs quantum well as our sample. In our sample, the electron density varies in the order of $n = 10^{10}$ to 10^{11} cm^{-2} and mobility varies $\mu = 10^6$ to 10^7 cm^2/Vs. For example, one of our low density samples has density $n = 6.13 \times 10^{10}$ cm^{-2} and mobility $\mu = 9.1 \times 10^6$ cm^2/Vs while one of our high mobility samples has density $n = 2.8 \times 10^{11}$ cm^{-2} and mobility $\mu = 15 \times 10^6$ cm^2/Vs. There are reasons that the quantum well width is decided to be around 30 nm for a regular size quantum well. If the well is too narrow, different impurity effects such as ionized impurities from doping layer and interface roughness can affect on 2DEG energetics preventing the emergence of correlated states [57]. In contrast, if the well is too wide, the subbands in quantum well describing the kinetic energy of 2DEG along the z-direction become too close each other. As a result, there is a risk of populating the second subband in the quantum well when the electron density is high. If the second subband is populated, the electrons confined in GaAs cannot be regarded as pure 2DEG anymore, since the distribution of probability density along the z-direction is occurred through the wavefunction of the second subband which has two antinodes.

3.1.2 Sample Preparation

Once we receive GaAs/AlGaAs wafers grown by our collaborators, the sample preparation process, which is transforming a wafer into measurable devices, starts. The first step of our sample preparation is cleaving a GaAs/AlGaAs wafer into a small square piece. To cut a wafer into a smaller piece, we proceed the following steps. 1)

Make a tiny scratch at the edge of the wafer with a diamond tip cutter. 2) Note the orientation of crystal direction on the note. This process is very important especially if one is planning to measure the anisotropy of resistances along two different crystal axes. 3) Flip the wafer and cover it with filter paper. 4) Gently roll the roller on the scratch covering with the filter paper. 5) When the wafer is cleaved, you can feel it. Then stop the rolling and cut the other side. Since our GaAs/AlGaAs wafers is a pure crystal, a little dent on the wafer can cut it into perfect straight line. We typically use 4×4 mm^2 as sample size.

Once we have a 4×4 mm^2 wafer, we start to make contacts. The first step of contact fabrication is annealing process. To connect the surface of sample with the 2DEG confined in GaAs region which is isolated from the surface by AlGaAs, annealing process is required. We first solder In/Sn (eutectic indium) on the surface of sample. We use 360°F or around as soldering temperature. Here, we use a vacuum chuck to hold the sample to avoid possible contamination while holding the sample using different method. In this step, sample cleanness is extremely important since the sample will go through the high temperature annealing process. If contamination is made especially on the surface of the sample, diffusion of the contaminator may harm the quality of 2DEG. When In/Sn is soldered, it is important that each contact touches the edge of the sample to measure the edge behavior of the quantum Hall system. We either make 8 contacts for bigger sample or 4 contacts for smaller sample in van der Pauw geometry. By making the sample geometry square instead of rectangle, the resistance becomes equivalent to the sheet resistance and we can avoid the extra calculation to extract the resistivity which is same with the sheet resistance in two-dimension.

After finishing soldering the In/Sn, we mount the sample on our home-made annealing station in Fig 3.2(b). Here, the ultimate goal is to anneal the sample at 450°C for target annealing time. We typically use 3 minutes for our sample but we also use from 1 minute to 10 minutes depending on the location of 2DEG in the sandwich structure. The annealing process is as follows. (1) Open the glass body,

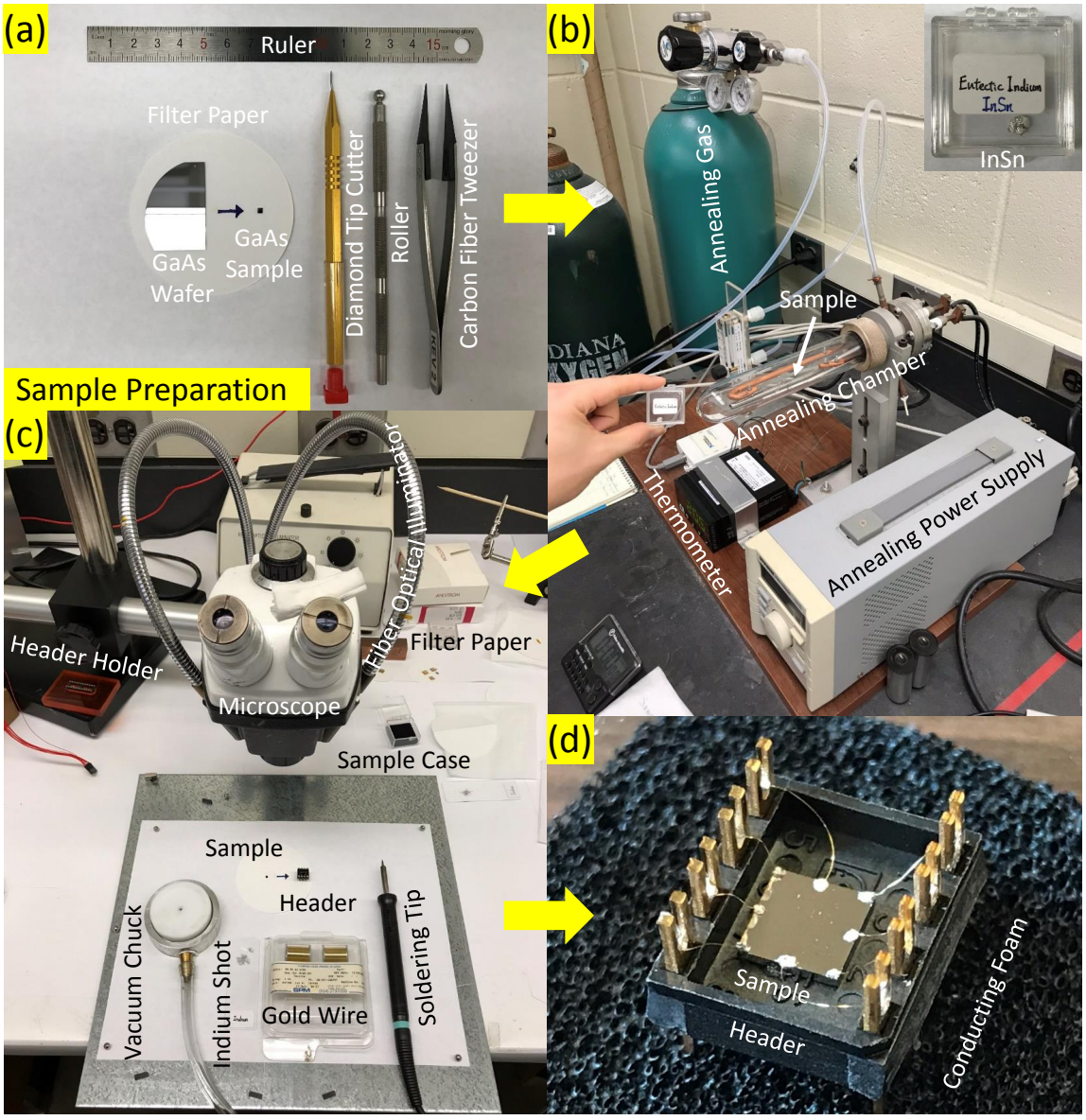

Figure 3.2. (a) Left: a GaAs/AlGaAs wafer and a cut sample on filter paper. Right: cleaving tools. We use a diamond tip cutter to make a scratch and a roller to gently push the scratch covering with a filter paper. Carbon fiber tweezers are used for softer grab. (b) Home-made annealing station: annealing gas, chamber, and power supply. Eutectic In/Sn is shown in the inset. (c) Microscope station with soldering tools. The tools include vacuum chuck, indium shot, gold wire, soldering tip, a header, and a header holder (orange square). (d) A well-made sample on a header for dipper experiment.

put the sample on the annealing plate which has thermometer attached right below, and close the glass body. (2) Flush out the air with the annealing gas (90% nitrogen and 10% hydrogen) for 5 minutes with the flow rate of 5 SCFH (standard cubic feet per hour). Keep the gas flowing for entire annealing process. (3) Heat the annealing plate at 90°C for 5 minutes for warming up the system. (4) Heat the annealing plate at 110°C for 5 minutes to evaporate the moisture remaining inside. (5) Heat the annealing plate at 450°C for 3 minutes (or target annealing time) to diffuse the In/Sn into 2DEG. (6) Turn off the heating power immediately and flush the annealing gas for about 10 more minutes to cool the system down to room temperature. (7) Wait until the system cools down to 30°C, open the glass body, and retrieve the sample.

The next step is attaching thin gold wires to each contact in the sample with indium soldering and mounting the entire system on a header or a cell. For this process, we can also use the vacuum chuck to hold the annealed sample; however, I prefer to use the double-sided kepton tape since the vacuum chuck is limited to rotation and too noisy. We use .001"/0.001inch/25μm thin gold wire and 99.9% indium shots for the process. We use 360°F or around as soldering temperature also for the pure indium (not only for the eutectic indium). Since indium gets easily oxidized, it is important to clean the tip frequently with glass slides. If indium is oxidized, indium does not stick easily. Once the wire soldering process is done, you can see the sample looking like a spider.

The next step is mounting this spider shaped sample on a header or a cell. Before mounting the sample, a header should be trimmed properly to fit in our dipper system which has constrained space. If a sample is mounted on non-trimmed header accidentally, one need to unmount the sample, trim the header, and mount the sample again to avoid the destruction of sample. To mount the sample on the trimmed header, we first apply really tiny amount of rubber cement using the back side of a Q-tip. Then, gently mount the spider shaped sample on the rubber cement, considering the position of the gold wires. Here, if gold wires are arranged to touch each of the pins on the header, it is very convenient when one solders the wires on the pins avoiding using

two hands to hold a wire and the soldering tip simultaneously. To add a personal tip for soldering, both hands should be used for holding the soldering tip to sensitively control and to avoid the accident miscontrol of weaker hand. After soldering all the gold wires on the pins stably, cut the wires with a small nail scissors. Finally, move the sample header safely in a small plastic box equipped with conducting foam and the wafer information labelled.

3.2 1K Dipper System

Once a sample is prepared to be measured, before we measure with dilution refrigerator, we first conduct the preparatory measurement using the 1K dipper system. Measuring with dilution fridge is a time, energy, and money consuming process. The complicated preparation process of dilution fridge including electrical check, vacuum sealing, connecting hoses, inserting the fridge unit to dewar, and etc. takes at least one day. Moreover, once the fridge unit is inserted in the dewar, liquid helium boils off about 30% of the liquid helium capacity of our fridge per day which is about 15L/day. Based on the market price of liquid helium, which is more or less \$2000/100L, this costs about \$300 per day. In contrast, with the dipper system, we can finish the preparation process within 2 hours including lowering the sample temperature down to liquid helium temperature. Also, the similar amount of helium boils off when the dipper is in, compare to the amount of helium boils off naturally in a dewar, which is about 1.5L/day. Therefore, the dipper measurement is the first step of our experiments to check the sample condition before measuring with the fridge.

3.2.1 Structure of 1K Dipper System

The dipper can be thought as small fridge without dilution unit. It is designed to directly dip in the ubiquitously used commercial helium dewar to use the cooling power of liquid helium. The outer part material of dipper is made of G-10, which is an excellent thermal insulator and robust against thermal contraction and expansion.

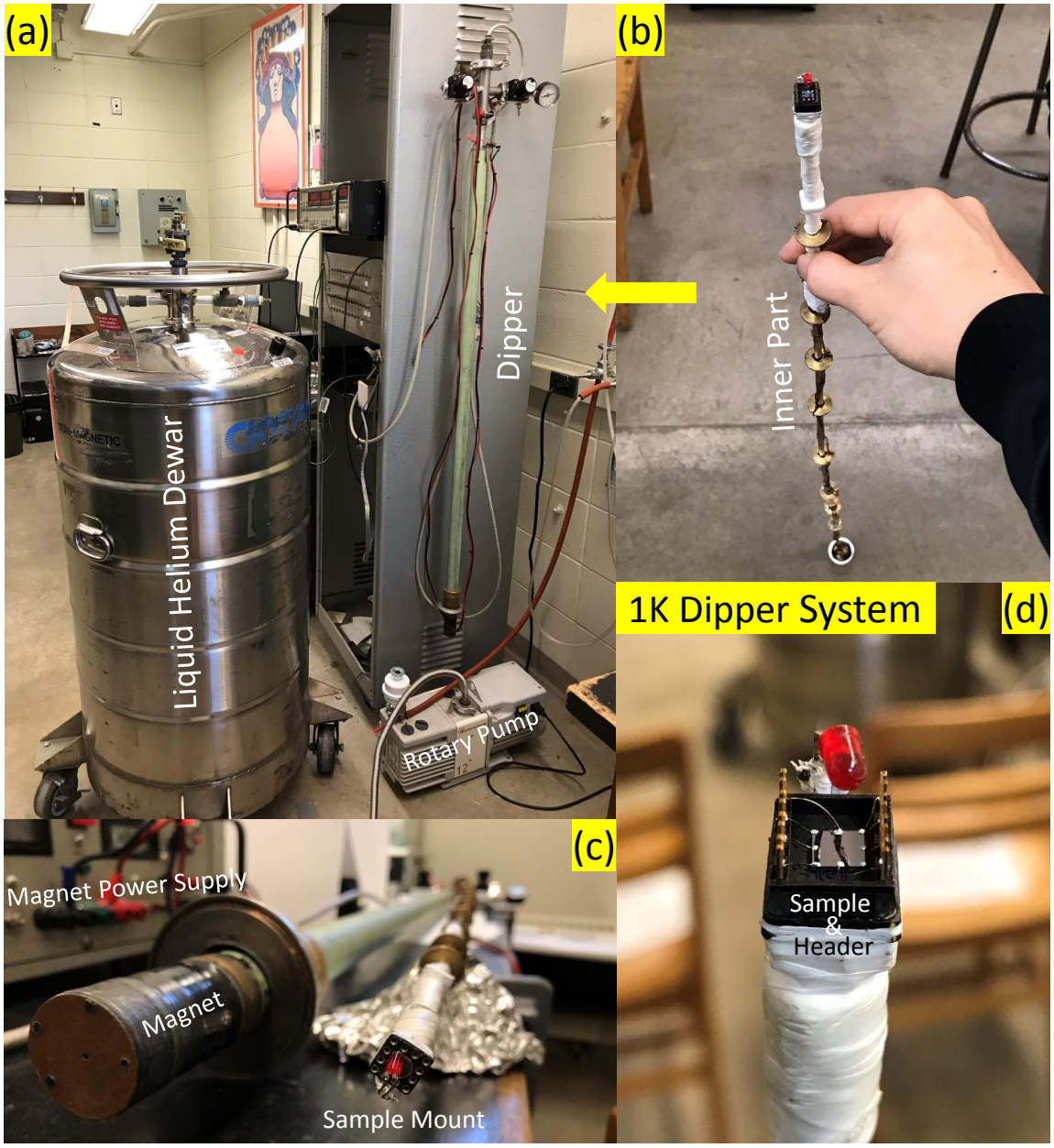

Figure 3.3. (a) The dipper and a liquid helium dewar. The dipper is designed to directly dip in the helium dewar. The outer part is made of G-10. A rotary pump is used to lower the temperature down to 1K. (b) The inner part of dipper. Brass disks are designed to prevent the radiation. (c) Dipper magnet (black), magnet power supply (left), and sample mount (right). (d) A sample is mounted. A red LED is equipped for the 10K illumination for GaAs sample.

The G-10 outer part thermally insulates the inner part from the room while keeping its shape from the continuous cool downs. The inner part of dipper is made of stainless steel. The inner part should be non- or less-conducting to thermally isolate the sample from room temperature. It also should not be magnetic as all the other cryogenic components possibly exposed to magnetic field. One of the interesting features of the inner part is attached brass disks. The eight brass disks are equipped to block the radiation from the room to sample. At the end of the inner part, sample mount area exists. Here, a red LED is equipped for the 10K illumination technique for GaAs sample.

At the end of the outer part of the dipper, a superconducting magnet is furnished. This magnet is operated by the power supply in Fig. 4.3(c). The length of the inner part is adjusted to perfectly locate the sample mount area in the middle of the magnet. Below the magnet, there is a small hole where the liquid helium flows into. The liquid helium flows into the space inside the magnet where the real outer part of dipper is locating. Another smaller hole exists at the real outer part of dipper. Through this smaller hole, the outer and inner parts of dipper are connected. The liquid helium flows into the inner part of the dipper where sample is located. In this way, liquid helium touches our sample directly. To control the amount of helium flowing through the smaller hole, a thin wire impedance is plugged inside the smaller hole.

With the above arrangement, a sample can cool down only to around 4K close to the boiling point of liquid helium at 1 atm. However, to cool down the temperature to around 1K, a rotary pump is required. Once the dipper is completely lowered down to the bottom of the dewar, a rotary pump can be connected to the dipper through a valve attached on the top of dipper. With the rotary pump, we can lower the pressure inside the dipper, and as a result, the temperature of liquid helium touching the sample inside the inner part of the dipper drops to around 1K.

3.2.2 Operation of 1K Dipper System

The operation procedure of dipper system is similar to that of dilution fridge without operating the dilution unit but much simpler. The procedure is as follows. (1) Take the inner part of dipper out; plug in the sample header on the mount and arrange the position of LED; conduct the electrical check on the sample and LED; if everything looks good, put the inner part back inside the dipper and seal it with a clamp. (2) Pump out the air inside the dipper and flush in the ultra high purity 99.999% helium gas inside the dipper. Repeat this process two more times. Filling the helium in should be the last step not pumping the gas out. (3) Flush in the pure helium to the small space inside the magnet through the small hole below the magnet. (4) Connect the magnet wires to HP multimeter and start measuring the magnet resistance as thermometer. (5) Open the dewar cap and place the dipper on the top of the dewar with a clamp holder holding the body of dipper to prevent the accidental sliding. (6) Lower the dipper slowly to the bottom of the dewar checking the magnet resistance. This process should take more than 30 minutes to avoid destruction of the system or sample from abrupt thermal contraction. (7) Once the magnet resistance saturates to zero, connect the magnet wires to the magnet power supply; and connect the HP multimeter to RuO thermometer equipped inside the dipper and measure the temperature. (8) The experiment can start once the resistance of RuO thermometer becomes stable. (9) To lower the temperature down to around 1K, connect the rotary pump to a valve on the dipper. The air inside the hose must be pumped out before opening the valve. Once the hose is cleaned, open the valve slowly. The temperature will drop as the pressure drops. (10) To increase the temperature of the system for shining the LED at 10K, pull the dipper up accordingly checking the RuO thermometer. (11) Once the experiment is over, to warm up the system, pull up the dipper half way from the dewar and wait for about 15 minutes. As soon as the dipper is pulled up, paper towers should be wrapped on the body of dipper to prevent water from flowing inside the dewar. (12) Then, pull

up the dipper all the way to the top and wait until the magnet resistance reaches to 3.4 kΩ, which is nearly the room temperature resistance 3.8k Ω. Magnet should be warmed up nearly to the room temperature before retrieving the dipper from the dewar to prevent magnet getting moisturized. This step takes about 30-40 minutes. (13) Once the magnet resistance reaches to 3.4 kΩ, retrieve the dipper out from the dewar, put it on the table, and start drying the magnet with our air flowing setup as soon as possible. When the magnet resistance reaches to 3.8k Ω, stop the air flow. The sample can be retrieved from this point. Typically, we flow the air for about 30-40 minutes.

3.3 Dilution Refrigeration

In order to detect some of the most delicate changes of quantum states, temperature of a few millikelvin or lower is required. Up to date, dilution refrigeration using the mixture of ^{3}He and ^{4}He is the most effective method to cool the temperature of a bulk system below 100 mK. With our dilution refrigerator, one of the coldest dilution refrigerator in the world achieving electron temperature down to around 4 mK, we perform our experiments.

3.3.1 Principle of Dilution Refrigeration

The cooling power of dilution refrigeration comes from the latent heat required to mix the two separated phases in the ^{3}He and ^{4}He mixture: ^{3}*He concentrated phase* and ^{3}*He dilute phase* [58]. Below 867 mK, if the ^{3}He concentration is larger than a certain percentage, the ^{3}He and ^{4}He mixture separates into the two phases. One is the ^{3}He concentrated phase which is pure ^{3}He and the other is ^{3}He dilute phase which is ^{4}He mostly plus the certain percentage of ^{3}He. This certain percentage is temperature dependent; for example at 0K, this value is 6.6%.

One remarkable fact here is there is maximum percentage of ^{3}He occupation in the dilute phase, which is 6.6% of ^{3}He at 0 K [58]. This means, at 0 K, if the 10% of

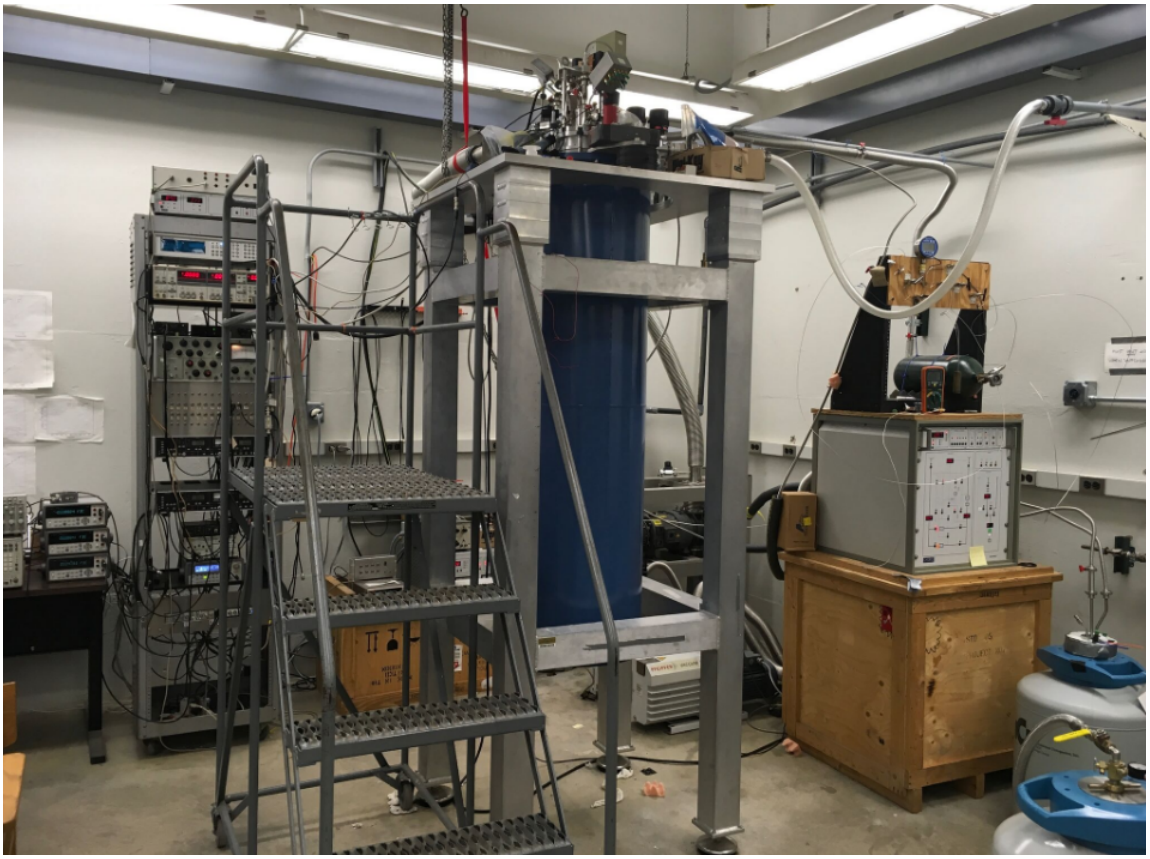

Figure 3.4. Our lab's dilution refrigerator system. Left: lock-in amplifiers. Middle: dilution refrigerator. Right: control panel.

mixture is ^{3}He, the 6.36% is in the dilute phase and the rest of 3.64% exists separately as the concentrated phase. This concentrated phase will be on the top of the dilute phase due to its lower density. As the ^{3}He in the concentrated phase passes through the boundary of the two phases and mixes with the dilute phase, the latent heat which is required for the mixing is supplied from the internal energy of the mixing chamber [58, 59].

The ^{3}He in the concentrated phase can pass through the boundary of the two phases only when there is a vacancy in the 6.6% of ^{3}He in the dilute phase [58, 59]. In order to create the vacancy, the ^{3}He in the dilute phase is evaporated in the place called still and pumped out with a rotary (vane) pump. As the evaporated ^{3}He is pumped out, it goes out from the fridge, passes the ^{3}He-rotary pump, passes the

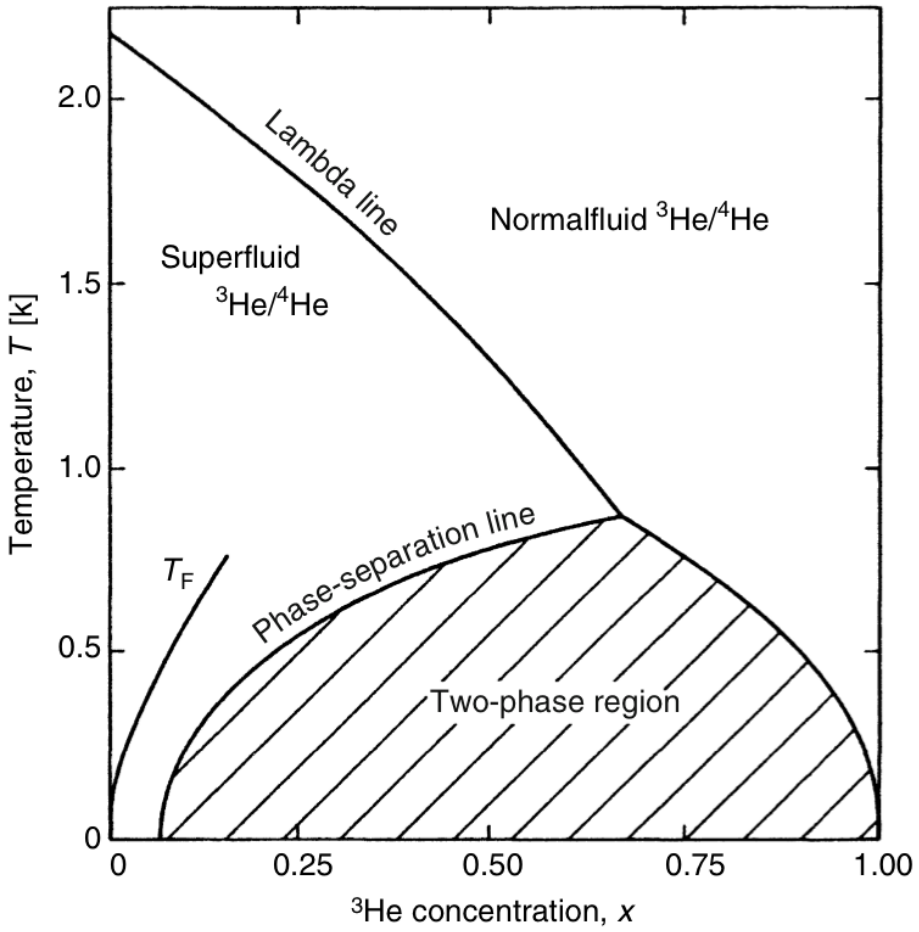

Figure 3.5. The phase diagram of ^{3}He and ^{4}He mixture. The phase separation starts to occur at the highest temperature of 867 mK [58]. Reprinted figure with permission from Ref. [58]. Copyright © 2007 by Springer Nature.

nitrogen trap, passes the helium trap, and comes back to a place called condenser inside the fridge. In the condenser, the gas ^{3}He condenses into liquid and drips down to the mixing chamber passing the heat exchangers in different stages. Meanwhile in the mixing chamber, as the vacancy of ^{3}He in the dilute phase is created, the ^{3}He in the concentrated phase crosses the boundary of the two phases and refill the maximum percentage of 6.6%. Thanks to this circulation process of ^{3}He, the cooling power from the dilution of ^{3}He in to the dilute phase can be constantly provided.

In addition, to boost the circulating process to cool down the mixing chamber temperature faster at lower temperature, still heater is used to evaporate the liquid ^{3}He faster in the still and a roots pump is used in between the still line and the ^{3}He-rotary pump to blow the gas ^{3}He faster to the ^{3}He-rotary pump.

3.3.2 Structure of Dilution Refrigerator

The structure of dilution refrigerator can be roughly categorized into three independent parts. They are the *dilution unit*, *1K pot*, and ^{4}*He bath*. Helium inside each component is separated and does not mix with one another (except through the needle valve connection between the ^{4}He bath and 1K pot). The dilution unit and 1K pot are mechanically attached as one unit which I call here *fridge unit*. The fridge unit is designed to be detachable from the ^{4}He bath to prevent cooling and warming of the whole system in the sample changing process. In this way, enormous amount of expensive helium can be saved.

Dilution Unit

Dilution unit is the place inside the fridge where the mixture of ^{3}He and ^{4}He circulates. This means the mixture does not pass through the other parts of fridge, which is 1K pot and ^{4}He bath. Dilution unit consists of the three major parts, *mixing chamber*, *still*, and *condenser*.

Mixing chamber is where the dilution cooling process occurs. The phase boundary of the dilute phase and the concentrated phase locates inside the mixing chamber. The dilution process of ^{3}He in the concentrated phase into the dilute phase absorbs heat from the mixing chamber [58,59]. The mixing chamber locates at the end of the fridge unit. Since the gas ^{3}He should be liquefied and cooled down through different heat exchanging process, the mixing chamber locates at the end of the heat exchanging stages. Samples are mounted on a copper tail attached on the plate below the mixing chamber. Since the mixing chamber is the coldest part of the fridge, the copper tail

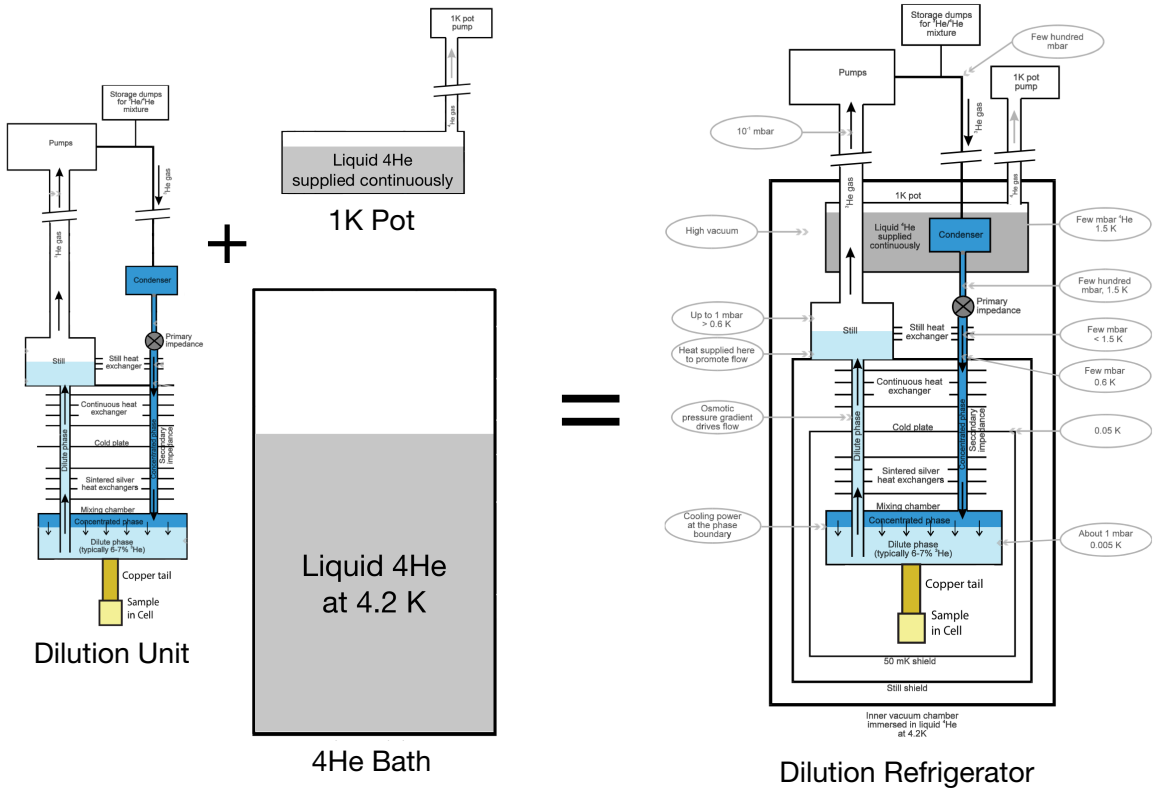

Figure 3.6. The three components of dilution refrigerator: the dilution unit, 1K pot, and ^{4}He bath. Figures adapted with permission from Ref. [59] and Ref. [60]. Image Courtesy to Oxford Instruments. Copyrighted by Katherine A. Schreiber.

and samples are connected to the mixing chamber plate. A copper tail is used to locate the sample in the middle of magnet. In addition, since the phase boundary between the dilute and concentrated phases should locate inside the mixing chamber, if the mixing chamber temperature does not drop to the target temperature, one can suspect the shift of the phase boundary to the outside of the mixing chamber due to the lack of ^{3}He in the mixture.

Still is a chamber where the liquid ^{3}He in the dilute phase evaporates in to gas. To maintain the dilution of ^{3}He into the dilute phase in the mixing chamber, a vacancy

needs to be created in the dilute phase. To evaporate ^{3}He from the dilute phase, the dilute phase needs to be heated up to around 700 mK to maximize the ratio of the vapor pressure of ^{3}He to that of ^{4}He [58, 59]. Thus, a place called still exists, which is connected to the mixing chamber to supply the dilute phase but placed far above and thermally isolated to prevent heating the mixing chamber. As the ^{3}He in the dilute phase evaporates in the still, the ^{3}He of the dilute phase in the mixing chamber is sucked up to the still by osmotic pressure, and as a result, the ^{3}He of the concentrated phase crosses the phase boundary of the two phases and refill the maximum percentage of 6.6% in the mixing chamber [58, 59]. The evaporated ^{3}He in the still is pumped outside the fridge by the ^{3}He-rotary pump and comes back to the condenser after passing through the roots pump, ^{3}He-rotary pump, nitrogen trap, and helium trap in the order. Below 300 mK, in order to boost the circulation process to cool down the system faster, the still is heated with an attached heater typically with 3 mW while the roots pump is turned on.

Condenser is a chamber where the gas ^{3}He coming into fridge from outside condenses into liquid. It is physically attached to the 1K pot (above the still) and uses the cooling power of the 1K pot to condense the gas ^{3}He. Once the gas ^{3}He condenses into liquid, it drops down to the mixing chamber passing different heat exchanging stages. To clarify, the evaporated ^{3}He from the still condenses into liquid for the first time in the condenser before dropping down to the mixing chamber. The room temperature ^{3}He and ^{4}He mixture from the dump also condenses first typically in the condenser (or still). This step is called condensing.

In addition, there are couple of *heat exchangers* to efficiently cool down the incoming ^{3}He from the condenser to the mixing chamber and warm up the outgoing dilute phase from the mixing chamber to still. The heat exchangers thermally connect the warm incoming ^{3}He (from condenser to mixing chamber) and the cold outgoing dilute phase (from mixing chamber to still) in between the still and mixing chamber. Through the heat exchanging process, an amount of power required for cooling the warm ^{3}He as well as heating the cold dilute phase can be saved. This heat exchanging

process is the most crucial and sensitive part of the fridge design which directly affects on the base temperature of the dilution fridge [58, 59]. Our fridge has the extra heat exchanger compare to standard model thus provides cooling power of 500 μW.

1K Pot

1K pot is a chamber which is the second powerful cooling source of the dilution fridge. It exists to provide the cooling power to the condenser. By pumping out the evaporated ^{4}He in the 1K pot with a rotary pump, 1K pot pump or ^{4}He-rotary pump, the temperature of liquid ^{4}He in the 1K pot drops from 4.2K to around 1.5K, because the boiling point drops under the lower pressure. This is same with the cooling principle of the 1K dipper system. The liquid ^{4}He is constantly provided from the ^{4}He bath through the small needle valve and the ^{4}He-rotary pump keeps pumping while the fridge is running. The amount of provided liquid ^{4}He from the bath can be controlled manually by the needle valve. If the needle valve is completely closed, the 1K pot will run out the liquid ^{4}He. 1K pot and condenser are attached closely thus they look as one chamber.

Sorb is a charcoal attached to the 1K pot. It absorbs the exchange gas used to thermally connect the inner vacuum chamber (IVC) and the dilution unit to cool down the dilution unit using the cooling power of 4He bath. Here, the IVC is dipped in the ^{4}He bath. Once the cooling process is done, the exchange gas is absorbed into the sorb to thermally disconnect the dilution unit and the IVC to cool down the dilution unit to lower temperature. Absorbing and releasing of exchange gas is controlled from the temperature control of the sorb. To release the exchange gas, we set the sorb temperature to 12K. And to absorb the exchange gas, we simply stop the temperature control on the sorb which cools the sorb back to the 1K pot temperature.

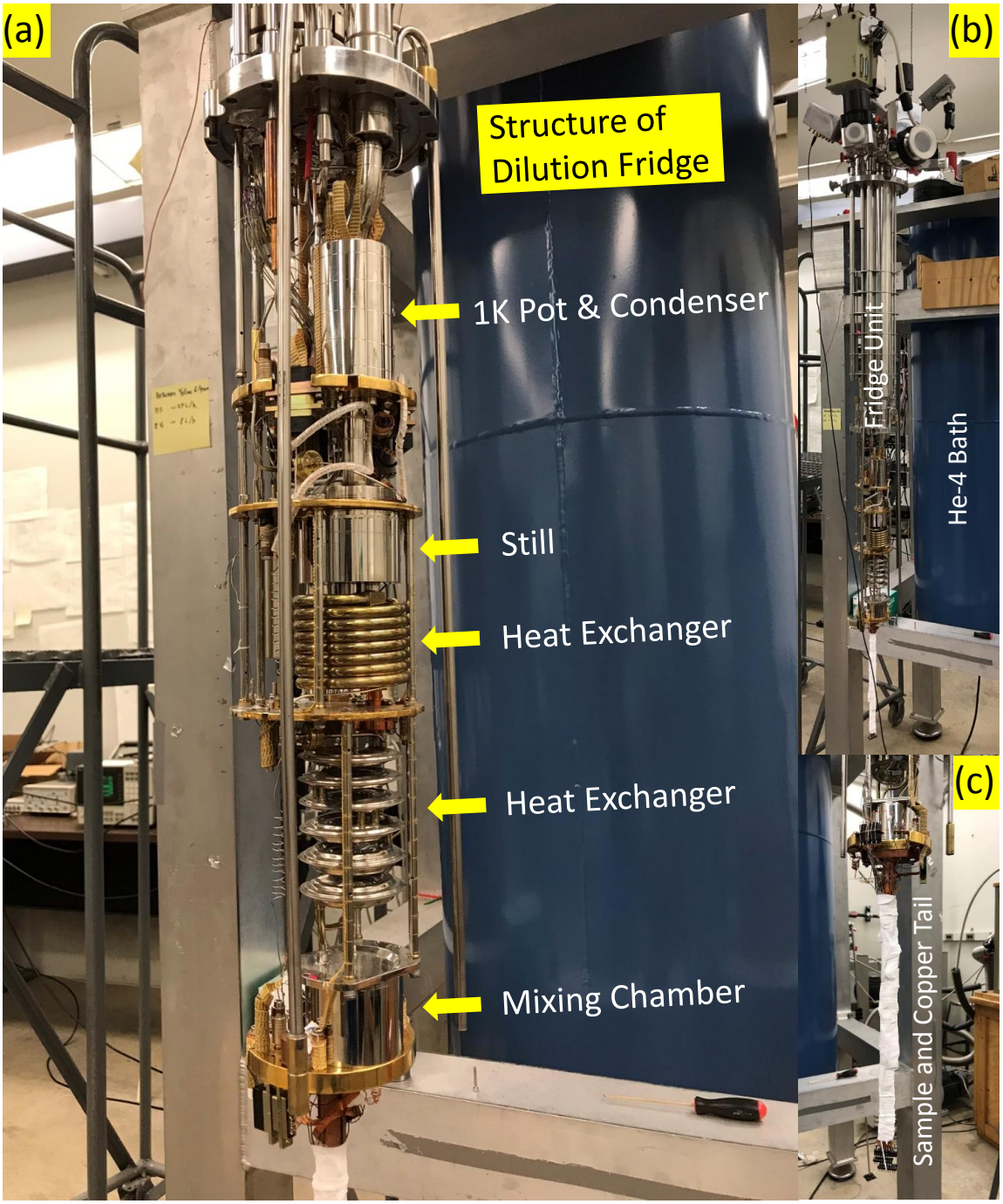

Figure 3.7. (a) Structure of the fridge unit. (b) The two components of dilution fridge: fridge unit and ^{4}He bath. (c) Samples mount on the copper tail attached below the mixing chamber.

^{4}He Bath

^{4}He Bath is the bath of liquid ^{4}He at 4.2K inside the fridge. It is the main protecting layer for the fridge unit from the room temperature heat. To insulate the heat transfer from the room to the fridge unit, the fridge is shielded with a *vacuum jacket* and after that covered with the ^{4}He Bath. Filling up the ^{4}He bath regularly is the most labor and money requiring part of maintaining the *wet dilution refrigerator system*. It needs to be filled up every two days when the fridge unit is inserted and every five or six days when the fridge unit is out. These cost $2000 for every two days (fridge unit in) and five or six days (fridge unit out) calculating with the market price of liquid ^{4}He ($2000/100L). Thus, most people purchasing new dilution fridge these days choose *cryo-free or dry dilution refrigerator system* which has pulse-tube cooling system instead of ^{4}He bath.

External Units: Pumps, Traps, Dump, and Control Panel

There are three pumps in our dilution refrigerator system. They are ^{3}He-rotary pump, ^{4}He-rotary pump, and roots pump. The ^{3}He-rotary pump is necessary to pump out the evaporated ^{3}He from the still. It is constantly on once the circulating is started. The thick still line is connected from the fridge to the ^{3}He-rotary pump. In the middle of the still line, the roots pump exists to boost the circulating process faster below 500mK. The ^{4}He-rotary pump is necessary to pump out the gas ^{4}He from the 1K pot to reduce the vapor pressure to drop the liquid ^{4}He temperature down around 1.5K.

There are two traps in our dilution fridge system. One is nitrogen trap and the other is helium trap. The nitrogen trap is inserted in the liquid nitrogen dewar out side fridge. Once the gas ^{3}He passes the ^{3}He-rotary pump, it heads to the nitrogen trap. Nitrogen trap absorbs the impurities such as oil mist or air that the gas ^{3}He obtained outside the fridge. The nitrogen dewar is usually filled every 6 days when the fridge is running. The helium trap is inserted in the ^{4}He bath inside fridge. Once the

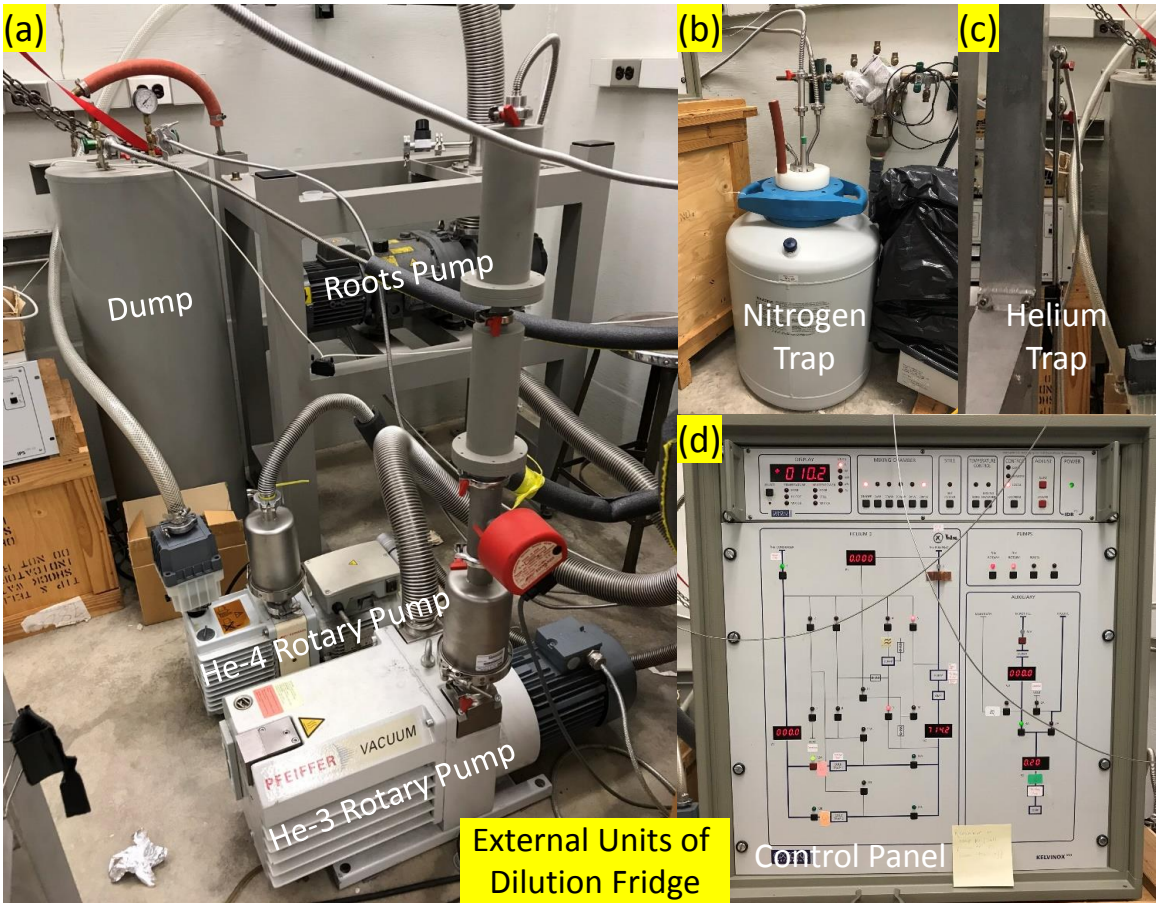

Figure 3.8. (a) The three pumps (^{3}He-rotary pump, ^{4}He-rotary pump, and roots pump) and the room temperature mixture storage, dump. ^{3}He-rotary pump and roots pump are sealed in the closed path of the mixture between the dump and dilution unit. In contrast, the ^{4}He-rotary pump is connected in one way path to the recovery line. The pumps are operated by the control panel in figure (d). (b) The nitrogen trap is inserted in the nitrogen dewar outside the fridge. The nitrogen dewar needs to be filled periodically when the fridge is running. (c) The helium trap is inserted inside the ^{4}He bath while the fridge is running. In the warming up process, the helium trap must be retrieved first before the fridge unit is retrieved from the ^{4}He bath. The pressure inside the helium trap measured at room temperature indicates the amount of impurities absorbed. (d) The control panel. Pumps and valves are controlled by this panel to convey different gases through different channels.

gas helium ^{3}He passes nitrogen trap, before heading to the condenser line, it passes the helium trap first. Similar to the nitrogen trap, helium trap absorbs the obtained impurities in the gas ^{3}He but is operated at the liquid ^{4}He temperature.

Dump is a place where the ^{3}He and ^{4}He mixture is stored once they are retrieved from the dilution unit and other connected lines after finishing an experiment. It is a cylinder container sitting in room temperature. The maximum pressure in the dump must be remembered and checked before finishing the retrieving process not to lose the precious mixture. This value for our system is around 714-719 mbar depending on the room temperature (AC on/off and seasons).

Control panel is where all the controlling valves are located. While the three pumps provide the momentum of the gas transfer, the control panel decides the path of gas by controlling the valves blocking different routes of the gas. The amount of gas in each route can be identified from the pressure shown in the pressure gauge in the path.

3.3.3 Operation of Dilution Refrigerator

The operation procedure of dilution fridge can roughly divided into three steps: *1) cooling the fridge*, *2) condensing & circulating*, and *3) warming the fridge*.

Cooling the Fridge

There are two scenarios of cooling the fridge. One is cooling the fridge unit while the fridge dewar is cold with ^{4}He bath inside and the other is while the fridge dewar is warm at room temperature. Since the former scenario is more frequently used, I will start with the first scenario.

To insert the fridge unit into cold fridge dewar having ^{4}He bath, we follow this procedure. 1) Put a proper tail on the plate below the mixing chamber. 2) Figure out the wire configuration for sample, thermometer, and heater. 3) Mount sample on the tail and thermometer on the mixing chamber plate. 4) Conduct electrical check of

sample, thermometer, and heater. 5) Arrange the coax cables and wires with teflon tape to fit inside the copper shield. 6) Conduct electrical check once more. 7) Close the copper shield and check whether the sample and tail touch the shield through a hole below the shield. They should not touch the shield. 8) To close the inner vacuum chamber (IVC), clean the interface on the fridge unit and on the IVC with ethanol using Kimwipes. Once they are clean, in order to indium seal the interface, apply grease on the proper length of pure indium wire and surround the IVC interface. 9) Close the IVC on the fridge unit and tighten the screws. 10) Pump out the IVC using the rotary pump until the pressure reaches 50 mTorr or below. It takes about 50 minutes. 11) Once the IVC is pumped out, re-tighten the screws. 12) Connect the still and condenser with a tee pipe and pump them out simultaneously with the turbo pump until the pressure reaches less than 2×10^{-5}mbar. It takes more than 3 hours. 13) Clean the needle valve filter with acetone and sonicator. To dry it, flow the ultra-pure helium through the filter until the acetone smell disappears. It takes about 1-2 minutes. Put the filter back and seal the rod with aluminum tape. 14) Put the G-10 shield on. 15) To prepare the 1K pot, pump out the 1K pot with a rotary pump for 10 minutes; flow the ultra-pure helium for 10 minutes while the needle valve is open; close the needle valve and pump out for another 10 minutes. In the last step, 1K pot should be empty. 16) Put ultra-tiny amount of exchange gas using the orange rubber bladder and needle holder. 17) Connect the recovery hose to G-10 and connect the ultra-pure helium hose to the recovery hose. 18) Flush the ultra-pure helium through the G-10 to get rid of air while docking the fridge unit to the fridge dewar. 19) Once the docking is done, connect the G-10 recovery hose to recovery line. 20) Slowly lower the fridge to the bottom while keeping the eyes on the recovery rate. When the fridge unit is stuck around the magnet docking point, pull and push the fridge unit gently along the 11 o'clock direction. The complete lowering process takes about 2 hours and should not be done faster than 1 hour to avoid destruction of the system due to rapid thermal contraction. 21) Connect the pumping lines for the still, condenser, and 1K pot and the electrical lines for the sample, thermometer,

helium level meter, and ground. 22) Check out the pressure in the line in front and behind the nitrogen trap which indicates the amount of impurities collected, record it, and pump them out with ^{4}He-rotary pump. 23) Insert the helium trap into the ^{4}He bath. 24) Pump out the still line with the rotary pump and then with the turbo pump until the pressure reaches below 9×10^{-4}mbar. It takes more than 3 hours. 25) Start condensing.

The second scenario is when the fridge dewar is at room temperature. The fridge dewar is usually cold due to back to back experiments and is kept to be cold since a significant amount of effort is required to cool the warm fridge dewar back to liquid helium temperature. However, if the fridge dewar became warm and needs to be cooled down, we follow this procedure. 1) Follow the 1-16 steps of the first scenario. 2) Insert the fridge unit directly inside the fridge dewar. Since the fridge dewar does not have ^{4}He bath at this moment, the lowering of fridge unit to the bottom can be done immediately. 3) Connect the big pressure gauge, ^{4}He-rotary pump hose, gas nitrogen hose simultaneously at the end of the recovery pipe. Pump out the fridge dewar with ^{4}He-rotary pump and flush in the ultra-pure gas nitrogen. The fridge dewar pressure should not exceed 2 psi. Repeat this two more times. At the end, nitrogen gas should be filled in the fridge dewar. 4) Transfer 40L of liquid nitrogen while the recovery pipe is partially open to the air partially covered with aluminum foil. 5) Check the filling level of liquid nitrogen with the three resistors attached near the fridge magnet. 6) Stop transferring when the gauge in the 100L liquid nitrogen dewar positions in the middle of 1/2 and 3/4. 7) Attach the one way valve at the end of the recovery pipe and wait until all the liquid nitrogen boils off. This takes as much time as liquid helium boils off naturally in the fridge. with the 40L of liquid nitrogen transferred, it takes about 24 hours. 8) Once the sorb temperature reaches 87K (+10K from the liquid nitrogen temperature), wait for 4 hours and then start transferring the liquid helium. The most important thing in this process is boiling off all the liquid nitrogen inside the fridge dewar. If some amount of liquid nitrogen is left in the fridge dewar, enormous amount of liquid helium boils off to cool down the

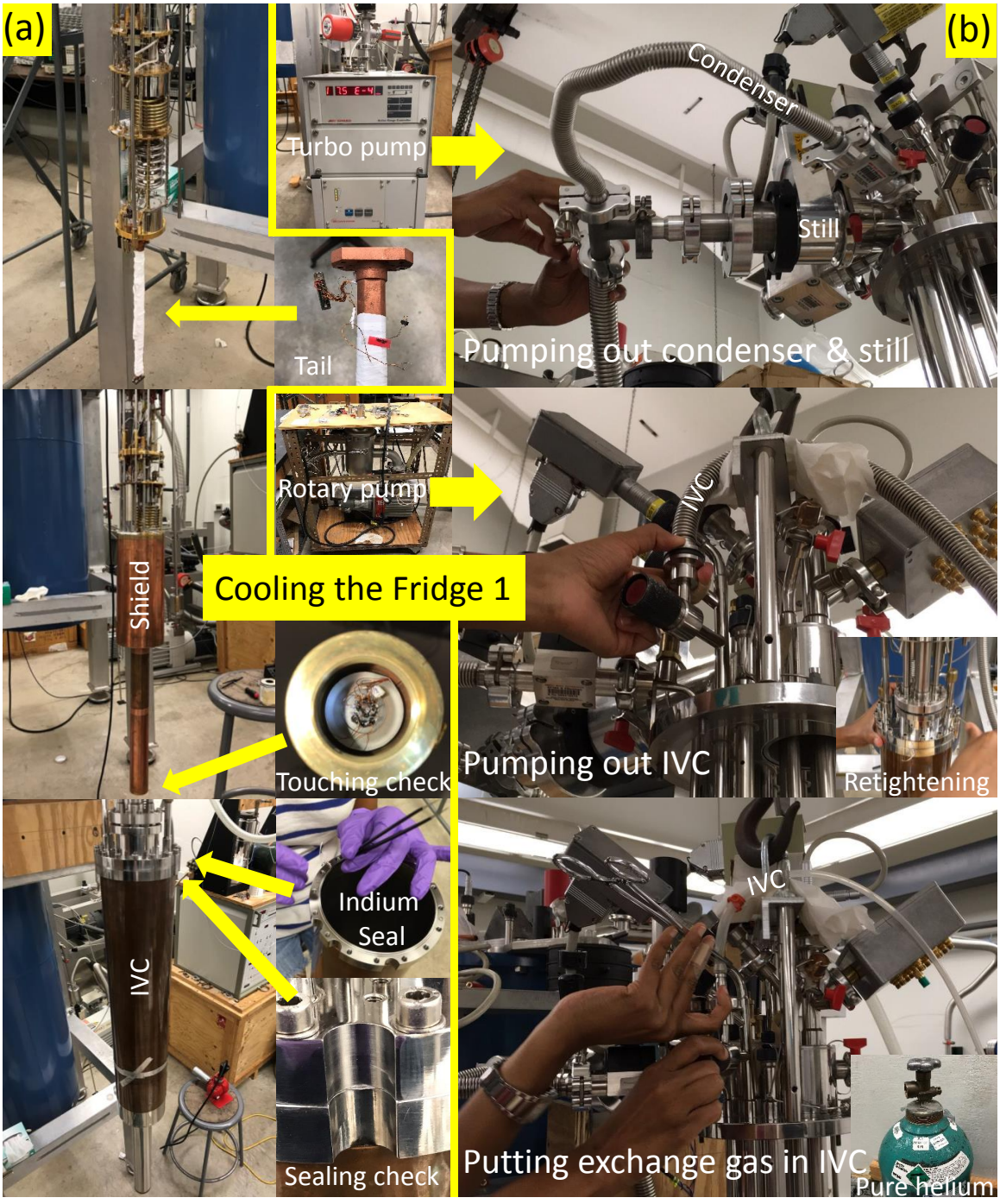

Figure 3.9. (a) Sealing parts of the fridge cooling process. (b) Pumping parts of the fridge cooling process.

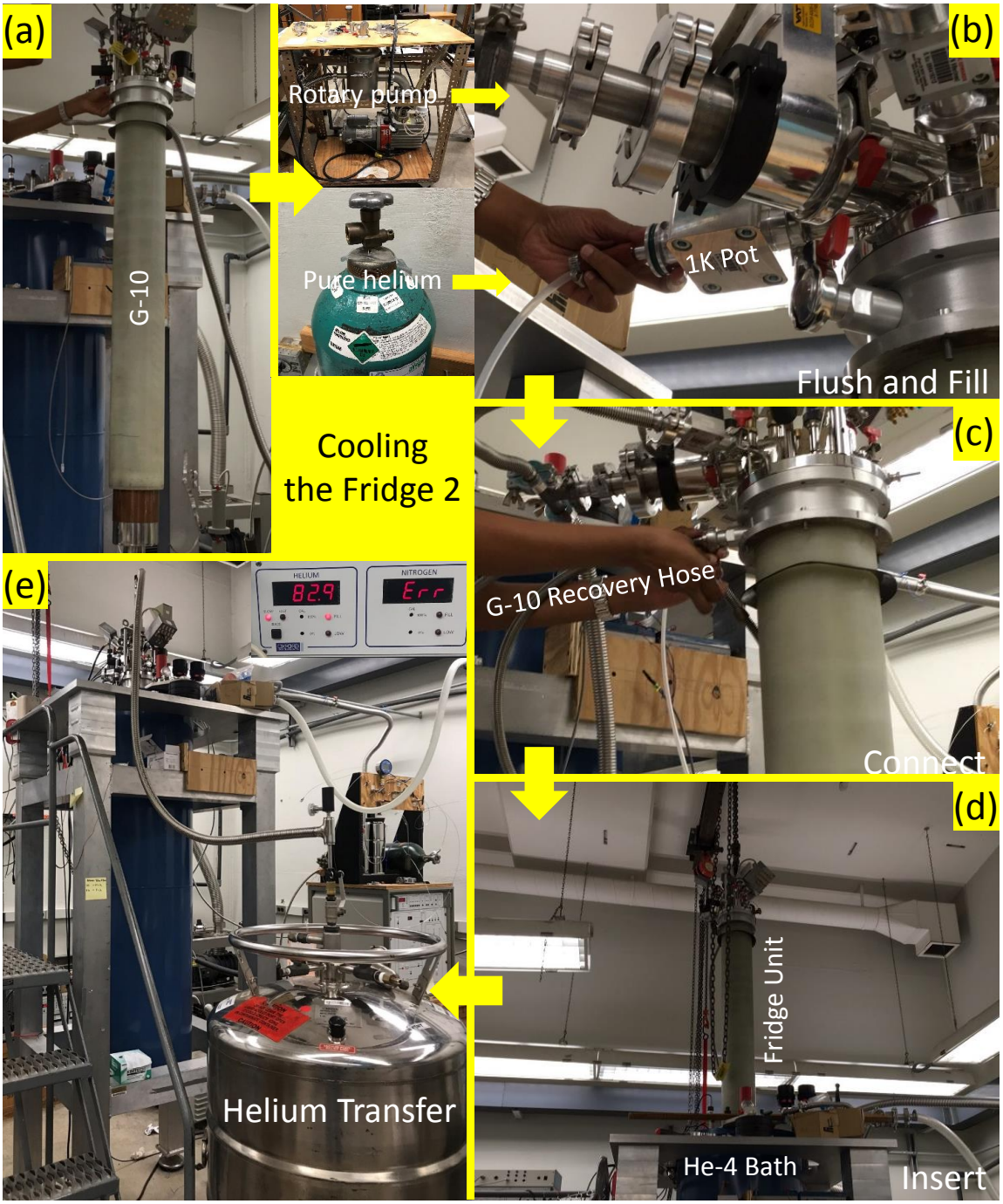

Figure 3.10. (a) G-10 shield on. (b) 1K Pot preparation: flush/fill the ultra-pure helium gas/flush. (c) Connecting the G-10 recovery hose. (d) Fridge unit insertion to ^{4}He bath. (e) Helium transfer is necessary soon after inserting the fridge unit.

system, since the heat capacity of liquid nitrogen is significant. 9) Once the liquid helium transfer is over, connect the pumping lines for the still, condenser, and 1K pot. 10) Check out the pressure in the line in front and behind the nitrogen trap which indicates the amount of impurities collected, record it, and pump them out with ^{4}He-rotary pump. 11) Insert the helium trap into the ^{4}He bath 12) Pump out the still line with the rotary pump and then with the turbo pump until the pressure reaches below 9×10^{-4}mbar. It takes more than 3 hours. 13) Start condensing.

Condensing & Circulating

Once the cooling the fridge process is done, the mixing chamber temperature is stabilized around 7K. To lower the temperature further, the gas mixture in the dump needs to be transported into the dilution unit and condensed into liquid. To transport the gas mixture into the dilution unit, we slowly diffuse the gas from the dump to condenser or still without using a pump. Although the fridge manual recommends the diffusion process through the condenser, our lab diffuses the mixture through the still. As the gas mixture diffuses into the still, from the cooling power of the 1K pot, it condenses into liquid inside the still and drips down to the mixing chamber. Since the 1K pot is thermally linked to the warm incoming gas mixture, 1K pot temperature can increase and run out all the liquid helium inside, if too much gas comes in abruptly. Therefore, we keep eyes on the 1K pot temperature maintaining it below 1.8K while increasing the amount of incoming gas mixture by opening the valve 12A. Once the pressure inside the dump and still reaches equilibrium, close the connection between the dump and still. At this point, condensing is done and the mixing chamber temperature stabilizes at around 1.5K. The process of transporting the gas mixture from the dump to dilution unit and condensing into liquid is called condensing and the condensing process takes approximately 4 hours.

To lower the mixing chamber temperature below the 1K pot temperature, the ^{3}He in the mixture needs to circulate. To circulate the ^{3}He, the ^{3}He-rotary pump sealed

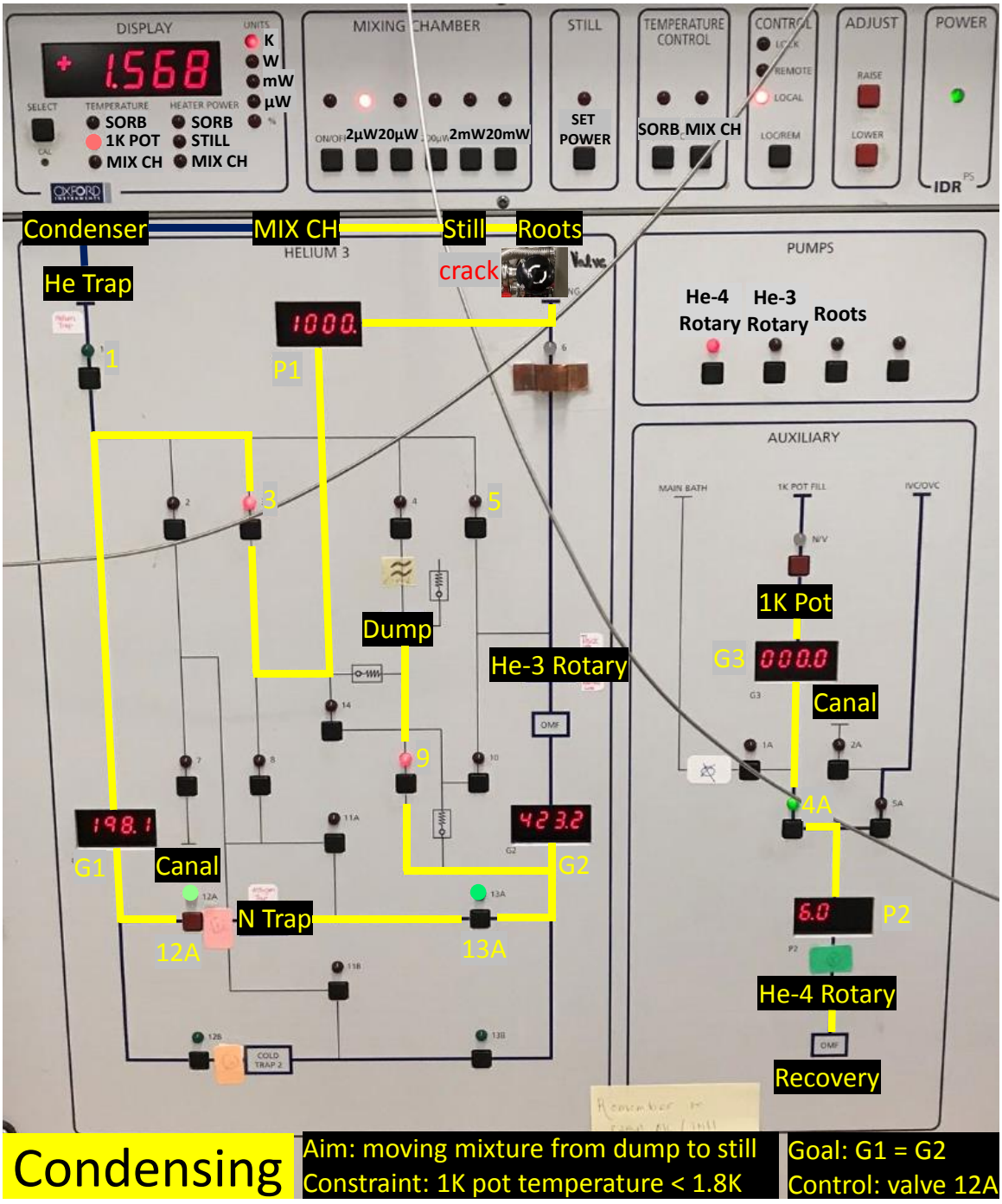

Figure 3.11. Condensing process of the mixture.

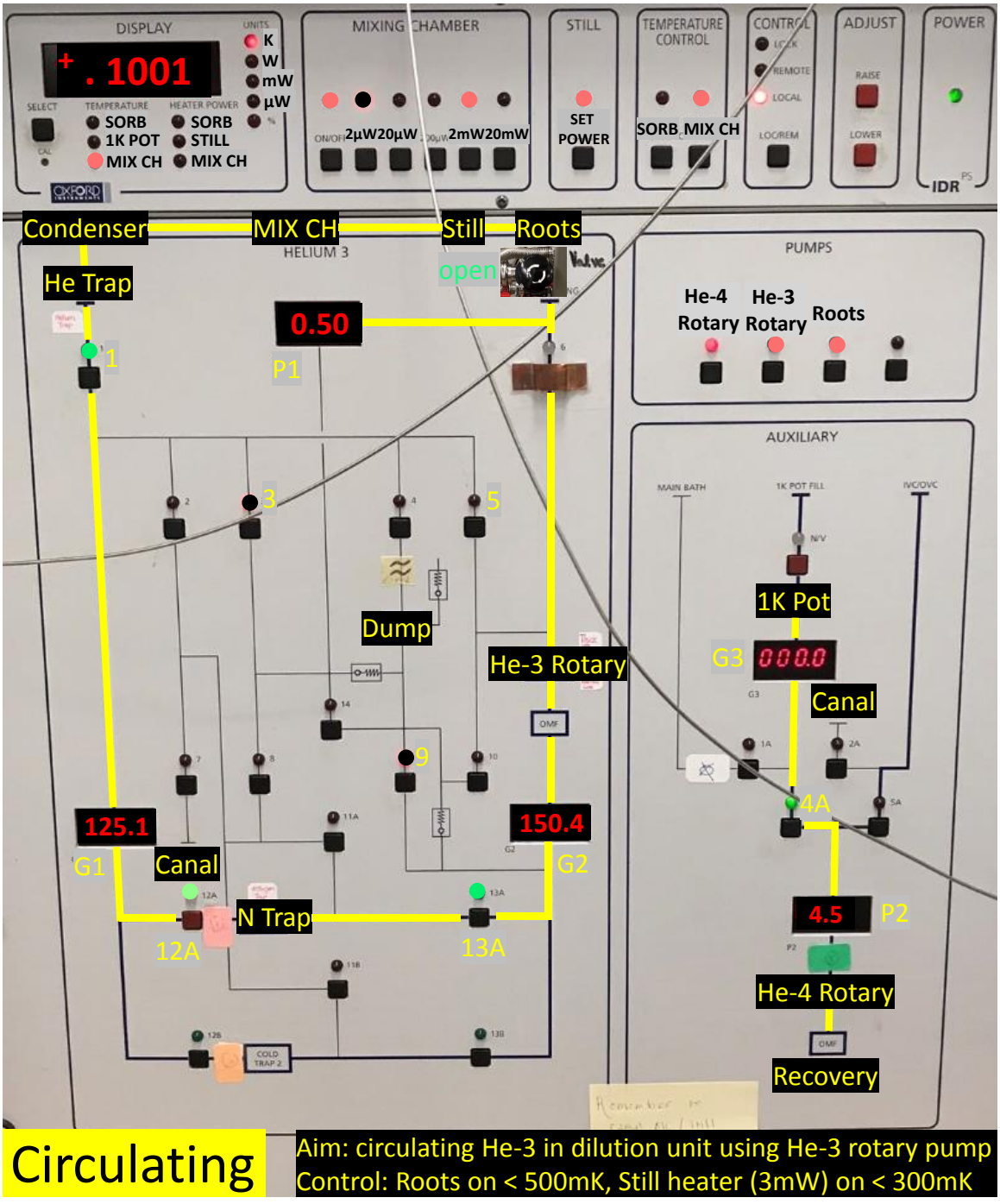

Figure 3.12. Circulating process of the mixture.

in a closed path is used primarily. Once the circulation starts, the mixing chamber temperature drops relatively quickly down to 500 mK. However, as the temperature drops further, the cooling speed becomes slower and the extra boosting of circulation is necessary. To boost the circulation of ^{3}He, from 500 mK, the roots pump locating in the middle of the still line between the still and the ^{3}He-rotary pump is turned on. From 300 mK, the heater on the still is turned on typically with 3 mW of heating power. The heater on the still boosts the evaporation of ^{3}He from the dilute phase inside the still. However, down to 100 mK, the temperature drops relatively fast only with the roots pump without the still heater. In addition, without operating the roots pump and the still heater, the temperature of mixing chamber can drop below 100 mK but very slowly. To sum up, this circulation process of ^{3}He is called circulating and controlled by ^{3}He-rotary pump, roots pump, and the still heater.

To start a measurement, the temperature of mixing chamber must be stabilized. This stability is achieved by the equilibrium between the cooling power of the dilution process and the heating power from the heater near the mixing chamber. Once a new temperature is set by a code, about 40-60 minutes take to stabilize the target temperature with properly operating roots pump and still heater.

Warming the Fridge

Warming the fridge process is divided into following steps: retrieving the mixture to dump, pulling out the fridge unit from the fridge dewar, and retrieving the sample. Although the warming up process is rather straight forward compared to the cooling and condensing & circulating process, equal amount of care is required since a small mistake during the process can ruin the system.

The most important part in the warming the fridge process is fully retrieving the mixture to dump. To retrieve the mixture, we follow these steps. 1) Turn off the still heat and stop the roots pump. 2) Close the needle valve. 3) Close the 13A, the valve connecting the dump and nitrogen trap. 4) Open the 9, the valve connecting

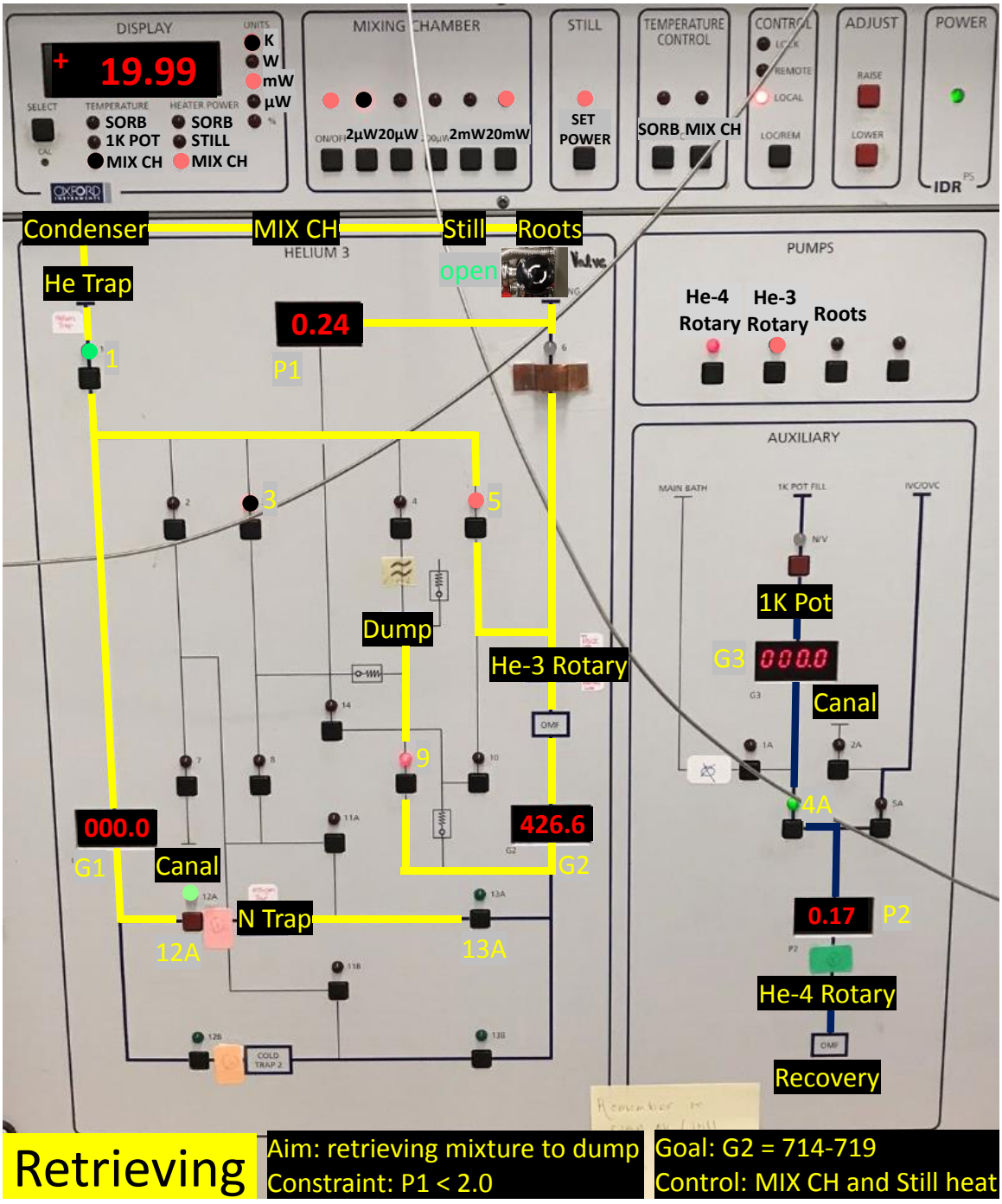

Figure 3.13. Retrieving process of the mixture.

the ^{3}He-rotary pump and dump; and open the 5, the valve connecting condenser and ^{3}He-rotary pump. 5) Start applying and increasing the heat on the mixing chamber and still while keeping the P1, the pressure coming into ^{3}He-rotary pump, less than 2. Preferably, it should maintain in between 1 and 2 mbar. P1 should not exceed 2 mbar all the time to prevent breaking the ^{3}He-rotary pump from inhaling too much gas. Once the G2, the pressure in the dump, exceeds 220 mbar, increase the mixing chamber heat to 20 mW which is the maximum and apply 20 mW to still. Once the 1K pot temperature exceeds 6K, turn off the still heat. 6) If there is an external heater, put 16 mW of external heat on the mixing chamber. If P1 is still lower than 2 mbar and the mixture is not retrieved fully, apply 100 mW of external heat. If an external heater is not prepared, it is still ok. Just wait enough time to retrieve all the mixture. 7) The G2, the pressure in dump, indicates the amount of mixture retrieved. 714-719 mbar is the maximum dump pressure with full mixture. The maximum pressure is room temperature dependent, thus it changes by seasons and whether AC operates or not. Once the G2 saturates to the maximum values, wait 3 hours more and close the 9, the valve sealing the dump, and record the G2 pressure. 8) Close the condenser valve and the gate valve for still. 9) Close all the dilution unit related electronic valves: 12A (nitrogen trap to panel), 1 (condenser to panel), 5 (condenser to ^{3}He-rotary pump), and the manual valves: pink (nitrogen trap to panel), black (still line to ^{3}He-rotary pump) on the panel. Do not turn off or close the 1K pot pump and valves. 10) Turn off the ^{3}He-rotary pump. 11) Lower the mixing chamber and still power to minimum and turn off the power. This procedure is important to prevent heating the mixing chamber and still accidentally with excessive heat set at this moment in the experiment. 12) Turn off the external heater. 13) Take the helium trap out from the ^{4}He bath; warm up the helium trap with a heat gun to touchable warm; open the valve 1 and measure the G1 pressure (pressure inside the helium trap) which indicates amount of impurities absorbed in the helium trap; close the valve 1. 14) Close the 1K pot valve on the fridge unit; close the 4A and green valves, the valves connecting 1K pot and ^{4}He-rotary pump. 15) Close the red valve on the recovery line

connected to ^{4}He-rotary pump and disconnect the hose from the pump. 16) From now, we will disconnect every connection to the fridge unit to pull the fridge unit out from the fridge dewar. 17) Vent the still line. 18) Close and disconnect the G-10 hose from the fridge unit and recovery line, if connected. 19) Ground the sample and thermometer using the box on the fridge unit; disconnect the ground cable, sample cable, thermometer cable, IGH box cable, 1K pot line, condenser line, still line (thick hose). 20) Connect the fridge unit to the hook from the ceiling and screw out the screws on the fridge unit. 21) Pull up the fridge 1/3 and wait for 20 minutes; pull up to 2/3 wait for 20 minutes; pull up almost all the way and wait for 20 minutes; take the fridge unit out from the fridge dewar and hang it on for a day. 22) To retrieve the sample, never forget to vent the IVC, before opening the IVC.

3.4 ^{3}He Immersion Cell

Instead of using a regular copper tail which is attached on the plate right below the mixing chamber, we use ^{3}He immersion cell to effectively stabilize the electron temperature in the sample. Since the development of RIQHSs is extremely sensitive to temperature change, delicate and stable temperature control is required to capture the temperature dependent behaviors of RIQHSs, especially around the onset of RIQHSs. By immersing the sample directly in the liquid ^{3}He using the immersion cell, this can be achieved.

The ^{3}He immersion cell is a chamber which seals the ^{3}He while the sample inside is touching the ^{3}He directly [118]. The chamber is made of half-transparent polycarbonate. With a polycarbonate cap having thread, the sample mount space where the liquid ^{3}He fills is sealed from the outside. Inside the immersion cell, the sample is soldered to silver sintered silver wires and mounted on a copper pillar which is in thermal contact with the wires. Here, the silver sinters are applied on wires to increase the surface of the wires touching the liquid ^{3}He to boost the thermalization between the wires and the ^{3}He. Once the electron temperature is controlled to

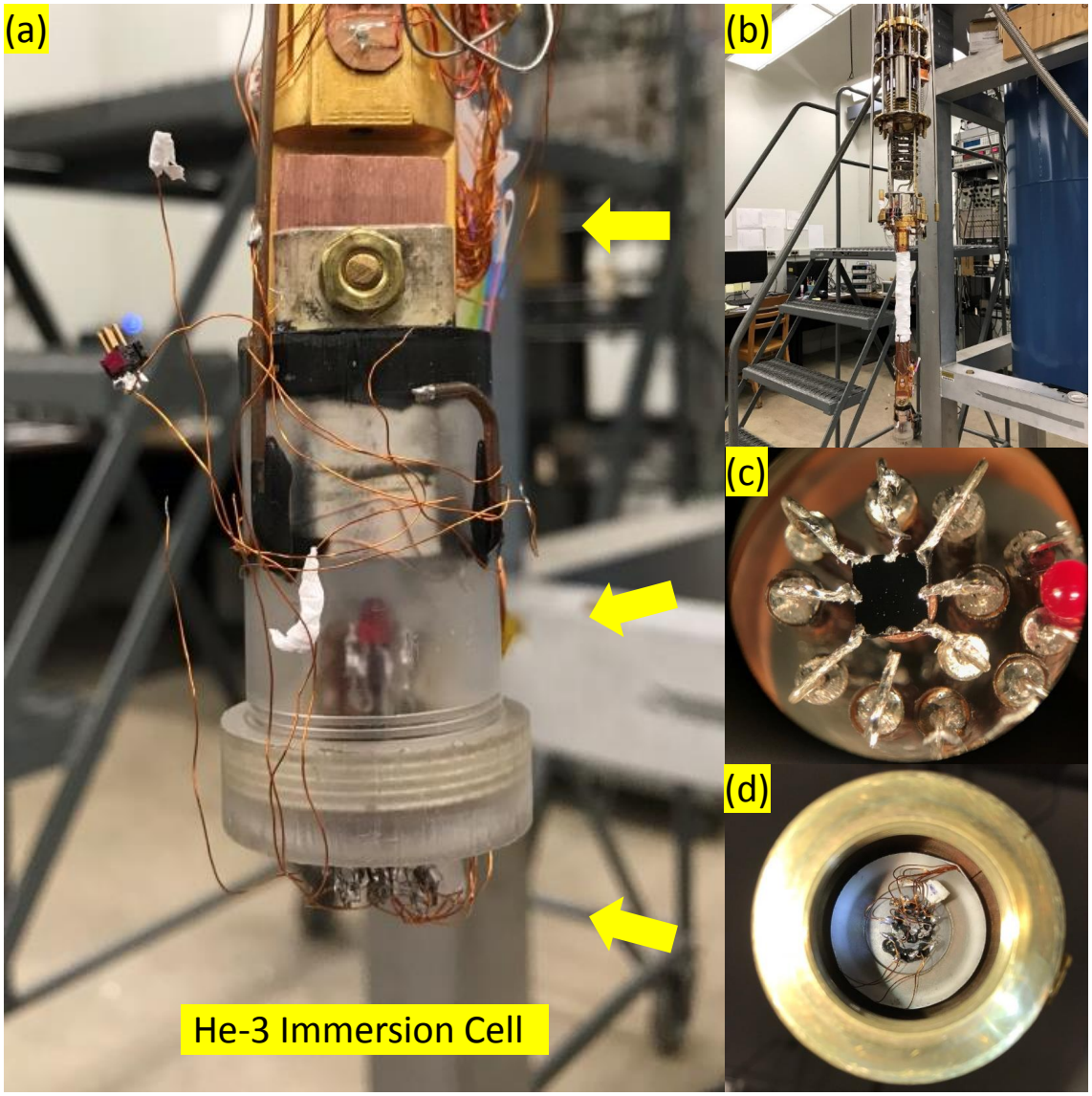

Figure 3.14. The ^{3}He immersion cell used in our experiments. (a) The exterior of immersion cell. The immersion cell is attached at the end of the immersion cell copper tail. (b) The immersion cell and its tail are attached below the mixing chamber plate. (c) The interior of immersion cell. A sample is mounted on the copper pillar at the middle of the cell. The contacts are made directly through the silver sintered silver wires without extra wires connecting in between. (d) The bottom sight of the immersion cell after closing the shield. The sintered silver wires are connected to the copper wires outside the cell.

the target temperature, thanks to the large heat capacity of liquid ^{3}He, the electron temperature can stably maintain.

To determine the sample temperature, we use an interesting technique [118]. By using the quartz tuning fork attached inside the immersion cell, we can measure the temperature of liquid ^{3}He directly from its viscosity. Since the liquid ^{3}He is directly touching the sample, referring the sample temperature to the liquid ^{3}He temperature is more accurate than referring to the temperatures measured by the thermometers attached on the mixing chamber plate. The viscosity of liquid ^{3}He is high enough to be measured at low temperature and sensitively changes depending on the temperature. Hence, by measuring the viscosity of the liquid ^{3}He from the resonance frequency of the tuning fork, the sample temperature can be determined. This non-resistance based thermometry has also other advantages on the measurement accuracy. It is immune from the self-heating and high magnetic field effect which reduce the accuracy of resistance-based thermometry.

3.5 Low Noise Measurement

In order to detect the most sensitive signals from an electronic state, signal to noise ratio ought to be maximized. To achieve this, we perform our experiments with measurement system of *lock-in amplifier* often times preceded with *pre-amplifier* to amplify the incoming signal further. To examine the signal to noise ratio of a circuit, *spectrum analyzer* is used to measure the signals coming from the cables which will be eventually connected to the inputs of lock-in amplifier. To reduce background noise such as the 60 Hz noise, we attach several *ferrites* on the sample cable bundle or any cables connected on the circuit.

3.5.1 Lock-in Amplifier

Lock-in amplifier is an amplifier which can measure the signal from only the designated frequency. By measuring the signal from the single designated frequency, lock-in amplifier removes the noise from different frequencies.

In our experiment, we use lock-in amplifiers as both current source and measurement device. We normally attach a 1GΩ or 100MΩ resistor (at least 100 times larger than the sample resistance) at the output of lock-in amplifier to make it as a current source. We typically use 1 nA not to heat up the sample; however, when the signal to noise ratio is too small and as a result the graph looks too noisy, we increase the current to 10 nA or up to a current which will not heat up the sample. Once the circuit is set up, we measure the voltage on the sample down to orders of nano-volt using the coax cables which are connected on the inputs of the lock-in amplifier. To avoid the 60Hz noise from the U.S. commercial frequency, we avoid using the frequency which are the multiples of 60 Hz. Typically, we use frequency between 4 Hz and 20 Hz.

4. OBSERVATION OF MULTIPLE REENTRANCE IN A HIGH LANDAU LEVEL AND THE STRUCTURE OF THE ORBITAL WAVEFUNCTION

Stripe and bubble patterns form in various natural systems spontaneously when the competition between long-range and short-range interactions break uniformity. Stripe or nematic morphology are under intense investigation in numerous strongly correlated electron systems. In contrast, the bubble morphology in electronic system is rare. Some of the most fascinating bubbles develop in the two-dimensional electron gas under perpendicular magnetic field. However, unlike the bubbles forming in classical systems including the Langmuir films and Turing activator-inhibitor reaction, bubbles of electron gases emerge from quantum mechanical interactions: they are stabilized while the individual electronic wavefunctions overlap. Here, we report a proliferation of multi-electron bubble phases in a high Landau level and conclude the richness is from the increasing nodal structures of the electronic wavefunction.

In this project, we measure the magnetotransport of the RIQHSs in high Landau levels of 2DEG in ultra-pure GaAs/AlGaAs. Consistent with earlier results, we observe four RIQHSs in the $N = 2$ Landau level which were associated with single type of bubble phase based on symmetry considerations. In contrast, in the $N = 3$ Landau level, we find eight distinct RIQHSs which indicates the family of RIQHSs is richer than previous reports. This proliferation of the RIQHSs in a higher Landau level was a missing puzzle of the bubble interpretation of the RIQHSs. Therefore, our result significantly strengthens the bubble interpretation of the RIQHSs and identifies the types of bubbles phases in the $N = 2$ and 3 Landau levels. Furthermore, we find evidence of which the wavefunction structure of electrons determines the richness of multi-electron bubble phases in high Landau levels highlighting a fundamental difference between quantum and classical bubbles.

Our measurement was supported by the NSF grant DMR 1505866. The sample growth work of M.J. Manfra was supported by the DOE BES award DE-SC0006671, and that of K.W. West and L.N. Pfeiffer by the NSF MRSEC Grant No. DMR-1420541 and the Gordon and Betty Moore Foundation Grant No. GBMF 4420.

Additional Note. Observations from this chapter were reported at APS March Meeting 2019 [98] earlier than the related observations in alloy disorder sample were published by Fu *et al.* [84]. Later, our work in this chapter was published in Ref. [117].

4.1 Background: The Discrepancy between the Bubble Theories and Experiments

The complex charge order of non-relativistic electrons in the topmost Landau level of two-dimensional electron gas (2DEG) is predicted by the pioneering Hartree-Fock theory [61–63]. The intriguing charge order emerges in bubble and stripe phases at Landau level filling factors ν away and at from half integers, respectively. Bubble phases are intricate solids of electrons. In the no disorder limit, several electrons cluster into a unit called bubble and the bubbles arrange in a triangular lattice structure forming a bubble crystal. The lattice constant of bubble crystal is approximately three cyclotron radii [61, 62]. The Hartree-Fock theory is understood to be exact for Landau levels with large orbital index $N \gg 1$ [63] and regarded to hold for $N \geq 2$ [61–63]. Since fluctuations are not considered in the mean-field level approach of Hartree-Fock theory, the bubble formation is expected to be interrupted in the $N = 1$ Landau level [61–63]. Density matrix renormalization group (DMRG) [65] and exact diagonalization [64] studies also provide additional theoretical support for the emergence of bubble phases.

Soon after the prediction of the Hartree-Fock theory, the complex charge order was observed in the $N = 2$ and higher Landau levels of in 2DEGs confined in GaAs/AlGaAs [66–69]. Reentrant integer quantum Hall states (RIQHSs) were associated with bubble phases whereas anisotropic phases at half-filling were asso-

ciated with stripe phases [66–69]. Later experiments of pinning resonance [71, 72], Non-linear transport [68, 70], surface acoustic wave measurements [74, 75], and onset temperature [73] in RIQHSs also supported the bubble interpretation.

Although the experimental results on the RIQHSs are consistent with the bubble interpretation, they are certainly not conclusive. This is because the 2DEG is underlying deep in the GaAs crystal and inaccessible to scanning probes, on one hand. And the proliferation of RIQHSs in higher Landau levels, a hallmark of the bubble theory, has not been observed, on the other hand. The Hartree-Fock theory predicts an increasing number of bubble phases with increasing Landau level index N at $N \geq 2$ [65, 76–81]. DMRG calculations also reached to similar conclusion comparing $N = 2$ and $N = 3$ [65, 78]. However, so far in experiments including microwave pinning resonance [71, 72], transport [66, 67, 75, 82–84], and surface acoustic wave attenuation measurements [75, 83], the same number of RIQHSs was found in the $N = 2$ and higher Landau levels. Even if single RIQHS associates with multiple bubble phases, such an assumption could not be examined in the lack of direct scanning of the morphology. The absence of the proliferation of RIQHSs at large Landau indices is specifically unsettling since the Hartree-Fock theory is known to provide better description as N increases [63].

4.2 Observation of M=2 and M=3 Reentrant Integer Quantum Hall States in the N=3 Landau Level

In Fig 4.1, we present magnetotransport traces of the $N = 2$ and higher Landau levels. R_{xy} is the Hall resistance whereas R_{xx} and R_{yy} are the longitudinal resistances measured along mutually perpendicular crystal directions of GaAs. We measured a sample of density $n = 2.8 \times 10^{11}\text{cm}^{-2}$ and mobility $15 \times 10^{6}\text{cm}^{2}/\text{Vs}$. More details on this sample and the measurement setup are described in Ref. [73]. The quantization of Hall resistance to $R_{xy} = h/ie^2$ and vanishing longitudinal resistances $R_{xx} = R_{yy} = 0$ at integer filling factors $\nu = i$, with $i = 4, 5, 6, ...$, are the signs of integer quantum

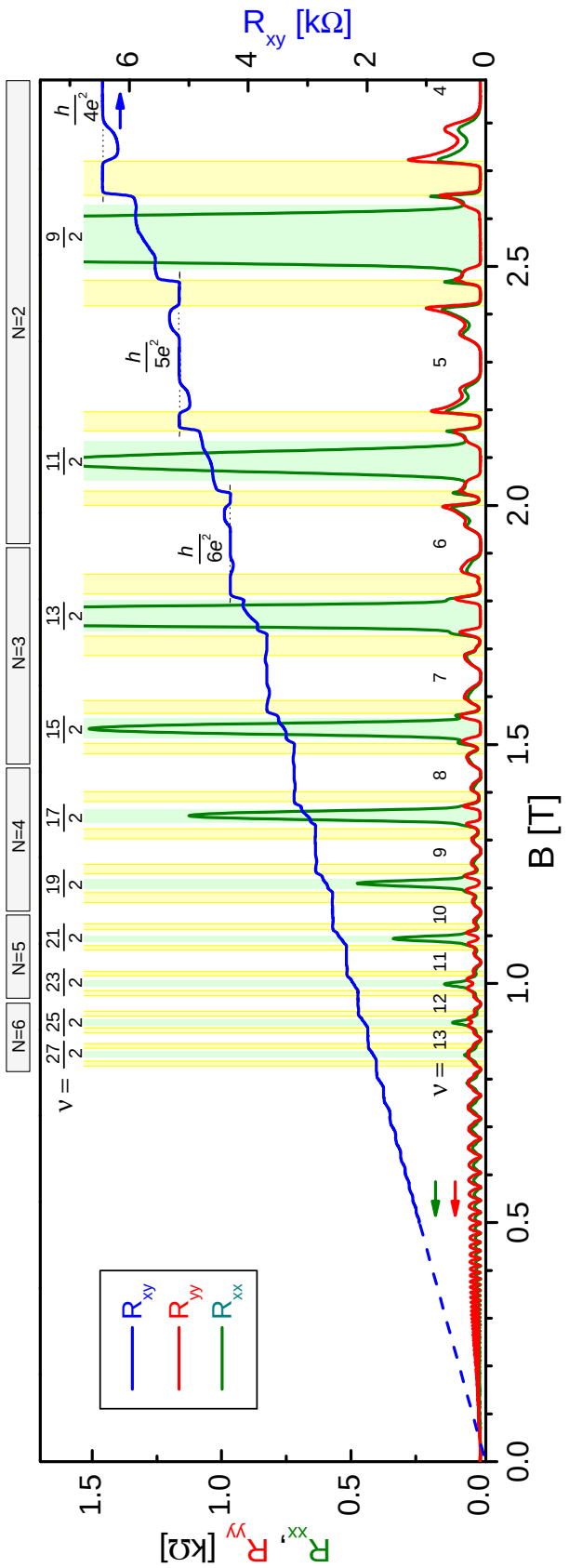

Figure 4.1. Hall resistance R_{xy} and longitudinal resistances R_{xx}, R_{yy} measured along two perpendicular crystal directions are plotted with respect to the magnetic field B for the $N = 2$ ($4 < \nu < 6$), $N = 3$ ($6 < \nu < 8$), and higher Landau levels. Here, ν is the filling factor and N is the Landau level index. Data were measured at $T = 77$ mK. Numbers are marked at the integer and half-integer filling factors. RIQHSs which associate with bubble phases are colored in yellow whereas the nematic phases are colored in green. Reprinted figure with permission from Ref. [117].

Hall states (IQHS) [85]. The remarkably strong resistance anisotropies at half-fillings $\nu = 9/2, 11/2, ..., 27/2$ indicate the quantum Hall nematic phases [66,67] associated to the stripe phases of the Hartree-Fock theory [61–63, 86–88]. Presence of the nematic phases in Landau levels as high as $N = 6$ is a fingerprint of ultra purity of sample.

Based on previous work, transport feature near $\nu = 4$ may be understood as below. At $\nu = 4$, occurring at $B = 2.90$ T in our sample, the $N = 0$ and $N = 1$ Landau levels are full while the $N = 2$ Landau level is empty. By reducing B, the $N = 2$ Landau level populates and therefore the areal density of electron quasiparticles in the topmost Landau level n^* increases. At low n^*, the electron quasiparticles are localized by disorder, hence an integer plateau $R_{xy} = h/4e^2$ and $R_{xx} = 0$ develop in Fig 4.1 between $B = 2.8$ T and $B = 2.90$ T. As n^* increases, the Coulomb interactions of the electrons overcome disorder effects, leading a transition to a Wigner solid [89]. The Wigner solid is not able to be distinguished by standard transport, but its signatures were captured in compressibility [91], microwave resonance [89, 90], tunneling measurements [94], and resistively detected NMR [92,93]. A further increase in n^* induces the reentrance to the integer quantization: first a deviation from integer quantization occurs, then a conspicuous return to quantization is realized [66–68]. Such behaviors appear in the regions near $B = 2.44$ and 2.68 T and other regions colored in yellow in Fig 4.1. Because the reentrance is not expected from an Anderson insulator, the reentrance signals a collective nature such as the electron bubble phase [67, 68].

Consistent with previous results, in the $N = 2$ Landau level, we observe four RIQHSs locating at $\nu = 4 + 0.29$, $5 - 0.29$, $5 + 0.29$, and $6 - 0.29$ [67, 68, 73]. These are shown in Fig 4.1. These four filling factors are in particle-hole symmetry relation, thus the four RIQHSs are associated with single type of bubble phase. Calculations found the $M = 2$ bubble phase at these filling factors [61, 62, 64, 65, 78–81].

Surprisingly, the magnetoresistance in the range of reentrance around $B = 1.83$ T or $\nu = 6.3$ in Fig 4.1 appears wider than expected and reveals an uncommon structure in the $N = 3$ Landau level. We further examine the details of the structure more

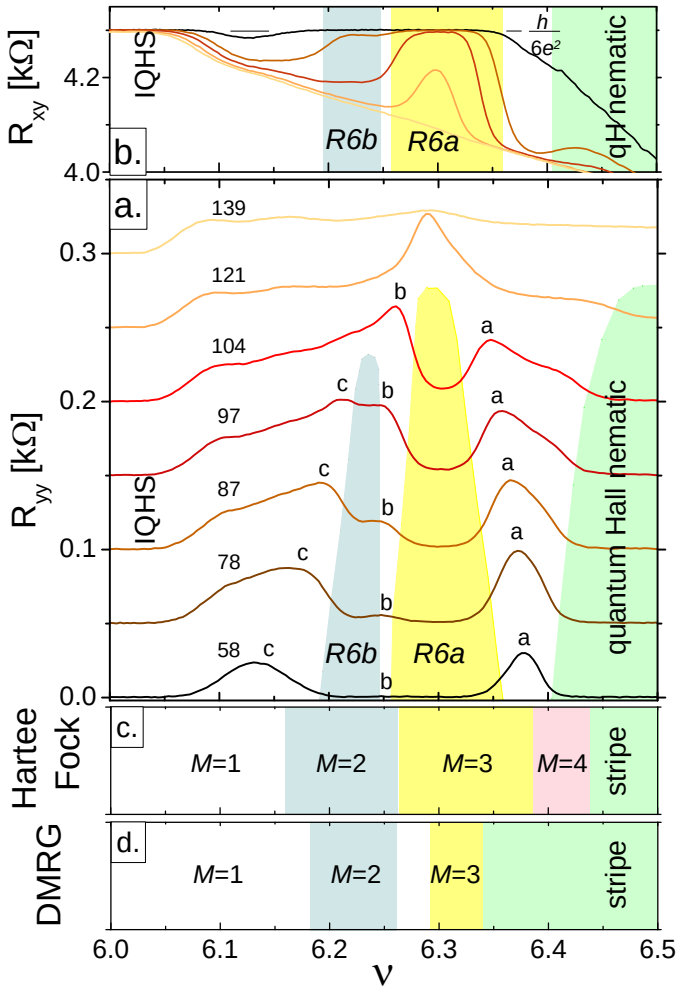

Figure 4.2. Panel *a*: Temperature evolution of the longitudinal resistance R_{yy} in the filling factor range $(6 < \nu < 6.5)$ of the $N = 3$ LL is plotted in waterfall style. Traces in consecutive temperatures are shifted by 50 Ω. The local maximum labeled *b* distinguishes the two distinct RIQHSs marked *R6a* and *R6b* which are colored in yellow and blue respectively. Panel *b*: The waterfall style plot for the Hall resistance in the reentrance region. The $T = 78$ and 97 mK traces were dropped out to reduce clutter. Traces at $T = 78$ and 97 mK were omitted to reduce clutter. Panels *c* and *d*: The ground state phase diagrams of the $N = 3$ Landau level predicted by Hartree-Fock theory [78–80] and DMRG calculations [78]. Two-, three-, four-electron bubble phases are colored in blue, yellow, and pink respectively. Reprinted figure with permission from Ref. [117]. Copyright © 2019 by American Physical Society.

closely. In Fig 4.2, the $T = 104$ mK traces exhibit a quantized Hall resistance $R_{xy} = h/6e^2$ and a vanishing magnetoresistance R_{yy} at $\nu = 6.30$ indicating the development of the $R6a$ labeled RIQHS. In the yellow colored region in Fig 4.2a, a local minimum in the magnetoresistance is observed between the two local maxima labeled a and b. However, as the temperature is lowered to $T = 97$ mK, another local minimum appears at $\nu = 6.23$. This second minimum appears in the blue colored region between the two local maxima named b and c in Fig 4.2a. With further temperature drop to $T = 58$ mK, R_{yy} at the second minimum vanishes and the Hall resistance becomes quantized to $R_{xy} = h/6e^2$. This data unveils a novel RIQHS at $\nu = 6.23$, which we labeled $R6b$ in Fig 4.2a. Owing to the resistive feature b, the novel RIQHS is distinct from $R6a$. Hence, we observed a dual reentrance of the $\nu = 6$ IQHS at the filling factor range of $6 < \nu < 6.5$ in the $N = 3$ Landau level. We encounter two distinguishing RIQHSs instead of single RIQHS in the region. Therefore, the number of RIQHSs proliferates in the $N = 3$ Landau level compare to that in the $N = 2$ Landau level. Such proliferation of the RIQHSs is readily interpreted as the proliferation of two distinct multi-electron bubble phases, a hallmark for the validity of bubble interpretation. Our finding provides the first evidence of the proliferation of multi-electron bubble phases in a high Landau level and strongly enhance the validity of the bubble interpretation of the RIQHSs.

Our data show additional details that strengthen the bubble interpretation of RIQHSs further. First, the Hartree-Fock [76–81] and of DMRG calculations [65, 78] predict that the multiple bubble phases appearing in a Landau level must be close in energy. Our data shows the RIQHSs $R6a$ and $R6b$ follow the case in Fig 4.2. The two onset temperatures are estimated within 15% of each other. Second, the doubled reentrance is an orbital effect in consistent with the Hartree-Fock theory. Data in Fig 4.3b indeed show the doubling of the reentrance behavior in both spin branches of the $N = 3$ Landau level. This implies the physics is independent from spin quantum number and thus the RIQHSs we observe in the N=3 Landau level including the

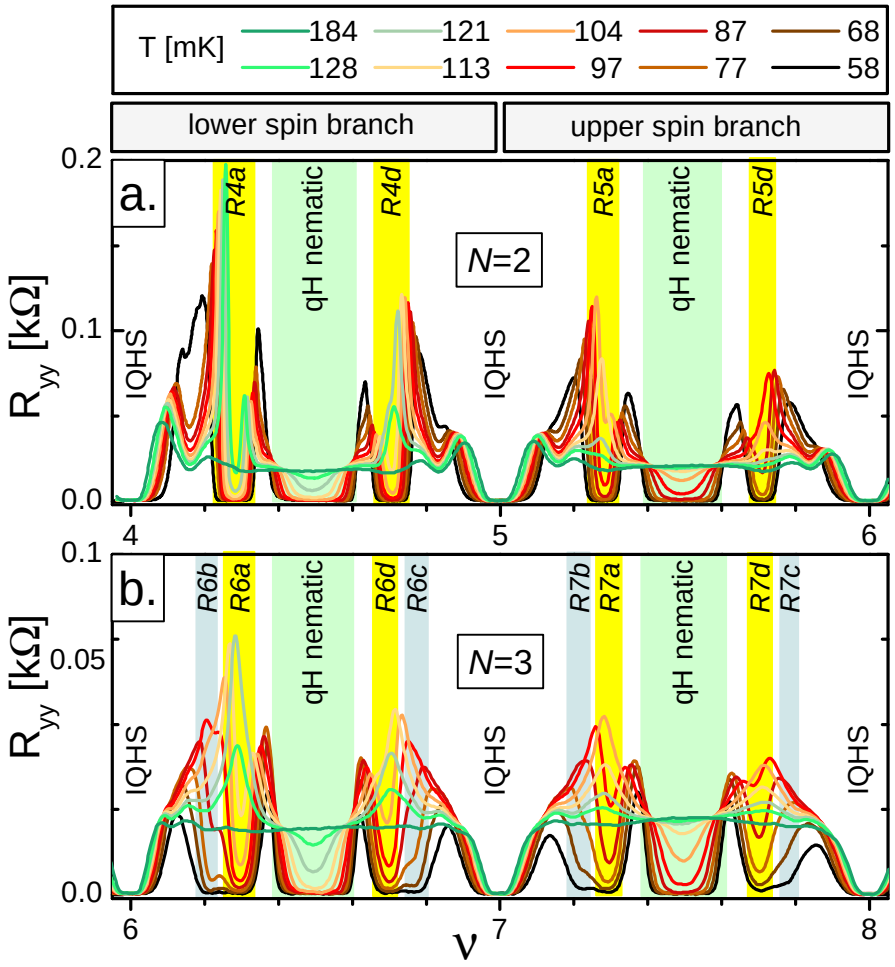

Figure 4.3. Temperature evolution of the longitudinal resistance in the $N = 2$ (panel a.) and $N = 3$ (panel b.) Landau levels. The measured temperatures and the spin branches are shown in the top legends. RIQHSs are colored in yellow and blue; stripe phases are colored in green, and the IQHSs are uncolored. The distinct resistive feature at several low temperatures distinguishes the two different types of RIQHSs in the $N = 3$ Landau level. Reprinted figure with permission from Ref. [117]. Copyright © 2019 by American Physical Society.

newly found *R*6*b*, *R*6*c*, *R*7*b*, and *R*7*c* precipitate due to orbital effects. The filling factors of the groups of RIQHSs are in particle-hole symmetry.

We are able to assign bubble phases to the RIQHSs based on the results of the Hartree-Fock and DMRG calculations. Fig 4.2c and Fig 4.2d presents the predicted

ground states in the $N = 3$ Landau level of the Hartree-Fock [78–80] and DMRG [78] calculations, respectively. The alignment of filling factor ranges of our RIQHSs are in excellent agreement with those of the $M = 2$ and $M = 3$ bubble phases. Furthermore, the range of $M = 1$ bubble phase or the Wigner solid overlaps with the measured $\nu = 6$ integer quantum Hall plateau, although it is considerably wider. We conclude the $R6a$ RIQHS emerging around $\nu = 6.30$ is a bubble phase with 3 electrons per bubble, while the weaker $R6b$ emerging around $\nu = 6.23$ is a bubble phase with 2 electrons per bubble. We find no evidence for the $M = 4$ bubble phase of the Hartree-Fock theory [78–80]. We observe the quantum Hall nematic phase at the expected filling factors instead. DMRG calculations more accurately capture the transition between the $M = 3$ bubble phase and the nematic phase. In the same manner, the RIQHSs in the $N = 2$ Landau level presented in Fig 4.3a are associated with $M = 2$ bubble phases.

Data in Fig 4.2a present that the onset temperature of $R6a$ exceeds that of $R6b$. These energy scales would favorably compare to the cohesive energies of the $M = 2$ and $M = 3$ bubble phases in the Hartree-Fock calculations. Our data agree with the results in Refs. [79, 81] qualitatively which predict the $M = 3$ bubbles closer to half filling are more stable. However, our data are not consistent with the results in Refs. [76, 80]. The contradicting results of calculated cohesive energy is not from different dielectric functions used: Refs. [76,81] include screening using a wavenumber-dependent dielectric function while Refs. [79, 80] through a constant dielectric function. However, the Ref. [81] find the finite thickness effect of the electron layer has a remarkable influence on cohesive energies. These results imply the finite thickness or other effects modifying the short-range part of the Coulomb interaction can give a strong impact on cohesive energies. Nevertheless, the contradiction on the calculated cohesive energy, do not dim the observation of two RIQHSs in the $N = 3$ and the interpretation of these RIQHSs as multi-electron bubble phases.

4.3 The Origin of Multiple Bubble Formation in High Landau Levels: Nodes of Orbital Wavefunctions

One finds competition between long-range and short-range interactions in the origin of bubbles. For the bubble phases, the Coulomb interaction maintains its bare form in the long-range, while it is modified by the overlap of wavefunctions

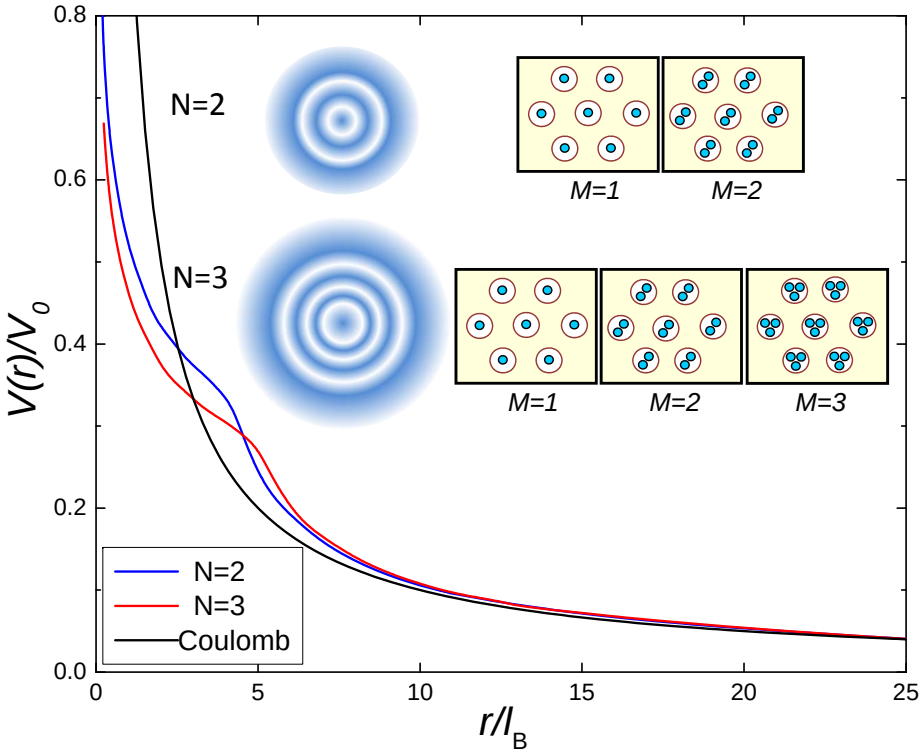

Figure 4.4. The interaction energy in units of Coulomb energy $V_0 = e^2/(4\pi\epsilon l_B)$ for the Landau indices $N = 2$ and $N = 3$. As the electronic wavefunctions overlap, the interaction energies deviate from the bare Coulomb expression. The inset associates the nodal structure of the wavefunction $|\psi|^2$ under the symmetric gauge with the types of emerging bubble phases. In the $N = 2$ Landau level, the wavefunction has two nodes and two different types of bubble phases ($M = 1$ and $M = 2$) exist. In contrast, in the $N = 3$ Landau level, the wavefunction has three nodes and three different types of bubble phases ($M = 1$, $M = 2$, and $M = 3$) exist. Reprinted figure with permission from Ref. [117]. Copyright © 2019 by American Physical Society.

ψ of the electrons [61–63] in the short-range. In Fig 4.4 we present the $|\psi|^2$ for $N = 2$ and $N = 3$ of the symmetric gauge. When their geometric centers are close, the overlap of the objects creates the bubbles. Since structure of the wavefunction is dependent on the Landau index, the Coulomb interaction in short-range also depends on the Landau index. Even though the shape of wavefunctions ψ depends on the choice of the gauge potential [95], observables are the result of gauge-independent property in wavefunctions. We suggest the gauge-independent property related to bubble formation is the number of nodes in the electronic wavefunctions. It was already discussed that nodal lines in the wavefunctions play a role in creating the bubbles [69]. Our discovery of multiple reentrance in the $N = 3$ Landau level brings the intriguing effects of multiple nodal lines to the fore in generating a rich set of multi-electron bubble phases. In Fig 4.4, the nodal lines are presented as white circles. Our results show the number of bubble phases in the $N = 2$ and $N = 3$ Landau levels coincides with the number of nodal lines in the wavefunctions, which is the same with the Landau index N, when the Wigner solids are included as the $M = 1$ electron bubble phases. In contrast, the quantum Hall nematic phases in our experiment did not show any particular dependence on the nodal structure of wavefunctions.

Our findings underline the fundamental differences between the quantum and classical bubbles. Examples for the classical bubbles are found in the Langmuir films or in the Turing activator-inhibitor system [96]. In classical systems only single type of bubble exist; the density change of the system often creates the size change of the bubbles. In contrast, in the quantum mechanical 2DEG, different types of bubbles are allowed to form; the quasiparticle density change results in either a phase transition or a crossover to different types of bubble phases.

The weak but distinctive resistive feature marked b in Fig 4.2a distinguishes the *R*6*a* and *R*6*b* RIQHSs. It is noteworthy that a sharp phase transition is expected between the two bubble phases in the Hartree-Fock theory [65, 76–81]. The resistive feature having finite width may be appeared owing to the presence of disorder in our sample, which is not counted in the theory. The resistive feature could also be the

result of a backscattering channel providing the percolating paths between coexisting two different bubble domains [77]. Interestingly, the resistive feature we observe has a very good overlap with the uncolored range between the $M = 2$ and $M = 3$ bubble phases where the ground state could not be identified in DMRG calculation [78].

The recent observations of RIQHSs in graphene provides the chance to study electron bubbles in a novel platform [97]. Results highlight the host-independent property of the physics and offer the opportunity to study new effects, such as the effect on the valley degree of freedom on the RIQHSs.

4.4 Conclusion

In conclusion, we observed the doubled reentrance of the integer quantum Hall effect in the $N = 3$ Landau level of a ultra-pure 2DEG confined to GaAs/AlGaAs. Our observation provides an evidence of the proliferation of the RIQHSs in high Landau levels, hence strongly support the bubble interpretation of the RIQHSs. Our result underlines the role of quantum mechanics in electronic bubble formation, particularly, the attribution of the three nodal lines of the electronic wavefunctions to the abundance of the bubble phases in the $N = 3$ Landau level.

5. STABILITY OF MULTI-ELECTRON BUBBLE PHASES IN HIGH LANDAU LEVELS

We investigate the multi-electron bubble phases in the $N = 2$ and $N = 3$ Landau levels in a ultra-pure GaAs/AlGaAs sample. We found the longitudinal resistance versus temperature curves exhibit sharp peaks in the multi-electron bubble regions irrespective of the Landau level index. We interrelate these peaks with an increased scattering occurred by thermally fluctuating domains of bubble phases and uncorrelated electron liquid at the onset temperatures of the bubble phases. We also found the onset temperatures of three-electron bubble phases are systematically higher than those of two-electron bubble phases within the $N = 3$ Landau level; and exhibit a different trend with respect to the filling factor, regardless of Landau levels. Furthermore, the two-electron bubble phases across $N = 2$ and $N = 3$ Landau levels have similar onset temperatures exhibiting an offset. Our measurements provide information on bubble energetics which is expected to be a guide for improving the existing theories and which reveals the impact of the short-range effective electron-electron interaction on bubble formation.

Our measurement was supported by the NSF grant DMR 1904497. The sample growth effort of M.J. Manfra was supported by the DOE BES award DE-SC0006671, and that of L.N. Pfeiffer and K.W. West by the NSF MRSEC Grant No. DMR-1420541 and the Gordon and Betty Moore Foundation Grant No. GBMF 4420.

Additional Note. Our work in this chapter was submitted as Ref. [120].

5.1 Background: Absence of Studies on the Number of Electrons per Bubble M

The two-dimensional electron gas (2DEG) under perpendicular magnetic fields is a system hosting rich physics that creates a variety of electronic phases. The most

well known of the phases are, perhaps, the fractional quantum Hall states [100] which carry topological order. Electron solids harboring charge order form another distinct group of phases. Electronic solids include the Wigner solids [101], electron bubble phases, and nematic or stripe phases [61–63, 66–69, 87, 102, 103].

Bubble phases are one of the most recently discovered states of 2DEGs which their properties have not been revealed all yet. They were predicted by a Hartree-Fock theory [61–63] first and further confirmed by the density matrix renormalization group (DMRG) [65] and exact diagonalization [64] studies to be a periodic array of clusters called electron bubbles. In linear transport, the reentrant integer quantum Hall states are identified as bubble phases [67,68,102]. In addition, non-linear transport [68,70,82, 83,105,106], microwave resonance [71,72,104], temperature dependence [73,107–111], surface acoustic wave [74, 75], and thermal transport measurements [112, 113] also support the formation of bubbles. However, direct detection of the bubble morphology is still absent.

Bubble phases are generally observed in 2DEGs in GaAs/AlGaAs [66–75, 82, 83, 102,104–113] and have also been found in graphene recently [97]. In the GaAs/AlGaAs system, bubbles appear in the Landau levels having orbital index $N \geq 1$. Theories predict different type bubble phases exist within a Landau level [76–81,114–116]. The types of bubble phases are differentiated by the number of electrons per bubble M and a modest tuning of filling factor was expected to lead a phase transition between two different types of bubbles. Experiments nearly for two decades could not resolve such distinguishing bubble phases. The distinct bubble phases were observed only recently in the $N = 3$ Landau level [99,117]. The filling factors range of these bubble phases excellently agree with the predictions. These observations assigned the corresponding bubble phases to the newly resolved two different types of reentrant integer quantum Hall states (RIQHSs) and cemented the bubble phase interpretation of the RIQHSs.

Recent resolution of two different multi-electron bubble phases within one Landau level [99, 117], the $N = 3$ Landau level, facilitated the qualitative and quantitative

study both within one Landau level and across different Landau levels. We found the bubble phases in the $N = 3$ Landau level of our high mobility GaAs/AlGaAs sample show sharp peak behavior in the longitudinal magnetoresistance versus temperature traces at fixed magnetic fields. The peak behaviors were captured previously in the $N = 1$ and $N = 2$ Landau levels in ultra-pure GaAs/AlGaAs [73, 110, 113] and also in graphene [97]. However, such peaks were absent in an alloy disorder GaAs sample having low mobility [99]. We think these peak behaviors are originated from scattering through the bulk of the sample caused by fluctuating and interpenetrating domains of bubbles and uncorrelated uniform liquid. Based on this interpretation, the onset temperature of bubble phase which provides the maximum of the peak is extracted. We found the onset temperatures of the bubble phases extracted with this method have a surprising dependence on the number of electrons per bubble. Within the $N = 3$ Landau level, the dimensionless reduced onset temperatures of $M = 3$ bubble phases are higher than those of $M = 2$ bubble phases and present different trends with respect to the filling factor. Moreover, comparing the $M = 2$ bubble phases across the $N = 2$ and $N = 3$ Landau levels, we found the dimensionless onset temperatures are close each other yet having an offset. Our measurements provide information on energetics of bubbles that facilitate a qualitative comparison to the theories; and on details of the effective electron-electron interaction in short-range.

5.2 The Signatures and Criticality of Electron Bubbles: The Peak Behaviors and Onset Temperatures

We measured a magnetotransport of 2DEG in GaAs/AlGaAs quantum well of 30 nm width having an electron density $n = 2.8 \times 10^{11}$ cm^{-2} and mobility $\mu = 15 \times 10^6$ cm^2/Vs. In the experiment, the sample was mounted on a He-3 immersion cell [118] to stabilize the sample temperature more effectively taking the advantage of the large heat capacity of liquid He-3.

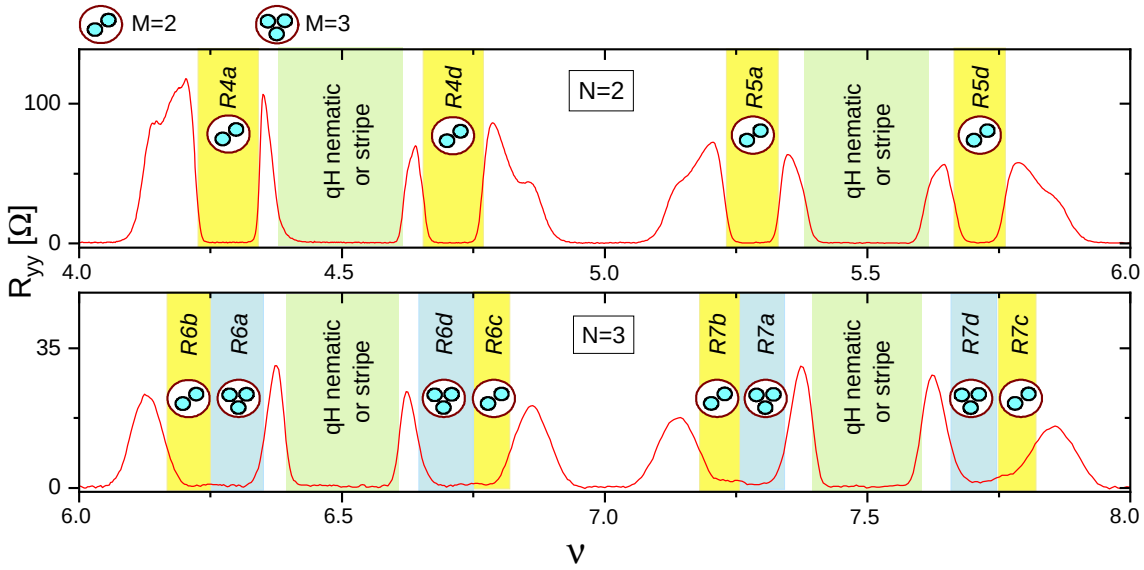

Figure 5.1. The longitudinal magnetoresistance R_{yy} is plotted with respect to the filling factor ν in the $N = 2$ (top panel) and $N = 3$ (bottom panel) Landau levels. The two-electron bubble phases ($M = 2$) are colored in yellow, while the three-electron bubble phases ($M = 3$) are colored in blue. Zero R_{yy} near integer filling factors signals integer quantum Hall states, while areas colored in green at half-integer filling factors are quantum Hall nematics. Data is collected at $T = 59$ mK. Reprinted figure from the submitted manuscript Ref. [120].

In Fig 5.1, we present the longitudinal magnetoresistance R_{yy} in the $N = 2$ and $N = 3$ Landau levels against the Landau level filling factor ν. In the $\nu = hn/eB$, h is the Planck constant, e is the elementary charge, and B is the perpendicular magnetic field. Regions where the longitudinal resistance R_{yy} vanishes in this figure associate with diverse phases. Integer quantum Hall states [85] locate at integer filling factors $\nu = i$ ($i = 4, 5, 6,$ and 7), where the $R_{yy} = 0$ and the Hall resistance is quantized to h/ie^2. Quantum Hall nematics or stripe phases [66, 67] reside at half integer fillings $\nu = i + 1/2$. For the last, bubble phases form in the filling factor range between the full and half integers. In the $N = 2$ Landau level, only one type of multi-electron

bubble phase emerges [67, 68]. In contrast, in the $N = 3$ Landau level, two different types of multi-electron bubble phases emerge as recently discovered [99, 117]. The corresponding bubble phases were identified based on an excellent agreement of the measured and predicted filling factors of the RIQHSs and bubble phases. In Fig 5.1, we colored and marked the two-electron ($M = 2$) and three-electron ($M = 3$) bubble phases. The two different multi-electron bubble phases in the $N = 3$ Landau level are distinguished by a local magnetoresistive feature [99, 117] in between. The Hall resistance of bubble phases was quantized to the integer values of the closest integer quantum Hall plateaus [67,68,99,102,117] (not shown in Fig 5.1). Detecting with the techniques other than standard transport, $M = 1$ bubble phases also emerge in these Landau levels as part of the plateaus of the integer quantum Hall states [89–94]. However, since our transport measurements cannot differentiate them from other localized states, the $M = 1$ bubble phases will not be discussed further in this Article.

In Fig 5.1, similarly colored bubble phases appear at the filling factors in particle-hole symmetry relation [73, 99, 117]. We investigate this noticeable symmetry to a greater detail in the following. Bubble phases form in a range of filling factors in high mobility samples such as ours. We define the central filling factor ν_c of a bubble phase as the filling factor of highest bubble stability. Hence, the local minimum of the longitudinal resistance hosting the bubble phase at the highest possible temperature locates at the central filling factor [73, 110].

Table 5.1.
The central filling factors ν_c and onset temperatures T_c of the $M = 2$ and $M = 3$ bubble phases in the $N = 3$ Landau level. Reprinted table from the submitted manuscript Ref. [120].

	R6a	*R6b*	*R6c*	*R6d*	*R7a*	*R7b*	*R7c*	*R7d*
ν_c	6.30	6.22	6.77	6.70	7.30	7.22	7.78	7.70
T_c[mK]	117	100	91	117	101	80	71	100

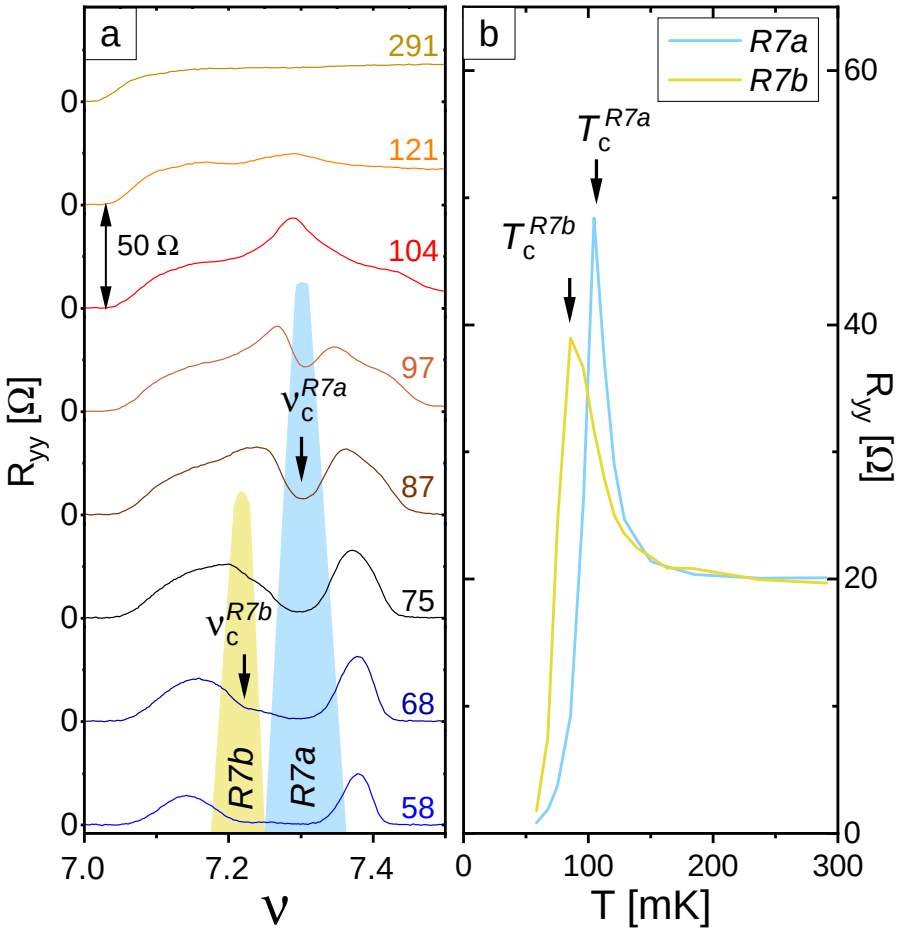

Figure 5.2. (a) Thermal evolution of R_{yy} versus ν (B-field) for the $R7a$ and $R7b$ bubble phases. Temperature in units of mK is marked on each curve. Arrows point the central filling factor ν_c of each bubble phase. (b) Thermal evolution of R_{yy} of the $R7a$ and $R7b$ bubble phases with respect to T at their central filling factors $\nu_c^{R7a} = 7.30$, and $\nu_c^{R7b} = 7.22$. Arrows point the onset temperature T_c of each bubble phase at the peak region. Reprinted figure from the submitted manuscript Ref. [120].

For example, we observe a local minimum in R_{yy} isotherms persists to temperatures as high as $T = 97$ mK for the $R7a$ bubble phase in Fig 5.2a. This local minimum is located at $\nu_c^{R7a} = 7.30$. Similarly, a local resistance minimum develops at $\nu_c^{R7b} = 7.22$ at temperatures as high as $T = 75$ mK for the weaker $R7b$ state. The central filling factors of multi-electron bubble phases in the $N = 3$ Landau level

are presented in Table 5.1. The error for filling factors are ± 0.01. We recognize the central filling factors of the $M = 3$ bubble family are able to be written in the form of $\nu_c = 6 + 0.30, 7 - 0.30, 7 + 0.30, 8 - 0.30$ for $R6a$, $R6d$, $R7a$, and $R7d$ respectively. Also, the filling factors of the $M = 2$ bubble family are able to be written in the form of $\nu_c = 6 + 0.22, 7 - 0.23, 7 + 0.22, 8 - 0.22$ for $R6b$, $R6c$, $R7b$, and $R7c$ respectively. Thus, we found the bubble phases in the $N = 3$ Landau level form at the central filling factors in particle-hole symmetry [99], similarly to those in the $N = 1$ and 2 Landau levels [73, 110].

In Fig 5.2a, the isotherm at $T = 104$ mK exhibits a local maximum, while that at $T = 97$ mK exhibits a local minimum near $\nu_c^{R7a} = 7.30$. We define the onset temperature of $R7a$, T_c^{R7a}, as the average of highest temperature that a local minimum exists in R_{yy} and the next higher measured temperature. The error in determining T_c is extracted from the difference between these two temperatures. The onset temperatures of the multi-electron bubble phases in the $N = 3$ Landau level are found in Table 5.1. The Errors in T_c are ± 5 mK. We remark the local maximum in the $T = 104$ mK isotherm of R_{yy} near $\nu_c^{R7a} = 7.30$ in Fig 5.2a still associate with the bubble phase $R7a$. This local maximum signify the precursor behavior of the $R7a$ bubble phase [111].

In Fig 5.2b, we exhibit the evolution of R_{yy} with respect to T at the central filling factor ν_c for the bubble phases $R7a$ and $R7b$. We name such traces as $R_{yy}(T)|_{\nu=\nu_c}$. These $R_{yy}(T)|_{\nu=\nu_c}$ traces can be thought as profiles at single filling factor $\nu = \nu_c$ in the three dimensional $R_{yy}(\nu, T)$ manifold having two independent parameters ν and T. $R_{yy}(T)|_{\nu=\nu_c}$ is close to vanishing at the lowest measured temperatures as expected, signifying stable development of bubble phases. At $T > 200$ mK, $R_{yy}(T)|_{\nu=\nu_c}$ has a nearly T-independent finite value. However, around $T = T_c^{R7a} = 101$ mK, $R_{yy}(T)|_{\nu=\nu_c}$ for the $R7a$ phase shows a sharp peak. Similar peak behaviors in $R_{yy}(T)|_{\nu=\nu_c}$ traces were captured at the onset temperatures of bubble phases in the $N = 1$ and $N = 2$ Landau levels [73, 110, 113]. As presented in Fig 5.3, we now capture such peaks for all the multi-electron bubble phases in the $N = 3$ Landau level. We conclude the

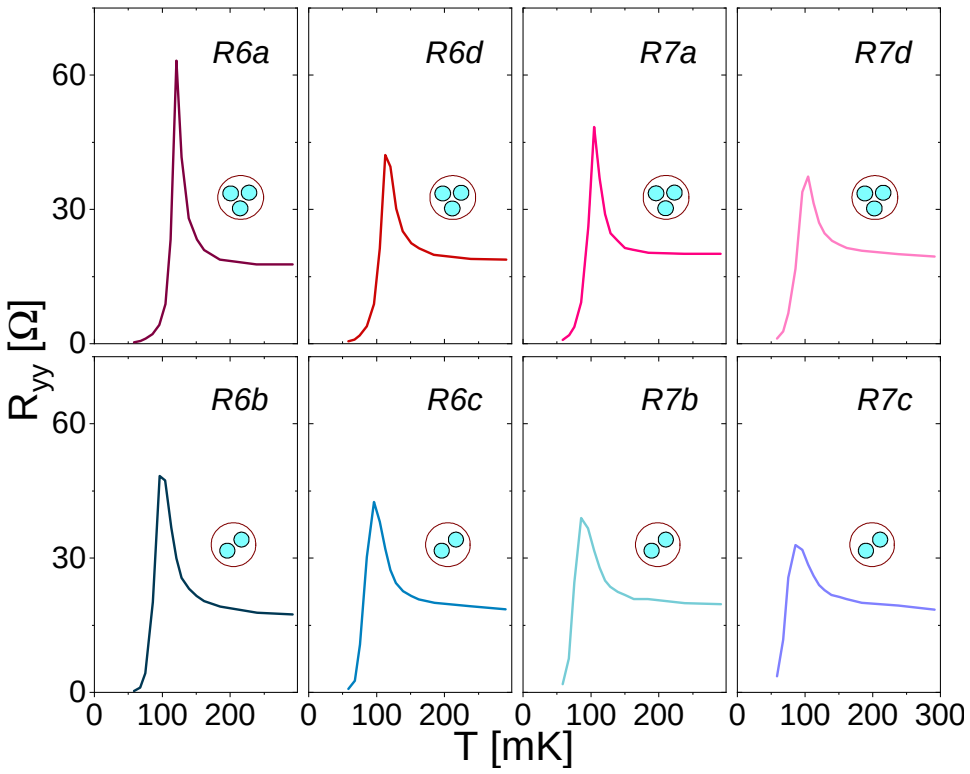

Figure 5.3. Temperature dependence of the longitudinal resistance measured at the central filling factors $\nu = \nu_C$ of the eight bubble phases in the $N = 3$ Landau level. Curves show a sharp peak behavior at the onset temperatures T_c of the bubble phases. Reprinted figure from the submitted manuscript Ref. [120].

peak behaviors present in the $R_{yy}(T)|_{\nu=\nu_c}$ traces at the onset of multi-electron bubble phases irrespective of the Landau level in high mobility samples.

Data of bubble phases in the $N = 3$ Landau level of an alloy sample [99] provides a chance for comparison. The alloy disorder sample in Ref. [99] has a mobility of $\mu = 3.6 \times 10^6$ cm^2/Vs due to the artificially introduced Al into the GaAs channel when the sample was grown. Comparing to mobility of our sample, the value is about a factor of 4 times less. Intriguingly, the multi-electron bubble phases in the $N = 3$ Landau level of the alloy sample emerge at the identical filling factors and in similar temperature ranges compare to those of our bubbles [99]. The increased longitudinal resistance of $\approx$ 80 Ω in the alloy sample [99] which is seen at temperature much

above the onset of bubble is thought to be the consequence of the reduced mobility. In our sample, that is $\approx 18\ \Omega$. Another remarkable consequence is the absence of the peak behavior in the $R_{yy}(T)|_{\nu=\nu_c}$ curves [99]. In the alloy disorder sample [99], the longitudinal magnetoresistance of the bubble phase increases and saturates above 135 mK without the showing a sharp peak, indeed. Currently, the transport in bubble regime is understood as follows: at $T << T_c$, the bubble phase is pinned by the disorder in the sample, while at $T >> T_c$, a uniform uncorrelated liquid forms. In this picture, around $T = T_c$, these two phases compete each other by building an interpenetrating network of domains in the bulk of the sample. The peak behavior of $R_{yy}(T)|_{\nu=\nu_c}$ in a narrow temperature range near $T = T_c$ in our ultra-pure GaAs sample as wells as in graphene [97] indicates the enhanced scattering due to the increased thermal fluctuations between the two competing domains. We conjecture that thermal fluctuations in this kind and the correlated peak behaviors are suppressed in the alloy disorder sample by the presence of deliberately added disorders [99].

5.3 Difference in Stability of M=2 and M=3 Bubble Phases: Comparison of Onset Temperatures and Cohesive Energies

We now scrutinize the two quantities closely related, the onset temperatures of bubble phases and the corresponding cohesive energies calculated in Hartree-Fock theories [73, 110]. We found the $M = 2$ and $M = 3$ bubble phases in the $N = 3$ Landau level have close onset temperatures. This feature is consistent with the Hartee-Fock calculations [61–63,76,77,79–81,114]. However, quantitative comparisons to the calculated cohesive energies are tenuous. This is partially owing to the idealized conditions in the cohesive energies calculations which do not include the disorder and Landau level mixing effects. Difference of more than two orders of magnitude between the calculated cohesive energies [61–63, 76, 77, 79–81, 114] and the measured onset temperatures [73, 110] in the $N = 1$ and $N = 2$ Landau levels were attributed

to these idealized conditions indeed. We found that these discrepancies exist also in the $N = 3$ Landau level [79–81].

Nevertheless, qualitative comparisons of onset temperatures and cohesive energies offer precious insight. It is well-understood that the clustering of electrons into bubbles is fostered during competition of short-range and long-range electron-electron interactions [61–63, 69, 117]. The long-range part is bare Coulomb in nature, whereas the short-range part is softened Coulomb potential. We find that overlap of single electronic wavefunctions [61–63,69,117] and the effect of finite layer thickness [81,119] are in the origin of such a potential softening.

Although the onset temperatures of the $N = 3$ Landau level in Table 5.1 do not seem to follow a special trend at the first sight, a closer investigation reveals two intriguing features. First, onset temperatures of single type bubble families create an approximately linear trend within one Landau level. In Fig 5.4, we present dimensionless reduced onset temperatures $t_c = k_B T_c / E_C$ of multi-electron bubble phases in the $N = 2$ and $N = 3$ Landau levels. Here, k_B is the Boltzmann constant, $E_C = e^2/4\pi\epsilon l_B$ is the Coulomb energy, and l_B is the magnetic length. In Fig 5.4, the three shaded bands with two different colors show these linear trends of the $M = 2$ bubble phases in the $N = 2$ and $N = 3$ Landau levels, and of the $M = 3$ bubble phases of the $N = 3$ Landau level. Because the data from different spin branches of a Landau level lie on the same line, we conclude that onset temperatures are not affected by the spin quantum number. Secondly, the linear trend of t_c with respect to ν_c for the $M = 2$ bubble phases have a similar slope across the different Landau levels: $\partial t_c/\partial \nu_c \approx -2.5 \times 10^{-4}$ in both the $N = 2$ and $N = 3$ Landau levels. Hence, we found bubble phases having the same number of electrons emerging in different Landau levels share a close $\partial t_c/\partial \nu_c$. Contrastingly, the $\partial t_c/\partial \nu_c$ slope of the $M = 3$ bubble phases in the $N = 3$ Landau level is remarkably flattened, decreased by about a factor 5 compared to that of the $M = 2$ bubble phases.

Details on the short-range part of electron-electron interaction, which induces bubble formation, is revealed by identifying the dominating bubble phase in the $N = 3$

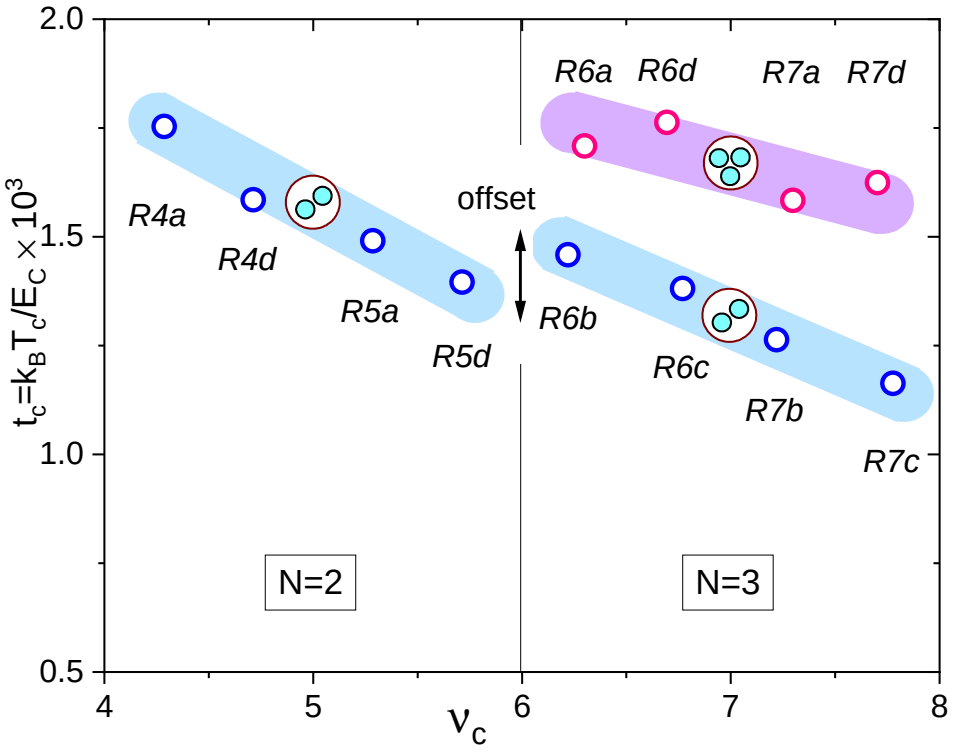

Figure 5.4. The dimensionless reduced onset temperatures $t_c = k_BT_c/E_C$ of the $M = 2$ and $M = 3$ bubble phases in the $N = 2$ and $N = 3$ Landau levels are plotted with respect to the filling factor. color bands guide the trends of onset temperatures of bubble phases having the same number of electrons per bubble. The offset in the dimensionless onset temperatures of the $M = 2$ bubble phases across the $N = 2$ and $N = 3$ Landau level is described by the double arrow. Reprinted figure from the submitted manuscript Ref. [120].

Landau level. We remark that Hartree-Fock calculations do not offer consistent results on the dominant or more stable bubble phase. In the $N = 3$ Landau level, Refs. [76,81] predict the $M = 3$ bubbles to be more stable, while Refs. [79, 80] predict the $M = 2$ bubbles to be dominant. Our findings agree on the former results, while disagree on the latter ones. A persuasive cause of the inconsistency on dominant bubble phase is possibly due to different effective electron-electron interaction. Particularly, the work of Ettouhami et al. [81] comprehensively elaborates this. In the work, the short-range part of the electron-electron interaction is tuned through the layer thickness

parameter λ, while maintaining the long-range part of the potential unchanged [81]. Here, the authors found the energy balance can be significantly changed in the $N = 3$ Landau level. The $M = 3$ bubbles are more stable at $\lambda = 0$, when the short-range softening of electron-electron interaction is not considered, while the $M = 3$ bubbles have nearly the same stability with $M = 2$ bubbles at $\lambda = 1$, when the softening at short distances is considered [81]. Thus, we further conjecture that a stronger softening of the potential may be able to reverse the energy hierarchy of the $M = 2$ and $M = 3$ bubble phases and may yield the experimental inconsistency.

Furthermore, comparing the $M = 2$ bubble energetics in the $N = 2$ and $N = 3$ Landau levels reveals dependence of the electronic short-range interaction on the Landau level index N. The linear trend of dimensionless onset temperatures of $M = 2$ bubble phases with respect to ν_c was discussed earlier. In addition to the similarity of slopes $\partial t_c/\partial \nu_c$, the linear trends show a vertical offset when the Landau level index N changes from 2 to 3 nearby $\nu = 6$. As seen in Fig 5.4, the blue band of $M = 2$ bubble phases in the $N = 3$ Landau level obtained an offset when comparing to that of $M = 2$ bubble phase in the $N = 2$ Landau level. We think this offset is mainly caused by the variation of the short-range effective electron-electron interaction with the Landau level index N. Although the finite layer thickness effects also soften the electron-electron interaction, they are thought to be independent on the Landau level index N. In contrast, the short-range part of the effective Coulomb potential which is an outcome of the overlapping wavefunctions is Landau index dependent [61–63, 69, 117]. This is because the nodal structure in the wavefunctions directly affects on bubble energetics. Thus, the comparison of the $M = 2$ bubble energetics in the $N = 2$ and $N = 3$ Landau levels offers direct evidence that the electronic wavefunction overlap plays a role in shaping the electron-electron interaction in the short-range.

5.4 Conclusion

To conclude, we observed qualitative and quantitative characteristics of bubble phases in the $N = 2$ and $N = 3$ Landau levels. We found the longitudinal resistance versus temperature traces show sharp peaks in the multi-electron bubble regime both in the $N = 2$ and $N = 3$ Landau levels of our high mobility sample. From these peaks, we extract the onset temperatures of the bubble phases. The recent assignment of corresponding bubble phases to the RIQHSs made an analysis of the measured onset temperatures of the bubble phases possible. We first found the dimensionless onset temperatures of $M = 3$ bubbles are higher than those of $M = 2$ bubbles and show a different trend with respect to the filling factor, within the $N = 3$ Landau level. Secondly, we found the dimensionless onset temperatures of $M = 2$ bubble phases across the $N = 2$ and $N = 3$ Landau levels are close each other yet exhibiting an offset. Our results provide information on bubble energetics which is expected to refine the existing theories and provides evidence that short-range electron-electron interactions which are critically influenced by overlap of wavefunction play role in bubble formation.

REFERENCES

[1] E.H. Hall, American Journal of Mathematics **2**, 287-292 (1879).

[2] K. von Klitzing, G. Dorda, and M. Pepper, Phys. Rev. Lett. **45**, 494-497 (1980).

[3] J.K. Jain, *Composite Fermions*, (Cambridge University Press, 2007).

[4] J.H. Davies, *The Physics of Low-Dimensional Semiconductors*, (Cambridge University Press, 1998).

[5] S. Holmes, D.K. Maude, M.L. Williams, J.J. Harris, J.C. Portal, K.W.J. Barnham, and C.T. Foxon, Semicond. Sci. Technol. **9**, 1549-1553 (1994).

[6] D. Vaid, arXiv:1208.3335.

[7] K. He, Physics **8**, 41 (2015).

[8] M. Büttiker, Phys. Rev. B **38**, 9375 (1988).

[9] X. Kou, Y. Fan, and K. Wang, Journal of Physics and Chemistry of Solids **128**, 2-23 (2019).

[10] P. Onorato, M. Malgieri, and A. De Ambrosis, Phys. Lett. A **378**, 590-596 (2014).

[11] C. Chang and M. Li, J. Phys.: Condens. Matter **28**, 123002 (2016).

[12] D.C. Tsui, H.L. Stormer, and A.C. Gossard, Phys. Rev. Lett. **48**, 22 (1982).

[13] J.K. Jain, Phys. Rev. Lett. **63**, 2 (1989).

[14] W. Pan, H.L. Stormer, D.C. Tsui, L.N. Pfeiffer, K.W. Baldwin, and K.W. West, Phys. Rev. Lett. **88**, 176802 (2002).

[15] R.B. Laughlin, Phys. Rev. Lett. **50**, 18 (1983).

[16] R.L. Willet, Rep. Prog. Phys. **76**, 076501 (2013).

[17] G. Murthy and R. Shankar, Rev. Mod. Phys. **75**, 1101 (2003).

[18] B.I. Halperin, Phys. Rev. Lett. **52**, 18 (1984).

[19] F.D.M. Haldane, Phys. Rev. Lett. **51**, 7 (1983).

[20] R. Willett, J.P. Eisenstein, H.L. Stormer, D.C. Tsui, A.C. Gossard, and J.H. English, Phys. Rev. Lett. **59**, 15 (1987).

[21] W. Pan, J.-S. Xia, V. Shvarts, D.E. Adams, H.L. Stormer, D.C. Tsui, L.N. Pfeiffer, K.W. Baldwin, and K.W. West, Phys. Rev. Lett. **83**, 3530 (1999).

[22] G. Moore and N. Read, Nucl. Phys. B **360**, 362-396 (1991).

[23] A.Y. Kitaev, Annals Phys. **303**, 2 (2003).

[24] S. Das Sarma, M. Freedman, C. Nayak. Phys. Rev. Lett. **94**, 166802 (2005).

[25] C. Nayak, S.H. Simon, A. Stern, M. Freedman, S. Das Sarma. Rev. Mod. Phys. **80**, 1083 (2008).

[26] R.H. Morf Phys. Rev. Lett. **80**, 7 (1998).

[27] M. Levin, B.I. Halperin, and B. Rosenow, Phys. Rev. Lett. **99**, 236806 (2007).

[28] S.S. Lee, S. Ryu, C. Nayak, and M.P.A. Fisher, Phys. Rev. Lett. **99**, 236807 (2007).

[29] B.I. Halperin, Helv. Phys. Acta **56**, 75 (1983).

[30] N. Samkharadze, Dohyung Ro, L.N. Pfeiffer, K.W. West, and G.A. Csáthy, Phys. Rev. B. **96**, 085105 (2017).

[31] X. Wan, Z.X. Hu, E.H. Rezayi, and K. Yang, Phys. Rev. B **77**, 165316 (2008).

[32] W. Bishara and C. Nayak, Phys. Rev. B **80**, 121302 (2009).

[33] N. Samkharadze, K.A. Schreiber, G.C. Gardner, M.J. Manfra, E. Fradkin, and G.A. Csáthy, Nat. Phys. **12**, 191 (2016).

[34] K.A. Schreiber, N. Samkharadze, G.C. Gardner, R.R. Biswas, M.J. Manfra, and G.A. Csáthy, Phys. Rev. B **96**, 041107(R) (2017).

[35] K.A. Schreiber, N. Samkharadze, G.C. Gardner, Y. Lyanda-Geller, M.J. Manfra, L.N. Pfeiffer, K.W. West, and G.A. Csáthy, Nat. Commun. **9**, 2400 (2018).

[36] K.A. Schreiber and G.A. Csáthy, Annu. Rev. Condens. Matter Phys. **11**, 17–35 (2020).

[37] G. Gervais, L.W. Engel, H.L. Stormer, D.C. Tsui, K.W. Baldwin, K.W. West, and L.N. Pfeiffer, Phys. Rev. Lett. **93**, 266804 (2004).

[38] K.B. Cooper, J.P. Eisenstein, L.N. Pfeiffer, and K.W. West, Phys. Rev. Lett. **90**, 226803 (2003).

[39] J. Göres, G. Gamez, J.H. Smet, L.N. Pfeiffer, K.W. West, A. Yacoby, V. Umansky, and K. von Klitzing, Phys. Rev. Lett. **99**, 246402 (2007).

[40] B.A. Schmidt, K. Bennaceur, S. Bilodeau, G. Gervais, L.N. Pfeiffer, K.W. West, Solid State Commun. **217**, 1-5 (2015).

[41] K.B. Cooper, J.P. Eisenstein, L.N. Pfeiffer, and K.W. West, Phys. Rev. Lett. **92**, 026806 (2004).

[42] E. Wigner, Phys. Rev. **46**, 1002 (1934).

[43] Y.E. Lozovik and V.I. Yudson, JETP Lett. **22**, 11-12 (1975).

[44] D. Levesque, J.J. Weis, and A.H. MacDonald, Phys. Rev. B **30**, 1056(R) (1984).

[45] P.K. Lam and S.M. Girvin, Phys. Rev. B **30**, 473(R) (1984).

[46] R.L. Willett, H.L. Stormer, D.C. Tsui, L.N. Pfeiffer, K.W. West, and K.W. Baldwin, Phys. Rev. B **38**, 7881(R) (1988).

[47] E.Y. Andrei, G. Deville, D.C. Glattli, F.I.B. Williams, E. Paris, and B. Etienne, Phys. Rev. Lett. **60**, 2765 (1988).

[48] F.I.B. Williams, P.A. Wright, R.G. Clark, E.Y. Andrei, G. Deville, D.C. Glattli, O. Probst, B. Etienne, C. Dorin, C.T. Foxon, and J.J. Harris, Phys. Rev. Lett. **66**, 3285 (1991).

[49] M.A. Paalanen, R.L. Willett, R.R. Ruel, P.B. Littlewood, K.W. West, and L.N. Pfeiffer, Phys. Rev. B **45**, 13784(R) (1992).

[50] Y.P. Li, D.C. Tsui, T. Sajoto, L.W. Engel, M. Santos, and M. Shayegan, Solid State Commun. **95**, 619 (1995).

[51] P.D. Ye, L.W. Engel, D.C. Tsui, R.M. Lewis, L.N. Pfeiffer, and K. West, Phys. Rev. Lett. **89**, 176802 (2002).

[52] Y.P. Chen, G. Sambandamurthy, Z.H. Wang, R.M. Lewis, L.W. Engel, D.C. Tsui, P.D Ye, L.N. Pfeiffer, and K.W. West, Nat. Phys. **2**, 452 (2006).

[53] V.J. Goldman, M. Santos, M. Shayegan, and J.E. Cunningham, Phys. Rev. Lett. **65**, 2189 (1990).

[54] Y.P. Li, T. Sajoto, L.W. Engel, D.C. Tsui, and M. Shayegan, Phys. Rev. Lett. **67**, 1630 (1991).

[55] H.W. Jiang, H.L. Stormer, D.C. Tsui, L.N. Pfeiffer, and K.W. West, Phys. Rev. B **44**, 8107 (1991).

[56] D.G. Schlom, L.N. Pfeiffer, Nature Mater **9**, 881–883 (2010).

[57] M.J. Manfra, Annu. Rev. Condens. Matter Phys. **5**, 347–73 (2014).

[58] F. Pobell, *Matter and Methods at Low Temperature*, (Springer, 2007).

[59] N.H. Balshaw, *Practical Cryogenics*, (Oxford Instruments Superconductivity Limited, 2001).

[60] K.A. Schreiber, *Ground States of the Two-Dimensional Electron System at Half-Filling under Hydrostatic Pressure*, PhD thesis, Purdue University, (2018).

[61] A.A. Koulakov, M.M. Fogler, and B.I. Shklovskii, Phys. Rev. Lett. **76**, 499 (1996).

[62] M.M. Fogler, A.A. Koulakov, B.I. Shklovskii, Phys. Rev. B **54**, 1853 (1996).

[63] R. Moessner, and J.T. Chalker, Phys. Rev. B **54**, 5006 (1996).

[64] F.D.M. Haldane, E.H. Rezayi, and K. Yang, Phys. Rev. Lett. **85**, 5396 (2000).

[65] N. Shibata and D. Yoshioka, Phys. Rev. Lett. **86**, 5755 (2001).

[66] M.P. Lilly, K.B. Cooper, J.P. Eisenstein, L.N. Pfeiffer, and K.W. West, Phys. Rev. Lett. **82**, 394 (1999).

[67] R.R. Du, D.C. Tsui, H.L. Stormer, L.N. Pfeiffer, K.W. Baldwin, and K.W. West, Solid State Commun. **109**, 389 (1999).

[68] K.B. Cooper, M.P. Lilly, J.P. Eisenstein, L.N. Pfeiffer, and K.W. West, Phys. Rev. B **60**, R11285 (1999).

[69] J.P. Eisenstein, Solid State Commun. **117**, 123 (2001).

[70] X. Wang, H. Fu, L. Du, X. Liu, P. Wang, L.N. Pfeiffer, K.W. West, R.R. Du, and X. Lin, Phys. Rev. B **91**, 115301 (2015).

[71] R.M. Lewis, P.D. Ye, L.W. Engel, D.C. Tsui, L.N. Pfeiffer, and K.W. West, Phys. Rev. Lett. **89**, 136804 (2002).

[72] R.M. Lewis, Yong Chen, L.W. Engel, D.C. Tsui, P.D. Ye, L.N. Pfeiffer, and K.W. West, Phys. Rev. Lett. **93**, 176808 (2004).

[73] N. Deng, J.D. Watson, L.P. Rokhinson, M.J. Manfra, and G.A. Csáthy, Phys. Rev. B **86**, 201301(R) (2012).

[74] M.E. Msall and W. Dietsche, New J. Phys. **17**, 043042 (2015).

[75] B. Friess, Y. Peng, B. Rosenow, F. von Oppen, V. Umansky, K. von Klitzing, and J.H. Smet, Nat. Phys. **13**, 1124 (2017).

[76] M.M. Fogler and A.A. Koulakov, Phys. Rev. B **55**, 9326 (1997).

[77] M.M. Fogler, "Stripe and bubble phases in quantum Hall systems", in *High magnetic fields: applications in condensed matter physics and spectroscopy*, (Springer-Verlag, Berlin, 2001).

[78] D. Yoshioka and N. Shibata, Physica E **12**, 43 (2002).

[79] R. Côté, C.B. Doiron, J. Bourassa, and H.A. Fertig, Phys. Rev. B **68**, 155327 (2003).

[80] M.O. Goerbig, P. Lederer, and C.M. Smith, Phys. Rev. B **69**, 115327 (2004).

[81] A.M. Ettouhami, F.D. Klironomos, and A.T. Dorsey, Phys. Rev. B **73**, 165324 (2006).

[82] K. Bennaceur, C. Lupien, B. Reulet, G. Gervais, L.N. Pfeiffer, and K.W. West, Phys. Rev. Lett. **120**, 136801 (2018).

[83] B. Friess, V. Umansky, K. von Klitzing, and J.H. Smet, Phys. Rev. Lett. **120**, 137603 (2018).

[84] Q. Shi, M.A. Zudov, J.D. Watson, G.C. Gardner, and M.J. Manfra, Phys. Rev. B **93**, 121404(R) (2016).

[85] K. von Klitzing, G. Dorda, and M. Pepper, Phys. Rev. Lett. **45**, 494 (1980).

[86] S.A. Kivelson, E. Fradkin, and V.J. Emery, Nature **393**, 550 (1998).

[87] E. Fradkin and S.A. Kivelson, Phys. Rev. B **59**, 8065 (1999).

[88] L. Radzihovsky and A.T. Dorsey, Phys. Rev. Lett. **88**, 216802 (2002).

[89] Y.P. Chen, R.M. Lewis, L.W. Engel, D.C. Tsui, P.D. Ye, L.N. Pfeiffer, and K.W. West, Phys. Rev. Lett. **91**, 016801 (2003).

[90] R.M. Lewis, Y.P. Chen, L.W. Engel, D.C. Tsui, P.D. Ye, L.N. Pfeiffer, and K.W. West, Physica E **22** 104 (2004).

[91] D. Zhang, X. Huang, W. Dietsche, K. von Klitzing, and J.H. Smet, Phys. Rev. Lett. **113**, 076804 (2014).

[92] L. Tiemann, T.D. Rhone, N. Shibata, and K. Muraki, Nat. Phys. **10**, 648 (2014).

[93] T.D. Rhone, L. Tiemann, and K. Muraki, Phys. Rev. B **92**, 041301(R) (2015).

[94] J. Jang, B.M. Hunt, L.N. Pfeiffer, K.W. West, and R.C. Ashoori, Nat. Phys. **13**, 340 (2017).

[95] Z.F. Ezawa, *Quantum Hall effects: field theoretical approach and related topics.*, (World Scientific, 2008).

[96] P. Ball, *The self-made tapestry: pattern formation in nature*, (Oxford University Press, 1999).

[97] S. Chen, R. Ribeiro-Palau, K. Yang, K. Watanabe, T. Taniguchi, J. Hone, M.O. Goerbig, and C.R. Dean, Phys. Rev. Lett. **122**, 026802 (2019).

[98] Dohyung Ro, N. Deng, M.J. Manfra, L.N Pfeiffer, K.W West, and G.A Csáthy, Bull. Amer. Phys. Soc. R01.00003 (2019).

[99] X. Fu, Q. Shi, M.A. Zudov, G.C. Gardner, J.D. Watson, and M.J. Manfra, Phys. Rev. B **99**, 161402(R) (2019).

[100] D.C. Tsui, H.L. Stormer, and A.C. Gossard, Phys. Rev. Lett. **48**, 1559 (1982).

[101] M. Shayegan, "Case for the Magnetic-Field-Induced Two-Dimensional Wigner Crystal", in *Perspectives in Quantum Hall Effects*, ed. S. Das Sarma and A. Pinczuk, Wiley (2004).

[102] J.P. Eisenstein, K.B. Cooper, L.N. Pfeiffer, and K.W. West, Phys. Rev. Lett. **88**, 076801 (2002).

[103] E. Fradkin, S.A. Kivelson, M.J. Lawler, J.P. Eisenstein, and A.P. Mackenzie, Annu. Rev. Condens. Matter Phys. **1**, 153 (2010).

[104] R.M. Lewis, Y.P. Chen, L.W. Engel, D.C. Tsui, L.N. Pfeiffer, and K.W. West, Phys. Rev. B **71**, 081301(R) (2005).

[105] S. Baer, C. Rössler, S. Hennel, H.C. Overweg, T. Ihn, K. Ensslin, C. Reichl, and W. Wegscheider, Phys. Rev. B **91**, 195414 (2015).

[106] A.V. Rossokhaty, Y. Baum, J.A. Folk, J.D. Watson, G.C. Gardner, and M.J. Manfra, Phys. Rev. Lett. **117**, 166805 (2016).

[107] J.S. Xia, W. Pan, C.L. Vicente, E.D. Adams, N.S. Sullivan, H.L. Stormer, D.C. Tsui, L.N. Pfeiffer, K.W. Baldwin, and K.W. West, Phys. Rev. Lett. **93**, 176809 (2004).

[108] W. Pan, J.S. Xia, H.L. Stormer, D.C. Tsui, C. Vicente, E.D. Adams, N.S. Sullivan, L.N. Pfeiffer, K.W. Baldwin, and K.W. West, Phys. Rev. B **77**, 075307 (2008).

[109] J. Nuebler, V. Umansky, R. Morf, M. Heiblum, K. von Klitzing, and J. Smet, Phys. Rev. B **81**, 035316 (2010).

[110] N. Deng, A. Kumar, M.J. Manfra, L.N. Pfeiffer, K.W. West, and G.A. Csáthy, Phys. Rev. Lett. **108**, 086803 (2012).

[111] V. Shingla, E. Kleinbaum, A. Kumar, L.N. Pfeiffer, K.W. West, and G.A. Csáthy, Phys.Rev. B **97**, 241105(R) (2018).

[112] W.E. Chickering, J.P. Eisenstein, L.N. Pfeiffer, and K.W. West, Phys. Rev. B **87**, 075302 (2013).

[113] W.E. Chickering, *Thermopower in Two-Dimensional Electron Systems*, PhD thesis, California Institute of Technology, (2016).

[114] M.O. Goerbig, P. Lederer, and C.M. Smith, Phys. Rev. B **68**, 241302(R) (2003).

[115] N. Shibata and D. Yoshioka, J. Phys. Soc. Jpn. **72**, 664 (2003).

[116] N. Shibata and D. Yoshioka, Physica E **22**, 111 (2004).

[117] Dohyung Ro, N. Deng, J.D. Watson, M.J. Manfra, L.N. Pfeiffer, K.W. West, and G.A. Csáthy, Phys. Rev. B **99**, 201111(R) (2019).

[118] N. Samkharadze, A. Kumar, M.J. Manfra, L.N. Pfeiffer, K.W. West, and G.A. Csáthy, Rev. Sci. Instrum. **122**, 026802 (2019).

[119] F.C. Zhang and S. Das Sarma, Phys. Rev. B **33**, 2903(R) (1986).

[120] Dohyung Ro, S.A. Myers, N. Deng, J.D. Watson, M.J. Manfra, L.N. Pfeiffer, K.W. West, and G.A. Csáthy, *manuscript submitted*.